NUCLEAR MAGNETIC RESONANCE IMAGING OF TUMOR PATHOPHYSIOLOGY AND ANGIOGENESIS

BY

SCOTT DEWITT PACKARD

B.A. Physics
Cornell University, 1996

SUBMITTED TO THE HARVARD-MIT DIVISION OF HEALTH SCIENCES AND TECHNOLOGY AND DEPARTMENT OF NUCLEAR ENGINEERING IN PARTIAL FULFILLMENT OF THE REQUIREMENTS FOR THE DEGREE OF

DOCTOR OF PHILOSOPHY
IN RADIOLOGICAL SCIENCES
AT THE
MASSACHUSETTS INSTITUTE OF TECHNOLOGY

JUNE 2002

Signature of Author:

Division of Health Sciences and Technology
Department of Nuclear Engineering
April 24, 2002

Certified by:

Bruce R. Rosen
Professor of Health Sciences and Technology, Radiology
Massachusetts Institute of Technology, Harvard Medical School
Thesis Supervisor

Certified by:

John J. A. Marota
Associate Professor of Anesthesia, Harvard Medical School
Thesis Reader

Accepted by:

Martha L. Gray
Chairman, J. W. Kieckhefer Professor of Electrical and Medical Engineering

ACKNOWLEDGEMENTS

There are numerous people who contributed to this work, both directly with scientific support and indirectly by empowering me to achieve. Among the former are colleagues at MGH, MIT, Harvard Medical School, and Merck & Co. Of special note are those who contributed in essential ways. John Moore helped make the final studies work. Jacqueline Yanch poignantly asked me what my thesis was about early in the process, helping my committee and I work toward a reasonable goal. Nino Chiocca provided support not only during thesis committee meetings but also through his laboratory and its generous members. Tim Davis helped me numerous times to overcome obstacles and engaged in enthusiastic conversations with me regarding cancer imaging. Joe Mandeville invested his valuable time in training me and provided crucial thesis and paper comments. Laura Sepp-Lorenzino started as a collaborator who provided me the opportunity to study a novel anti-cancer drug and became a supportive friend. Bruce Rosen gave me the opportunity to learn about the field at numerous meetings and workshops over the years. It was by watching him that I learned to construct convincing stories from numbers, a skill that will no doubt serve me in all my future endeavors. Finally, John Marota, anesthesiologist and cancer physiology enthusiast, taught me how to do science. From him I learned the power of meticulous planning, the precision required to execute good experiments, and that biology waits for no one. He patiently explained the power and necessity of hypotheses, and how to chase the answers to them. I am also indebted to him for his gracious lessons in scientific writing. Finally, and most importantly, I appreciate that he looked out for me.

Trailblazing is not easy, and I graciously thank those that have empowered me to do so and those that help me find my way. My mother successfully convinced me that I could achieve anything I wanted. Her faith and eventually my own has fueled me through difficult times personally and professionally. Without her, there is not a chance that I could come this far. From this foundation, the wisdom of experience taught me the courage to say no to others and to fundamentally respect myself. For this and everything else, I will always love and respect her.

There are friends that one has forever. Dave has always had the power to make me laugh, under any circumstances. James and I have been partners-in-crime for over 15 years. Sometimes moral compass, sometimes hooligan -- always a man to count on. Rocco, friend and guide, provides a model of how to get where you want to be, and how to enjoy the journey. I cannot remember a time before we were friends.

Now I get to live happily ever after with the woman of my dreams. Angela, you helped me persevere when even I began to doubt. You brought meaning into my life. I love you. I deeply apologize for not being as present as you deserved, and I promise to always put us first.

Cambridge, MA
April 2002

Table of Contents

TABLE OF TABLES AND FIGURES

Chapter 1 Introduction

The goal of this research was to refine, validate, and apply MR metrics to further our knowledge of the tumor vasculature as compared to the normal matrix of blood vessels. The timely convergence of research disciplines, innovation, and motivation has both enabled and driven the scientific progress contained herein. We exploited a unique opportunity to build upon the physics of magnetic susceptibility contrast and apply a novel intravascular contrast agent to address questions at the intersection of radiology and tumor biology with ramifications ranging from pre-clinical drug development to human cancer treatment evaluation. This work ties these disparate fields together by synthesizing the results of experimental MR techniques and careful histological analysis and subsequently proving useful correlations between the two. The result is not only the characterization of these new MR tools, but also the elucidation of differences between normal and tumor-spawned blood vessels. From background to conclusion, each chapter motivates or describes the unique contributions of this thesis.

Chapter 2 presents an overview of the penetrance of cancer and consequently, the significance of methods to identify and track tumor growth. We explore the significance of cancer in modern society in the context of its historical impact. Some basic concepts of physiology are explored in Chapter 3, primarily in vascular physiology and cancer biology. These two research areas are linked by a discussion of tumor angiogenesis, the process by which tumors incite the growth of their own vasculature, as understanding of this topic provides the backdrop in which to discuss our MRI and histological findings.

Some essential foundations of nuclear magnetic resonance are presented in Chapter 4 along with commentary on relevant literature. The reader may consult this section for detailed information and appropriate citations related to the basics of NMR and specific information on magnetic susceptibility contrast methods and theory.

Chapter 5, the first data chapter, presents the results of a somewhat complicated set of experiments involving the application of both steady state and dynamic contrast enhanced MR imaging methods to interrogate the vasculature of human gliomas in rat models. Utilizing these techniques and a novel contrast agent we study tumor vessels with respect to normal vessels along two lines: morphometry and physiology. We study tumor vessel morphometry by evaluating total and microvascular cerebral blood volume (CBV) as well as mean vessel size (MVS). Our physiological measurement is the determination of the flow/volume relationship within tumors quantified by our definition of a metric of perfusion efficiency. We find numerous differences between tumor-based vessels and their normal counterparts and relate MR-based metrics of blood volume and mean vessel size with the gold-standard of histology.

We discuss the second component of our interrogation of tumor vascularity in Chapter 6. Having explored the relationships of blood flow, blood volume and vessel size, we turn our attention to the functional status of tumor vessels. With a better understanding of the baseline characteristics of tumor vessels with respect to their normal counterparts, we test vasoreactivity in response to physiological challenges. For the first time, both vasodilation and vasoconstriction are measured, providing a more complete picture of functional status, and proving that non-response to vasodilating stimuli does not necessarily indicate absence of function.

The third experimental component of our exploration of tumor vascularity, described in Chapter 7, takes a different approach, measuring the extraction of a common contrast agent into the extravascular extracellular space. For many years, scientists and clinicians have exploited the paramagnetic properties of Gadolinium DTPA to identify regions of extensive blood-brain barrier (BBB) breakdown and other hyperpermeability. Extending this common clinical approach beyond localization of BBB breakdown, we employed a quantitative technique of measuring vasculature permeability surface area product (PS) to discern the effect of an experimental permeability-altering cancer therapeutic. In doing so, we demonstrate an imaging-based biomarker based on clinically-available materials.

The final chapter summarizes the major results and conclusions from all the experiments to provide a broad and coherent picture of the findings in this thesis. We validate novel MR imaging approaches to vascular interrogation and with them, demonstrate significant differences between normal vessels and those derived from rampant tumor angiogenesis.

Chapter 2 Cancer and Society

Magnitude of Cancer

Overall

Cancer is a massive public health problem. The second leading killer in the United States, cancer has major societal impact and remains, despite great medical advances, a feared and frequently lethal disease. Cancer is a family of diseases based on the development of genetic flaws or flaws in the expression of genes. While enormous progress has been made in the understanding of cancer, cancer in many ways has a more significant impact on our lives today than it had on previous generations. How is this possible?

Cancer is a disease of modern society for several reasons. People now live much longer than in previous generations. In medieval times, life expectancy was less than 30 years, less still if deaths at birth are factored in. Our extended lifespan is primarily due to medicine and nutrition. We live in an era blessed with cures to diseases formerly fatal and with powerful curative or life-extending drugs and surgical techniques for many diseases. As life is extended, more time is available for the summation of genetic errors and the emergence of malignant disease states.

Advanced clinical diagnosis is paradoxically a cause of increased incidence of cancer. As people live longer and we become more adept at identifying cancer *before* the presentation of clinical signs (often a point of no return), physicians now diagnose more cancer than in previous times. By allowing more time for the natural accidents of cancer to occur and by peering more closely into the human body, we have exposed a more true representation of the penetrance of cancer. In fact, careful autopsy of senior citizens considered cancer-free almost always yields evidence of cancer – microscopically, if not grossly. From this fact, we are left to deduce that given enough time each of us has the capacity to develop a cancerous growth either through fated cellular programming or the inability to prevent perpetuation of genetic or transcriptional errors.

Consequently, there is great need for the technologies to identify and treat cancer as early as possible. Often it is the stage of diagnosis that determines a patient's prognosis. MRI is one useful technique for the identification and tracking of malignancy. Standard anatomical MRI and Gadolinium based enhancement studies are common. Recent work in the field has proved more specific correlations between MR metrics and clinical parameters such as tumor grade. But there is still much progress to be made in developing advanced and specific techniques MRI for use in the clinics or in research settings. In this thesis, we explore ways in which MRI techniques can inform us about tumors, particularly their vasculature. In doing so, we hope to begin a bridge between rather esoteric MRI physics and a vital clinical applications.

History

It is useful to place recent advances in cancer identification and treatment into the historical context. In doing so, we outline a progression from belief-based to fact-based medicine. Specifically, treatment options progress as technology progresses. The evaluation of cancer treatment advanced from visual inspection to microscopic inspection, and now to minimally invasive imaging. Ironically, the ultimate measure of clinical value has not changed in thousands of years: patient survival time.

Ancient Times

Cancer has been recognized as a disease state since the time of the ancient Egyptians. Their priest/physicians were the first to distinguish between different types of lumps on the body. Evidence suggests that there have always been cancer-type growths, beginning from the evolution of complex multi-cellular organisms. Signs of malignancy have been found in fossil remains, skeletal remains of prehistoric people, and in the soft tissues of Egyptian mummies.

The recognition of the existence of malignancy demonstrated by the Egyptians and others took thousands of years to evolve. The next levels of understanding were attained in Mediterranean Europe. Widely considered the father of modern medicine, Hippocrates delineated several types of cancer and coined the Greek term karkinos (meaning crab) to describe these lesions based on their appearance and tenacity. In the Greek era, growths were divided into "phymata" (growths), "oidemata" (soft swellings), and "karkinos" (hard swellings) (Hanahan 1997). Hippocrates was familiar with the problem of anal and rectal carcinoma and pioneered digital proctology techniques to examine such tumors.

Hippocrates, and later Galen, espoused a theory in which all tumors were derived from a substance called black bile. This mysterious substance, along with blood, phlegm and yellow bile, constituted the four body humors. Each humor was equated with an element: black bile with earth, blood with fire, phlegm with air, and yellow bile with water. They believed that food was digested in the stomach and intestines and the by-products went to the liver and spleen where yellow and black bile respectively were produced. The blood that flowed in arteries and veins was actually a composite of all these humors. This early concept of humoral balance as the basis of health resonates with recent, albeit much more complicated, theories regarding the balance required to maintain normal angiogenesis. Even current concepts of balance between the growth and death of cells find analogues in the medicine of early civilization.

Clarrisimus Galen, the famous Roman physician, wrote *De Tumoribus Praeter Naturam* (On Abnormal Swellings) in 192 AD. His descriptions of swellings and tumors were based on clinical observations, but his views on the etiology of tumors came strictly from the humoral theories of the Greeks, most notably his predecessor Hippocrates. In his work he also described the following lesions, a rather complete summary of clinical signs of growth and inflammation:

phlegmone – swellings associated with distension, throbbing pain, heat, and redness -- most likely an inflammatory lesion
polysarkia – non-inflammatory cyst filled with clear fluid, not blood
kolpos – an ulcerated inflammatory lesion which secreted pus
pangrainai – gangrene
karkinoi – all hard, cancerous lesions which started out as painless lumps but which eventually ulcerated through the skin before causing death
phagedaina – malignant tumor which had ulcerated through the skin
ecchymonia – extensive bruises particularly those affecting the elderly
aneurysma – swelling caused by blockage in a blood vessel or the weakening of an artery
elephas – leprosy
myrmekia – warts
psydrakes – pimples

epikynktides – swellings from insect bites
dothien – small boils
phygethlon – glandular swellings
kirsoi – varicose veins

Table 1 – Galen's catalogue of neoplasia and inflammation.

Galen was very thorough in his attempt to understand via classification, as was the hallmark of biology from his era onward until functional understanding became possible and experimentation became the scientific method of choice.

Middle Ages and Beyond

The Middle Ages are known as a time when knowledge seemingly vanished from society save for a few extraordinary libraries. Fortunately the advances made primarily in Greece and Rome were stored and built upon in the Arab world during these dark times in Europe. The greatest medical figure of this era was Ibn Sina (aka. Avicenna) 980-1037. He wrote an encyclopedia that summarized all existing medical knowledge of the time, *The Canon.* As numerous cancers of the internal organs had been identified by this time, it was becoming understood that cancer could strike virtually any tissue.

In 1700 the French physician Claude Deshais Gendron made a leap forward from prevailing thought of the time. While most still believed in the humoral theory of cancer, Gendron published his work *Recherches sur la Nature et la Guerison des Cancers* in which he proposed that cancers were not due to humoral imbalance or corrosive effects of blood or lymph. He suggested that cancers were degenerative growths and their masses represented 'transformation of nervous, glandular, and lymphatic-vascular parts into a uniform, hard, compact, insoluble substance capable of growth and ulceration.' Gendron had struck upon a key concept in cancer that was truly understood only in the 20th century: cancer arises from transformations of normal cells.

Eventually, tissue-based rather than humoral-based theories of cancer evolved and took precedence. Bichat and Laënnec, distrusting the new development of microscopy, relied on the naked eye, knives, and a few simple stains to explore the tissue level structure of the human body. Despite their primitive methods, they categorized 21 tissue systems of the body that closely represent modern understanding of histology. The next major advance in understanding the cellular nature of cancer came from Schwann and Schleiden in the early and mid 1800's who invoked the two key elements of modern histology: microscopy and special stains. They described plants as aggregates of nucleus-containing cells that seemed mostly autonomous. They introduced the concept of cells as the building blocks of cells and tissues. Schwann also traced adult cells back to embryonic primary tissue. Mueller in 1838 explored the idea of the cancer cell, and described tumors in these terms. He explored the duel hypotheses that cancer cells were neo-formations versus transformations of cells that were already there. Later, it would become clear that both were correct.

Increased understanding of the cellular nature of cancer has relied upon methods of observing such cells. The Dutch scientist Zaccharias Janssen developed the first microscope in 1590, followed by Galileo's version in 1610. Advances in this light-based imaging technology revolutionized their understanding of cancer at the cellular level. Concomitant with this understanding were advances in treatment. We now enter a time in which molecular and functional imaging will help guide and evaluate treatments derived from molecular biology.

Treatment Philosophies

Surgery

Still a commonly employed technique, surgical resection of tumor is the oldest continuously practiced cancer treatment. Our knowledge of surgery dates back to The Edwin Smith Papyrus, the oldest known surgical treatise. It was written in Egypt in 1600 BC and is based on documents from 3000 BC and details that little hope existed for ancient Egyptian cancer victims, noting that no surgery at all was better for the patient than surgery on a lesion that was ulcerated.

On November 25, 1884, Dr. Rickman J. Godlee performed the first recognized resection of a primary brain tumor, at the Hospital for Epilepsy and Paralysis in London. He found an encapsulated glioma and removed it, although the patient died nearly a month later of meningitis and secondary complications. At this time there was no clinical precedent for opening an intact skull and manipulating the brain (Kirkpatrick 1984).

Harvey Cushing is considered by many to be the father of modern brain surgery. As professor of surgery at Harvard between 1912 and 1932, he performed over two thousand brain tumor surgeries and authored The Pituitary Body and its Disorders (1912) and Intracranial Tumors (1932). He pioneered the transpheroidal approach for removal of pituitary tumors, sparing other cranial structures. In 1936, Dr. K. G. MacKenzie of Toronto performed the first surgical approach to glioblastomas, previously considered inoperable, terminal lesions. While much as changed in the operating room, the tumor removal process is fundamentally the same as 5000 years ago.

Radiotherapy

Cancer radiotherapy developed from the discovery in the 1890s of xrays by Roentgen and from the discovery of radium by the Curies. They discovered that these agents have the capacity to produce skin damage. Eventually, the theoretical fabric of modern radiotherapy was built on the clinically critical concepts of dose, dose fractionation, dose timing, oxygenation, radiosensitizers and cell kinetics. The birth of clinical radiotherapy occurred in 1922 when Coutard and Houtant demonstrated the efficacy of radiotherapy for advanced laryngeal cancer.

Chemotherapy and Beyond

While chemotherapy has been used clinically through much of the 20th century, drug treatment of cancer has been primarily a disappointment. Cytotoxic therapy often damages the patient's healthy cells as much as the cancerous ones, and survival time based solely on chemotherapy is poor, such that it is almost always used in conjunction with surgery or radiotherapy, or both. But a new class of drugs holds promise to approach cancer treatment in a novel and potentially powerful way, restricting tumor growth through targeting of prerequisite blood vessels. While a complete discussion of recent trends in anti-angiogenic therapeutic targets is beyond the scope of this work, I will address here some of the major angiogenic factors, and their effects as currently understood, on endothelial cells.

Growth Factors and Receptor Tyrosine Kinases

The best-characterized regulators of angiogenesis are growth factors and receptor tyrosine kinases (RTKs) which modulate migration and proliferation of endothelial cells. Most of these RTKs contain an extracellular ligand binding domain, a transmembrane domain and an intracellular catalytic domain that transfers phosphate from ATP to substrate proteins initiating a signaling cascade. The receptors of most interest for angiogenesis are FLT-1 and Flk-1/KDR, the receptors for vascular endothelial growth factor (VEGF). Additionally, Tie1 and Tie2/Tek, the receptors for angiopoetins may also prove relevant targets for anti-angiogenesis. These receptors all modulate angiogenesis on endothelial cells.

Vascular Endothelial Growth Factor

VEGF is a dimeric protein that acts on endothelial cells inducing both permeability and proliferation. Its action is modulated through tyrosine kinase receptors. VEGF is upregulated during the angiogenic processes, both physiological (such as wound healing, menstruation, and fetal development) and pathological (tumor angiogenesis and diabetic retinopathy). The relationship between VEGF and tumor angiogenesis has been well studied in rodent models (Hanahan 1997). Countless studies relate VEGF with various forms of human cancer including human glioblastomas used in this work. This association is at least partially paracrine, with tumors secreting factors to drive their own ability to expand. A link has also been discovered between KDR-mediated angiogenesis and hypervascularity associated with Kaposi's Sarcoma (KS) in the context of advanced human immunodeficiency virus (HIV). Ganju *et al.* discovered that Tat, a protein associated with HIV, can functionally bind KDR, one of the most potent VEGF RTKs (Ganju, Munshi et al. 1998).

Platelet Derived Growth Factor

Platelet-derived growth factor is a homo-or heterodimer of two polypeptides, termed the A and B chains, which intereact with two receptor subtypes, PDGFRα and PDGFRβ. Its receptors are expressed in microvascular endothelium during endothelial cell activation and angiogenesis. PDGF has been found to induce tube formation (Battegay, Rupp et al. 1994) and upregulate VEGF (Enholm, Paavonen et al. 1997) among other findings. Additional findings that PDGF and its receptors are expressed not only in endothelial cells but also tumor cells, stroma, and pericytes suggest PDGF's action may be both direct, through endothelial cell migration, and indirect, by upregulating VEGF.

Angiopoietin and Ties

Tie1 and Tie2 are expressed in the vascular endothelium during embryonic development. Tie2 knockout and transgenic models suggest that Tie2 is important for vasculogenesis, while Tie1 seems to play an important role in maintaining vascular integrity (Hanahan 1997). Tie2 and its ligand, Angiopoetin-1, appear to be required for pericyte and smooth muscle cells recruitment. Angiopoetin-2 competitively inhibits the effect of angiopoetin-1(Tie-2 phosphorylation). While the fine details of their actions are still being worked out, Tie1 and Tie2 are also likely to be important targets for angiogenesis-based therapeutic intervention given their endothelial-specific expression.

Matrix Metalloproteinases

Matrix metalloproteinases (MMPs) are members of a multi-gene family of zinc-dependent enzymes. Their function in angiogenesis is to degrade the extracellular matrix, permitting the generation and extention of pre-vascular stromal scaffolding. Its expression can be increased by several factors including interleukin-1, VEGF, EGF, PDGF, and TNF-α (see review by Benaud (Benaud, Dickson et al. 1998)). There are well over a dozen versions of the MMP enzyme, each acts on a different substrate, ranging from tooth enamel (MMP-19) to the multiversatile elastase (MMP-12). A number of MMP inhibtors are already in clinical trial.

Integrins

Invasion, migration, and proliferation of vascular endothelial and smooth muscles cells during angiogenesis are regulated by integrins, a family of cell adhesion proteins. This group comprises 15α and 8β subunits that are expressed in various heteodimeric combinations on cell surfaces permitting a variety of downstream effects. Integrins bind to the extracellular matrix. The integrins that are expressed on smooth muscle and endothelial cells (e.g. $\alpha_v\beta_3$) are commonly used as vascular markers in histopathology. Because $\alpha_v\beta_3$ is expressed during angiogenesis but not on normal vessels, it is a promising molecular target.

Unorthodox Treatments

One advantage of enhanced diagnostic imaging techniques is the ability to evaluate the efficacy of novel treatments before widespread use in the clinical community. Early medicine was plagued by the application of numerous fraudulent approaches to treatment as well as outright foolishness – either way, these approaches did not work. The following extreme examples make the point that patients and doctors need to know the value of experimental compounds *before* clinical application. Imaging based techniques such as those presenting in this work are a step in this direction.

L. D. Rogers founded the National Medical University of Chicago as well as the American Cancer Research Society at the turn of the century. Rogers treated patients with injections of their own blood after he had "incubated and energized" it. He then claimed that the injected blood had special immunological properties capable of attacking tumor tissue.

Arthur d' Collard of Richmond, Virginia practiced what he called "poropathy," s,imilar to chiropractic medicine in which internal tumors were "cured" through spinal manipulations.

Albert Abrams of San Francisco was at one time a respected physician and pathologist. But in 1910 he developed what he called "spondylotherapy" for cancer. It resembled a chiropractic treatment. Later he developed his electronic "dynamizer" to help physicians diagnose and cure cancer. It had absolutely no therapeutic value, but Abrams managed to sell the devices to unorthodox medical practitioners throughout the world.

In the 1920's Lester Tilton of Chicago introduced his "blood poison treatment" for cancer, an escharotic containing zinc. Tilton was convicted of violating the Medical Practice Act of Illinois and imprisoned.

William Koch, a graduate of the University of Michigan, announced in 1919 that he had discovered a cure for cancer through "recrystallized synthetic antitoxin." Throughout the 1920's and 1930's the Koch treatment was extremely popular among cancer patients and their families, even though it had no therapeutic value. Eventually, Koch left his business in Detroit and set up practice in Sao Paulo, Brazil.

In the 1930's Norman Maker, a radio broadcaster from Muscatane, Iowa, set up the Baker hospital to treat cancer patients with two drugs: an arsenic powder and a concoction of various herbs and grasses. Baker eventually set up numerous treatment centers before being arrested and convicted of fraud.

Thomas Glover, a physician in Toronto announced a new treatment for cancer in 1920. The Glover serum was created by taking blood and tumor tissue from cancer victims, injecting them into a horse, waiting a week, taking blood specimens from the horse, and then injecting this "anti-serum" into the same cancer patients. Glover later worked for the Hygienic Laboratory, which eventually became the National Institutes of Health, testing his serum but co-workers could never substantiate his claims.

Max Gerson, a physician who died in 1959, established a sanitarium in New York city which claimed to cure cancer through nutritional therapy – a diet consisting of liver, vitamins, fresh vegetables, fruit juices, and periodic enemas.

With a greater understanding of why advanced treatments and techniques for evaluating them are needed, we proceed to review the physiological basics of cancer. We focus on the vasculature, the target of anti-angiogenic therapies. With a better understanding of these vessels' importance we will then go on to explain the new MR techniques for interrogating the vascular.

Chapter 3 Physiology

To understand MRI's potential in microvascular imaging, one needs an understanding of basic vascular physiology. The structure of blood vessels and the process of angiogenesis are of particular importance. First we will explore the fundamental role and structure of blood vessels, focusing on the capillaries, of special interest given their role in angiogenesis. The second section looks at some interesting and useful physiological relationships, such as blood flow and blood volume matching. In this work, we investigate and exploit such relationships. Finally, we examine angiogenesis and its evil cousin, tumor angiogenesis. It is our belief that MR can be used to explore the science behind tumor angiogenesis and also provide a useful diagnostic tool to identify regions where it runs rampant both clinically and experimentally.

Vasculature: Normal and Corrupt

Introduction

Humans and other complex multi-cellular organisms have evolved elaborate circulatory systems. Its main purpose is to drive the distribution of nutrients and the collection of waste products from the various and highly specialized tissues in the body. This work is powered by the heart, which pumps blood and transports substances throughout the labyrinth of blood vessels. Among the many fascinating aspects of the circulatory system is that it has the ability to selectively adjust perfusion of different tissues as needed. Not only does this system deliver oxygen and other nutrients, it also serves as the transit system for immune and inflammatory cells. This work will focus on the vascular physiology of the brain and subsequent changes due to tumor angiogenesis.

The heart actually powers two systems, the pulmonary circulation and the systemic circulation. In the pulmonary system blood from the right ventricle is pumped through a one-way valve into the lungs where oxygenation occurs by diffusion in the capillaries. In the normal intact systemic circulation, the total volume of blood is constant (5-6 Liters in humans); regional increases in blood volume must be accompanied by decreases elsewhere. The initial velocity of blood in the aorta is about 33 m/sec, but as the total vascular cross sectional area increases through branching, flow velocity decreases to about 0.3 cm/sec in the capillaries – a crucial adjustment since there needs to be adequate time for diffusion into surrounding tissue.

The caliber of blood vessels decreases going away from the heart through the large arteries to arterioles down to capillaries, and then increases as it returns to the heart from the capillaries to the venules to veins.

The circulation delivers high-pressure fluid to the various organ systems but the pressure must be low at the capillary level to allow adequate exchange across the capillary membranes. Because arterioles have small lumens and thick muscular coats, they are the major regulators of blood flow and at least half of the arterial resistance resides at this level. They are called resistance vessels and pulsations in CBF are damped here resulting in near continuous flow in the microcirculation.

In the beginning of the return circulation, blood is at low pressure already and flows steadily in the venules, which have large lumens and thin walls. Called the capacitance vessels, they are distensible and function as a variable blood reservoir. Most of the blood at any given moment resides in the low pressure side of the circulatory system (75% venous, 20% arterial, 5% capillary).

Cellular Structure

Blood is confined to a closed circuit of vessels lined by simple squamous epithelia, the endothelium, which serves as a physical partition and semi-permeable barrier. As regional functional conditions vary and modulate metabolic need, blood flow to various beds is adjusted by circularly or helically arrayed smooth muscle cells around distributing muscular arteries which can contract reducing vessel diameter as needed.

The walls of blood vessels comprise three basic structural components: endothelium, muscular tissue, and connective tissue. These tissues are arranged into concentric layers (*tunica*). The *intima* consists of endothelial cells, basal lamina, pericytes, subendothelial connective tissue and the internal elastic lamina. The second layer is *media*, which consists of muscles, typically smooth muscle cells, and elastic laminas including the external elastic lamina. The *adventitia* is largely collagenous connective tissue. Regional adaptations in vasculature architecture due to local mechanical or metabolic requirements have influenced the relative weighting of these structural components.

Arteries and veins have distinct structures. The arterial was is thicker than the venous wall to maintain integrity under greater blood pressure. Thickness of the arterial wall diminishes with vessel size, but the wall-to-lumen ratio increases in the periphery. Veins generally have larger diameter and larger lumen than arteries. Blood flow and blood pressure are regulated by changes in arterial lumen size through smooth muscle cell contraction or relaxation, regulated in part by the autonomic nervous system and local metabolic factors. The resistance of a blood vessel is proportional to the 4th power of the diameter, yielding a powerful effect on flow.

Arterioles, the smallest arterial branches (20μm – 100μm in diameter) regulate blood flow into capillary beds. The media smooth muscle cells of arterioles are capable of making dramatic adjustments in lumen diameter that can significantly influence blood flow distribution and pressure. It is in this regime that there is a change from pulsatile to relatively constant blood flow.

Capillaries are blood vessels whose diameters are on the order of those of red blood cells (approx 7 μm). Impressively, despite their small caliber, the capillary network is extensive with 700m^2 of surface area in humans. Endothelial cells line capillaries, supported externally by a thin basal lamina forming a basement membrane. In some capillaries there are pericytes surrounding the capillaries. Capillaries are optimized for rapid exchange of diffusible substances between blood and tissue as they contain low flow and possess very large cross sectional area and have one cell thick walls. Capillary composition can vary, although there are three general types:

- muscle-type – continuous endothelium and basement membrane. Seen in the heart, muscle, lung, skin, and nervous system
- visceral-type – fenestrated endothelium and a continuous basement membrane. Seen in endocrine glands, renal glomeruli, and the gastrointestinal

tract. Transluminal fluid transport 100 times greater than capillaries with continuous endothelium

- sinusoid-type – vascular channels with discontinuous endothelium with little or no basement membrane. Seen in the liver, spleen and bone marrow.

Transcapillary molecular transport has many mechanisms, a subject beyond the scope of this work. Fenestrated and discontinuous endothelial lined capillaries are openly permeable. In the brain, the intercellular junctions are perfectly tight and do not allow passage of substances across the endothelium. This wall preventing transport into the brain parenchyma is called the blood brain barrier (BBB) and is of critical importance to brain function. The BBB protects the brain from undesirable compounds. A frequent effect of brain tumors is the breakdown of the BBB, which allows toxins into the brain. It also allows injected contrast agents like Gadolinium DTPA to extravasate resulting in signal enhancement. We used Gadolinium leakage to measure permeability. In other work we used a blood pool contrast agent that remained intravascular despite BBB breakdown to measure vessel morphometry.

Regulation of CBV and CBF

CBF and CBV are related and controlled in the healthy cerebrovascular. Here we briefly outline the five hallmarks of cerebrovascular management of blood flow and blood volume. This research will use imaging technology to explore the first three of these properties. Failure of such mechanisms could be an important clinical sign of major pathology.

Flow-Volume Matching

Numerous studies have shown vascular transit time to be relatively uniform in the brain. As it is an index of the volume:flow relationship, we know that these parameters are well-matched in normal brain. Subsequently, deviations from this relationship could be a sign of pathology. This has been observed in seizures(Gado, Phelps et al. 1976) and in stroke(Ferrari, Wilson et al. 1992).

CBF, CBV Response to Carbon Dioxide Reactivity

Grubb and others have detailed the normal relationship between blood flow and blood volume in response to changes in $PaCO_2$ (Grubb, Raichle et al. 1974). CO_2 response is driven by the changing extravascular/interstitial H+ concentration. Vessels dilate when pH decreases surrounding the extraluminal surface. CO_2 is not impeded by the blood brain barrier and therefore freely diffuses into brain tissue when introduced via arterial blood. The CO_2 is converted into H+ and HCO_3- causing the required extravascular acidosis and consequent vasodilation. Severinghaus et al. showed that new steady-state values were reached in less than one minute after sharp changes in $PaCO_2$ (Severinghaus, Ozanne et al. 1976). Prostaglandins, glutamate, and and nitric oxide have all been identified as playing a role as intermediaries between pH changes and vasoreactivity. The relationship between CBV and CO_2 has been found to be linear between the ranges of roughly 25mmHg and 70 mmHg. It is within this regime that we adjust $PaCO_2$ and measure CBV.

Autoregulation

Autoregulation is the process by which CBF, and theoretically, CBV are maintained constant under the physiological challenge of changes in perfusion pressure. The autoregulation curve demonstrates that with MABP ranging from 50 to 150 there is no significant change in CBF. This curve is stylized and individual humans and animals can vary in the location and breadth of this plateau. Autoregulation can fail in some pathologic situations including but not limited to: tumor, stroke, aneurysm, and arteriovenous malformation. A recent MRI study examined CBV and CBF changes at various points along this curve (Zaharchuk, Mandeville et al. 1999).

Flow-Metabolism Coupling

As cerebral metabolic rate (CMR) is largely controlled by the amount of the metabolite delivered to the region, it is not surpising that there exists a strong flow-metabolism coupling. This matching allows delivery of the required compound (e.g. oxygen or glucose) in an appropriate level given the local demands of the tissue. High energy requiring regions such as gray matter therefore have higher CBF and higher CMR than white matter, for example. This is a functionally driven relationship and is seen in functional mapping of the brain where activated regions undergo a spike in both CBF and CMRGlu.

Measurement Techniques

Cerebral physiology is an interesting and elusive subject. Blood volume and flow form a foundation of physical function and also have direct impact on mental health. Consequently, these parameters are of great interest in a wide variety of clinical and research settings ranging from cancer and stroke to psychiatry. As important as these parameters are, they have been equally inaccessible in the past. Much like the scrutinization of quantum states in physics, any technique to directly measure intracranial physiology had profound impact on that physiology, rendering the measurement suspect at best. The development of invasive laboratory techniques to more accurately measure cerebral physiology has provided a greater insight into the role of CBV, CBF, and cerebral metabolic rates in normal and diseased states. While these methods are not readily translated to bed-side, they do provide important knowledge.

Recently, imaging techniques like PET and MRI have allowed for non- or minimally-invasive measurements of cerebral physiology parameters with good spatial resolution. It is clear that such techniques offer a huge advantage in that they do not directly disturb the vasculature and physiology that they interrogate. Much work has gone into the development and calibration of these non-invasive techniques, and we develop and utilize new methods in this work.

Due to the intrinsic difficulties of measuring cerebral blood flow and volume, researchers agree only moderately on the true absolute valuesof in normal brain under normal conditions. The values in Table 2 are estimates from Todd *et al.* based on their survey of the range of literature values (Todd, Weeks et al. 1993). There exists a 3-4 fold increase in CBF and CBV in gray matter compared to white matter, not surprising given the highly cellular nature of gray matter and consequently its high metabolic demands. The gold standard in CBF measurements is the Kety-Schmidt method in which catheters are placed in a peripheral artery and the jugular bulb. A diffusible tracer is injected (in their original work – 15% N_2O) and blood concentrations are recorded on both the arterial and venous sides over approximately 20 minutes. Initially, uptake by the brain results in lower venous values. High flow will result in a more rapidly reached equilibrium between the arterial and venous concentrations as saturation is reached. Obviously this technique is invasive and also provides no regional information; only one gross measurement is obtained. But it does allow for the determination of metabolic uptake, by multiplying CBF by the arterio-venous difference in the metabolic substrate of interest (e.g. glucose).

Several radioactive tracer washout methods were developed to gain regional information about CBF. This technique involves injection or inhalation of a diffusible radioactive tracer and measurement of radioactivity washout using one or many extracranial radiation detectors. Washout curves are then fit to a simple exponential decay, or a two-compartment model of washout, representing high and low flow (gray and white matter).

Parameter	**Whole Brain**	**Gray Matter**	**White Matter**
CBF (ml/100g/min)	50	80	20
CBV (ml/100g)	4	4-6	1.5-2.5

Table 2 Values recorded by Todd et al. in humans (Todd, Weeks et al. 1993).

Cerebral Blood Volume and Intracranial Pressure

Intracranial pressure is a parameter of particular interest in clinical management. Given the incompressibility of water and solids, and because the brain is fixed within a nearly rigid container – the skull and dura – increases in the amount of matter within the skull result in increased ICP. This change can have important clinical manifestations. Let us examine the intracranial contents:

- Solids (approx 168g, 12%)
- Tissue water (approx 1092g, 78%)
- Cerebrospinal fluid (approx 75ml, 5%)
- Blood (approx 50 ml, 5%)

At the gross level, basic physics and chemistry govern the interplay between these components. Increase in ICP can result due to the increase in any of these parameters. One of the most profound examples of this occurrence is intracranial neoplasia. Brain tumors are largely solid and a growing tumor will increase the ICP as it compresses the other brain compartments. While none of this material is actually compressible, the CSF compartment can shrink (not increasing in density – simply decreasing in volume and mass). As the tumor initially grows, decrease in the volume of the CSF compartment can compensate. Eventually, this compensatory mechanism is exhausted and ICP begins to more rapidly increase. Blood volume rarely gives way to compensate for increased ICP, indeed, it has been shown and will be explored more fully in this work that tumor growth promotes increases in blood volume. As high ICP may play a role in vasoactivity, measures of CBV may have relevance to ICP.

Other Methods for Determining CBF

Early work on cerebral blood flow involved the detection of the clearance rate of some exogenous compound. Gibbs performed some of the first work in this field in 1933. He measured thermal clearance by inserting a heating element into the brain and measuring the temperature difference between this heater and brain temperature. The heat clearance was then converted to a CBF value given certain assumptions about the density of the tissue and its thermokinetic properties. While such a setup allowed for the continuous measurement of CBF, it was very invasive and approximate due to the non-linear relationship between heat clearance and flow *in vivo*.

Clearance methods took more elaborate forms with both hydrogen and helium clearance used to determine CBF. The hydrogen clearance method involved its buildup, generally through inspiration, to a steady-state saturation. An inserted electrode then recorded the rate of clearance, which is fit to a compartmental model. While more accurate than the thermal clearance method, this technique is still invasive, and the modeling tends to be overly simplified to fit to a mono-exponential residue curve. The true multi-exponential nature of these curves reflects the heterogeneity of flow in the region of measure, likely due to both spatial and temporal heterogeneity. Helium clearance is also performed in this way, but the use of a mass spectrometer permits not only the detection of helium, but also measurement of $PaCO_2$ and PaO_2, providing a much more complete picture of the local physiology. This technique has similar drawbacks: invasiveness and limited spatial information, and is more complicated due to the mass spectrometer element of the experimental set-up.

Laser Doppler Flowmetry can be used non-invasively to measure relative CBF. A probe emits laser light that is scattered by the brain (and anything else in the way) and recorded. The scattered light data is processed to compute microvascular blood volume and red blood cell velocity as CBF. Like clearance methods, it yields only relative values and can measure CBF over time, but only in one non-deep position at a time. It has the added advantage of being a much simpler procedure and can be performed without removing the skull in smaller animals.

The following methods permit the measurement of CBF in multiple regions on the brain simultaneously, although invasively.

Autoradiography is a seminal technique in which a freely diffusible tracer is injected intravenously. The animal is immediately sacrificed, the brain frozen and sliced on a cryotome, and the slices are placed on x-ray film. The amount of recorded radiation in a given time is proportional to the CBF and can be extracted mathematically using a model by Kety, given a known input function (the arterial concentration of tracer due to the controlled infusion).

The microsphere method is similar in that radioactivity is injected and later measured as proportional to CBF. In this case, labeled microspheres, size selected to lodge in the microcirculation, are injected into the left atrium. Assuming adequate mixing of the microspheres in the blood, their distribution represents a measure of flow. This value can be quantified by taking an arterial blood sample both before and after the injection. Quantitative CBF is computed by dividing the activity of the brain by that of the reference blood sample. This method can also provide information about the distribution of blood to various organs in addition to simply measuring cerebral blood flow. It can also be expanded to multiple measurements by utilizing different radioisotopes.

More similar to the original clearance methods is the external detection of radiation following an injection of a radioactive agent (e.g. 133Xe). Multiple detectors can be configured to extract regional CBF data. Multiple measurements in time are also feasible. This method is best suited to larger animals, as in small creatures the spatial resolution of the detectors can be poor compared to the size of the region under investigation. In very small animals, only a globally averaged measurement is possible.

Blood Volume, Glucose Uptake, and Clinical Parameters

It is well known that tumor-spawned vessels have different characteristics than their normally-grown counterparts. Qualitatively, tumor vessels are disordered and dominated by large, dilated, and tortuous vascular structures. Deane and Lantos studied the various phases of vascularization of rat glioma and discovered microvessels on the order of 40μm in the intermediate zone of the tumor (Deane and Lantos 1981). Zama *et al.* assessed the three-dimensional growth patterns of rat gliomas, finding large budding vessels that held blood but with abnormal flow characteristics (Zama, Tamura et al. 1991). Tumor-spawned vessels are also comparable to those incited by wound healing (Dewhirst, Tso et al. 1989). Pathologists have been examining fixed and stained tissue samples since Schwann and Schleiden in the early and mid 1800's who invoked the two key elements of modern histology: microscopy and enthusiastic use of special stains (Vogt 1975). In the brain, histological examination of vasculature is useful in many settings including but not limited to cancer and stroke. The advent of imaging techniques to measure cerebral blood volume has led to the discovery of several important relationships.

Mineura *et al.* have shown using PET imaging the correlation between glucose uptake and tumor grade as well as PET-measured blood volume and grade(Mineura, Yasuda et al. 1986). They measured quantitative regional cerebral hemodynamics and metabolism in gliomas using O-15 and ^{18}FDG tracers, and compared their findings to preoperative histological findings. Hemodynamic and metabolic indices of regional cerebral blood flow (rCBF), cerebral blood volume (rCBV), oxygen consumption (rCMRO$_2$), oxygen extraction (rOEF), and glucose consumption (rCMRGlu) were studied on thirteen preoperative gliomas (including one recurrent case). The average rCMRGI values was 3.00 ± 1.06 mg 100 ml^{-1} min^{-1} (mean ± SD) for 7 low grade gliomas (grade II), and 5.91 ± 3.61 mg 100 ml^{-1} min^{-1} for 11 high grade gliomas (grade III and IV). These results suggested that anaerobic glycolysis increased with malignancy. Another interesting finding of this study was that rCMRglu was markedly reduced in the contralateral grey matter of gliomas in comparison to that of normal volunteers ($p < 0.01$). They suggested this could be a result of increased intracranial pressure and depressed cerebral functional activity. Their measurement of rCBV was significantly higher in high-grade gliomas in comparison with the contralateral gray matter around the sylvian fissure ($p < 0.02$).

Aronen *et al.* investigated the potential relationship between CBV and tumor grade in human gliomas(Aronen, Gazit et al. 1994). Using dynamic spin echo EPI images acquired after gadolinium contrast agent injection, they generated CBV maps from 19 patients with histologically-proven gliomas. They normalized the relative SE-CBV values by the CBV of contralateral white matter. The maximum CBV in these tumors varied with the grade of the tumor. In low grade gliomas ($n=6$), they found $CBV = 1.11 \pm 0.08$, while in high grade gliomas ($n=13$), $CBV = 3.64 \pm 1.59$. The difference between these two groups was statistically significant as measured by pooled t-test with unequal variances ($p = 0.0001$). Through immunohistochemical analysis, they found that MR SE CBV was associated with mitotic activity and vascularity, but not associated with cellular atypia, endothelial proliferation, necrosis, or cellularity. They showed that MR CBV maps provide information not available through traditional anatomical imaging and offers a functional parameter for assessing glioma grade globally and locally.

In previous work, our group demonstrated a regionally specific correlation between tumor relative blood volume (CBV) determined *in vivo* with functional magnetic resonance imaging techniques and tumor glucose uptake determined with fluorodeoxyglucose positron emission tomography (Aronen, Pardo et al. 2000). Regions of maximum glucose uptake were well matched with maximum CBV across all patients ($n = 21$; $r = 0.572$; $P = 0.023$). High-grade gliomas showed significantly elevated CBV and glucose uptake compared with low-grade gliomas, ($P = 0.009$ and 0.008, respectively). Correlations between CBV and glucose uptake were then determined on a voxel-by-voxel basis within each patient's glioma. Correlation indices varied widely, but in 16 of 21 cases of human glioma, CBV and glucose uptake were correlated ($r > 0.150$). These measures were well correlated in all cases when comparing healthy brain tissue in these same patients. Tumor vascularity, as determined immunohistochemically and morphometrically on clinical samples, revealed statistically significant relationships with functional imaging characteristics in vivo. Regional heterogeneities in glucose uptake were well matched with functional magnetic resonance imaging CBV maps. These findings support the concept that there is an association of microvascular density and tumor energy metabolism in most human gliomas and this is likely to have important clinical applications in the initial evaluation, treatment, and longitudinal monitoring of patients with malignant gliomas.

While external detectors can crudely measure a plasma-born radiotracer in large animals or humans, small distances and rapid vascular transit times prevent small animal studies from being performed in this manner. The typical approach in this situation is to administer a nondiffusible, radioactive tracer, kill the animal, remove a sample of the brain tissue and measure the concentration of radiation. During brain removal, intravascular pressures fall to zero, and blood drains from the tissue. Calculated CBV will be artifactually low due to low radiotracer concentration in the tissue from this leakage. Todd et al. utilized microwave fixation to lock radioactive tracers in place, and therefore reduce problems stemming from blood leakage during removal of the unfixed brain (Todd, Weeks et al. 1993).

They measured blood volume as the combination of plasma volume and red blood cell volume in animals killed by decapitation and brain fixation from focused microwave energy. They found significant differences between CBV and CPV obtained by the two methods, but with no difference in CBF (Table 3).

It would be best to have a non-invasive technique that is not so dependent on the method of animal sacrifice, or even better, would not require the animal's or patient's death.

	Decapitation	**Microwave Fixation**	**p-value**
CBF (ml /100g / min)	96 ± 18	101 ± 24	0.6239
CPV (ml /100g)	1.14 ± 0.29	1.74 ± 0.25	0.0001
CBV (ml /100g)	1.63 ± 0.28	2.67 ± 0.33	0.0001

Table 3 From Todd *et al.* (Todd, Weeks et al. 1993). Comparison between post-mortem findings based on sacrifice method. Significant differences depending on method drives the need for a true measure of CBV while the animal is alive.

Tumor Angiogenesis

Angiogenesis

Angiogenesis is the growth of new capillary blood vessels. While recent excitement and research interest has been focused on the particulars of tumor angiogenesis, it is important to understand the general role of angiogenesis in the human body. Angiogenesis is fundamental to human life. In embryology, the formation of blood vessels is absolutely critical to the development of a healthy fetus. This truth is poignantly and sadly illustrated by the thalidomide cases in Germany where children were born with serious defects. Thalidomide turned out to be a potent inhibitor of angiogenesis as well as a sedative. Interestingly, thalidomide is currently in clinical trial as an anti-angiogenic therapeutic. The process of menstruation is also angiogenesis dependent as is natural wound healing.

As illustrated above, angiogenesis is critical to life. Cells cannot function without fresh capillary perfusion. It is not surprising then that we have developed an elaborate system of checks, balances, and redundancies to ensure adequate angiogenesis when needed. This complex system is now being unveiled at the molecular level, as is its role in tumor growth. It is a testament to the rapid pace of science that only thirty years ago this link between angiogenesis and tumor growth was first proposed. It is a powerful reminder to researchers today that this proposal, thirty years ago, was considered outrageous.

In our work, we link MRI parameters with those assocaited with angiogenesis, the growth of new vessels. With these techniques we hope to establish new ways of evaluating not only tumor progress but also blood vessel progress. This dual approach will be of great importance with respect to the application of vascular and angiogenesis based therapies.

Folkman's Hypothesis

In 1971, Judah Folkman proposed a revolutionary view on the role of blood vessels in tumor growth (Folkman 1971). His suggestion was that tumor growth was actually dependent on new vessel formation. At that time, scientists believed that the hypervascularity of tumors was largely due to an inflammatory response of the body against the tumor. If the neovasculature were inflammation mediated, it would function to inhibit tumor formation, providing efficient access to cell destroying mechanisms of the immune system. Consequently, the hypothesis of angiogenesis dependence was quite contrary to accepted tumor dogma.

Folkman's hypothesis of angiogenesis dependent tumors was based on relatively simple assumptions. He realized that tumor cells, like any other cells, require nutrients, oxygen, and waste disposal. As tumors grow, they soon extend beyond the range where the current blood vessels can supply the needs of the tumor. Proliferating cells are metabolically hyperactive so one expected even greater vascular needs from tumor cells compared to its healthy counterparts. If tumors need more vasculature, they must have a mechanism for getting it. This supposition lead to the suggestion that endothelial cells, which line blood vessels, could be signaled to proliferate. Folkman suggested a diffusible chemical signal emitted from tumor cells could function to switch on endothelial proliferation, and consequently activate angiogenesis. This is the fundamental assumption of Folkman's theory of tumor angiogenesis.

There are two other important suggestions from this seminal work. The first, which has garnered great publicity in the past few years, is that angiogenesis could be a new target for the treatment of cancer. Rather than kill tumor cells, one could starve them, and potentially limit the tumor's capacity to grow. Enormous effort is now devoted to exploring this option, although it remains to be seen how effective anti-angiogenesis therapy will be. Specifics regarding anti-angiogenesis therapies in the pipeline will be discussed later.

The second suggestion is that new vessels, sprouted following this tumor-incited activation of angiogenesis, are not "established." It was conventional wisdom at the time that vessels generated concurrently with tumor growth would be similar to vessels created following the process of wound healing. These established vessels would remain present and function forever. The permanence of tumor-sprouted capillaries is likely critical to the long-term efficacy of anti-angiogenic agents. If tumor cells can be made to involute, it is reasonable that anti-angiogenic therapy could do more that slow the growth of a tumor, but could shrink it as well, collapsing recently generated vessels, and consequently killing peripheral tumor cells. If these blood vessels are permanent, it seems likely that these new therapies would only serve to slow or halt tumor progression: certainly a laudable achievement if tumors are halted quickly enough, but disappointing to those who anticipate a full cure.

Evidence That Tumors Are Angiogenesis Dependent

Indirect Evidence

Researchers in the 1970's and 1980's began to explore this blossoming field with great interest. Experiments painted a picture that was strikingly in-line with Folkman's hypothesis of 1971. For a more complete review of the evidence for angiogenesis, see (Folkman 1990). A few of the key results are briefly summarized here:

The necessity of new vasculature has been cleverly shown in several ways. Folkman showed that tumor cells were free to grow indefinitely on a two-dimensional plate as long as the nutrient supply was refreshed artificially by adding fresh medium (Folkman and Greenspan 1975). These same cells when formed into spheroids reached a critical size and could no longer grow, despite the addition of fresh medium. Given the size of these tumors, a balance had been reached between proliferation and death. The difference in the spheroid case from the plate case is that the spheroids had reached a diffusion limit of nutrients, and consequently, a limit to size. This finding added credence to the idea of tumors reaching a (very small) maximum size before an activation of angiogenesis removed this diffusion barrier to continued growth.

In numerous animal models, it has been shown that the rate of tumor growth is initially linear, but at a critical point becomes exponential. This fact was known as far back as 1945, when Algire *et al.* implanted window chambers in mice flanks to directly, although invasively, view tumor progression (Algire G 1945). They saw a change from linear to exponential growth after vascularization, although they where not able to make the causal link. Experiments involving the rabbit cornea showed a similar linear to exponential acceleration following vascularization (Gimbrone, Leapman et al. 1973).

Direct Evidence

Much more recently, scientists have been enabled through the aid of molecular-based tools to directly measure and influence the process of angiogenesis. Given these capabilities, it is now possible to affect angiogenesis and measure the results. These direct methods transcended simple observation; they provided a means of intervention coupled with quantitative and astute interpretation of any changes. These experiments can be divided into two classes: molecular and genetic inhibition of angiogenesis.

Molecular Inhibition

Molecular inhibition can take a few forms. One is the direct application of an angiogenesis-blocking compound. One of the first such compounds derived for this purpose was TNP-470 (a synthetic analogue of fumagillin also known as AGM-1470), a selective inhibitor of proliferating endothelial cells (Ingber and Folkman 1990). It is important to emphasize that this compound does not in any way target tumor cells. Despite this fact, it has been shown in numerous studies to have some (although quite variable) efficacy in the slowdown of tumor progression. While not a tumor-halting agent, it has been shown to retard the growth of tumors in numerous cancer types.

Another method of molecular inhibition is the blocking of tumor-secreted angiogenic factors, chemicals emitted to illicit the growth of new vasculature. Such an approach involves the introduction of a neutralizing antibody of Vascular Endothelial Growth Factor (VEGF). VEGF, also known as Vascular Permeability Factor, has been shown to be a key molecular signal in the induction of new blood vessels. Kim et al. showed in one tumor model that treatment with the anti-VEGF antibody inhibited tumor growth in mice by a staggering 90% (Kim, Li et al. 1993). It must be noted however that this particular model of angiogenesis is solely driven by VEGF, unlike most tumors that involve a complex milieu of factors.

Genetic Inhibition

Genetic methodologies have evoked intriguing possibilities for the advanced and elegant treatment of cancers. There are two main and complementary approaches to genetic treatments for cancer: transfection of tumor suppressing genes and transfection of genes that code for down-regulated tumor factor receptors in endothelial cells. As we begin an era of genetic understanding, each of these methods has great potential to revolutionize cancer treatment.

Tumor suppressing genes can take multiple guises. There are genes that work at the level of proliferation, governing the cell cycle. There are also genes that affect the process of apoptosis, the natural mechanism of cell death. These are topics of great importance, and even greater scope, that I will not directly address here. Another style of tumor suppressing gene is that which encodes for a directly angiogenesis inhibiting protein. Angiostatin is such a protein and its gene has been inserted into mice. Angiostatin is a 38 kD internal fragment of plasminogen and is a specific inhibitor of endothelial proliferation. Cao *et al.* showed that while it had no effect in vitro, in the animal model the transfected gene caused a slowing of tumor growth that was correlated with levels of the angiostatin protein (Cao 1998; Cao, O'Reilly et al. 1998). This is an excellent example of the potential of gene therapy to introduce cancer fighting genes, rather than simply injecting the protein products of those genes.

As mentioned, the other approach to gene therapy involves the introduction of genes that code for altered receptors. If the receptor component of the factor-receptor complex, required for tumor angiogenesis, can be altered, or down regulated, this would be a powerful way to halt the progress of a tumor. Such an approach has now been taken. The growth of brain tumors in mice was significantly inhibited when a dominant negative mutant of the Flk-1 receptor (receptor to VEGF) was introduced into host endothelial cells by a retrovirus. This receptor mutant prevented the formation of new capillary blood vessels in response to VEGF secreted by the tumor(Millauer, Shawver et al. 1994).

Evidence that Metastases Are Angiogenesis Dependent

While the suppression of tumors is an important goal, one notes that most cancer deaths are attributed not to primary tumors but to metastases. Therefore in terms of clinical relevance, the issue of tumor suppression by anti-angiogenesis may actually be overshadowed by the efficacy of metastatic suppression, either limiting the size of metastases or, preferably, preventing them. Here we review some of the key findings regarding the relationship between metastasis and angiogenesis.

There are numerous physical barriers to the shedding and distal seeding of tumor cells. For the presence of clinical metastasis, tumor cells must first migrate to a blood vessel, penetrate it, and survive for a time in the blood stream (Fidler 1978; Fidler and Nicolson 1978). Downstream, this tumor cell must again take hold, again penetrate the endothelium, migrate through the extracellular matrix and thrive in its new milieu. All of those processes, thankfully, are quite difficult. And in each of these processes angiogenesis, or angiogenesis related factors, can play a significant role.

Evidence strongly suggests that tumor cells rarely shed into the circulation prior to tumor angiogenesis (Liotta, Tryggvason et al. 1980). It has also been shown that there is a correlation between the vascular density and the number of metastases, at least in animal models. These findings seem reasonable, as VEGF is also vascular permeability factor. Therefore increases in tumor angiogenesis, partially evoked by increases in VEGF levels, would coincide with increases in vascular permeability, and consequently, increased penetrability of capillaries to tumor cells. Their basement membranes have fragmented and the tumors have a leaky vasculature. As a side note, this fact is critical to typical brain MRI in the clinical setting. These leaky vessels allow gadolinium contrast agent to leak from them into the extravascular space. This causes bright spots on MR film called enhancement. There will be more on this subject in the section on contrast agent techniques.

At the site of distal metastasis, angiogenesis plays a critical role similar to its role at the primary site. Without the ability to incite supplementary vasculature, metastases are limited to similar sizes as are primary tumors prior to vascularization (Chambers 1999). In several studies, including one by Chambers *et al.*, micrometastases were held to 100um to 200um indefinitely because of the lack of angiogenesis. While there is some controversy as to the specifics regarding this process, there is most likely a balance between apoptosis and proliferation, rather than simple non-proliferation (Holmgren, O'Reilly et al. 1995). These conclusions are critical to the future uses of anti-angiogenic drugs. Should metastases be as susceptible to these compounds as primary tumors, one could foresee a much broader and more productive role for these agents in clinical practice. If metastases had been found to be immune, such therapeutics would only be useful in the early stages of cancer. Later diagnosis and treatment by these methods would be fruitless.

The Angiogenic Balance

It has been said that the key to a healthy happy life is moderation. Nowhere is this saying more poignant than in the fine balance of angiogenesis. The disastrous consequences of either too much or too little angiogenesis have been discussed. How then does the body regulate this critical process, maintaining a dynamic balance, shifting the equilibrium to accommodate the body's needs? This delicate fulcrum is shifted by numerous factors, and it is by changing the relative weighting of these factors that the balance is stuck in the healthy individual, and corrupted in cancer.

Table 4 is a more complete listing of the known players in angiogenesis (Caramia, Huang et al. 1998). While this list has grown extensively in the past several years, it is to be expected that many more molecules will be discovered and the mechanisms will be increasingly better understood. While extensive discussion of each of these substances is beyond the scope of this thesis, it is helpful to appreciate the large number of natural substances involved in this process. This listing summarizes out current knowledge of natural, or endogenous, angiogenic molecules. The search for artificial inhibitors of angiogenesis is a major thrust in the field of cancer therapeutics.

Angiogenesis Activators	Function	Angiogenesis Inhibitors	Function
VEGF/VPF Family	Stimulate angiogenesis, permeability, leukocyte adhesion	VEGFR-1; soluble VEGFR-1; soluble NRP-1	Sink for VEGF, VEGF-B, PlGF
VEGFR, NRP-1	integrate angiogenic and durvival signals	Ang2	Antagonist of Ang1
Ang1 and Tie2	Stabilize vessels, inhibit permeability	TSP-1, -2	Inhibit endothelial migration, growth, adhesion, and survival
PDGF-BB and receptors	Recruit smooth muscle cells	Angiostatin and related plasminogen kringles	Suppress tumor angiogenesis
TGF-B1, endoglin, TGF-B receptors	Stimualte extracellular matric production	Endostain (collagen XVIII fragment)	inhibit endothelial survival and migration
FGF, HGF, MCP-1	Stimulate angiogenesis	Vasostain, calreticulin	inhibit endothelial growth
integrins avb3, avb5, a5b1	Receptors for matrix mcromolecules and proteinases	Platelet factor 4	inhibits binding of bFGF and VEGF
VE-cadherin; PECAM (CD31)	Endothelial junctional molecules	TIMPs; MMP inhibitors, PEX	Suppress pathological angiogenesis
Ephrins	Regulate arterial/venous specification	Meth-1; meth-2	inhibitors containing MMP, TSP, and disintegrin domains
Plasminogen activators, MMPs	Remodel matrix, release and activate growth factors	IFN-a, -b, -g; IP-10, IL-4, IL-12, IL-18	Inhibit endothelial migration; downregulate bFGF
PAI-1	Stabilize nascent vessels	Prothrombin kringle-2; antithrombin III fragment	Suppress endothelial growth
NOS COX-2	Stimulate angiogenesis and vasodilation	Prolactin	Inhibits bFGF/VEGF
AC133	Regulate angioblast differentiation	VEGI	Modulate cell growth
Chemokines	Pleiotropic role in angiogenesis	Fragment of SPARC	Inhibit endothelial binding and activity of VEGF
Id1/Id3	Determine endothelial plasticity	Osteopontin fragment	Interfere with integrin signaling
		Maspin	Protease inhibitor
		Canstatin, proliferin-related protein, restin	Unknown mechanisms

Table 4 Enodgenous angiogenesis related factors

Angiogenic Targets For Therapy

Better understanding of the natural mechanisms of angiogenesis, and the roles of specific molecules, is now allowing researchers and physicians to conduct clinical trials. Some of these drugs were synthetically derived based on knowledge of angiogenesis to attack certain pathways or mechanisms deemed particularly sensitive. Others are purified natural proteins that may supplement the body's natural resistance to the tumor's demand for increased vasculature. Table 5 lists the compounds currently in clinical trials for cancer treatment.

Drug	Mechanism
PHASE I	
EMD121974	Small molecule integrin antagonist
Combrestatin A-4 prodrug	Apoptosis in proliferating endothelium
PTK787/ZK2284	Blocks VEGF-receptor signaling
Endostatin	induces endothelial cell apoptosis in vivo
BMS-275291	Synthetic MMP inhibitor
SU6668	Blocks VEGF-, FGF, and PDGF receptor signaling
PHASE II	
CAI	Inhibitor of calcium influx
Squalamine	Inhibits NA+/H+ exchanger
COL-3	Synthetic MMP inhibitor: tetracycline derivative
CGS-27023A	Synthetic MMP inhibitor
TNP-470	Fumagilin analogue; inhibits endothelial proliferation
Vitaxin	Antibody to integrin on endothelial surface
IL-12	Induced interferon-gamma and IP-10
Anti-VEGF Ab	monocolonal antibody to VEGF
PHASE III	
SU5416	Blocks BEGF receptor signaling
Thalidomide	Unknown
Marimastat	Sythetic MMP inhibitor
AG3340	Synthetic MMP inhibitor
Neovastat	Natural MMP inhibitor
interferon-a	inhibition of bFGF and VEGF production
IM862	Unknown

Table 5 Potential therapeutics listed by clinical trial status.

Drug Delivery Issues

There arises an interesting paradox in the application of anti-angiogenic therapy. One major obstacle to cancer treatment by chemotherapy or radiotherapy is the delivery of the agent to the tumor. Tumors are often hypoxic, at least in core areas, and therefore are endowed with some resistance to radiation. These parts of tumor are especially hard to kill by external beam therapy. High interstitial pressure and tortuosity of the vasculature result in difficulties with blood-born delivery. Excess endothelial cells and abnormal perivascular cells contribute to vascular entanglement and hyperpermeability. These abnormalities in concert with increased overall compression of vessels due to a mass effect can cause resistance in the vascular network and impair blood supply on a microscopic scale to certain regions in the tumor, despite global elevations in flow throughout the tumor. Such pathological conditions can impair the effectiveness of traditional chemical and radiation therapies.

Jain et al. raised this issue with the concern that application of anti-angiogenic therapy or anti-vascular therapy could have the effect of pruning and streamlining the vasculature (Jain 2001). A more efficient vasculature my permit more productive distribution of metastases or tumor growth factors. The other potential result of such streamlining is more conducive delivery of nutrients and therapeutics. Such normalized vasculature would still be more permeable and less mature than its normal counterpart. Recent studies have proffered evidence for this kind of normalization – where anti-VEGF or VEGFR activity lead to apoptosis of endothelial cells and decreased in vessel diameter density and permeability.

Since tumors secrete their own growth factors, tumor regression can reduce levels of circulating growth factors. Unfortunately, following such tumor streamlining, there often seems to appear a second wave of angiogenesis as surviving cancer cells proliferate. A danger exists in that multiple cycles of streamlining could result in tumors less dependent of such growth factors. It seems reasonable that a cocktail of variously-acting anti-vascular agents may be useful to solve this problem.

If the goal of anti-angiogenic therapy is stasis, then such anti-angiogenic cocktails seem to be a useful approach. If the goal is to streamline the vasculature to increase the efficacy of other modes of cancer treatment, then treatments must be fine-tuned to balance the level of endothelial and perivascular cells to manipulate function, perfusion, oxygenation, and interstitial pressure. Complicated dose scheduling would be required. The ability to tailor the therapy rests on the ability to know the vascular status during such treatments.

The Case for MRI

The key advantages of magnetic resonance are it's non-invasive nature and its ability to tailor the contrast mechanism to countless biological situations. While other radiographic techniques deliver a dose of radiation during each procedure, MRI is exceptionally safe, even for multiple imaging sessions. These traits make MRI a useful tool for several cancer-related tasks.

Both in the clinic and at the research laboratory, MRI is ideally suited for non-invasive, in vivo tumor evaluation. MR has been used for many years in patients, particularly in cases where three-dimensional evaluation was deemed beneficial and in inaccessible locations. Additionally, MRI offers significant advantage over other techniques (or lack of action) in the following situations:

- Non-invasive, longitudinal monitoring especially of difficult to examine places – In the clinic patients can be scanned repeatedly, on a schedule of days, months, or years. Beneficial in many cases, this is ideal in the event of brain cancer, where intervention is dangerous and not always well advised. The ability to monitor a patient's progress without risky surgery is obviously a great benefit.
- Physiological markers for research – MRI provides surrogate markers for physiological study. Tumor sizing is now routine. Blood volume measurements were introduced years ago. In this work, we investigate microvascularly weighted blood volume and a measure of mean vessel size. Various blood flow metrics have also been proffered in recent years.
- Monitoring the effects of therapeutic agents – One potent application related to the above listed situations is the application of anti-cancer therapy. MRI can be used to follow changes in tumor size following drug therapy, as follow up to radiation or surgery, and more advanced techniques can be invoked to measure permeability or microvascular response to specific therapy or candidate drugs to test their efficacy.

Algire G, C. H., et al. (1945). "Vascular reactions of normal and malignant tumor in vivo." JNCI **6**(73).

Aronen, H. J., I. E. Gazit, et al. (1994). "Cerebral blood volume maps of gliomas: comparison with tumor grade and histologic findings." Radiology **191**(1): 41-51.

Aronen, H. J., F. S. Pardo, et al. (2000). "High microvascular blood volume is associated with high glucose uptake and tumor angiogenesis in human gliomas." Clin Cancer Res **6**(6): 2189-200.

Battegay, E. J., J. Rupp, et al. (1994). "PDGF-BB modulates endothelial proliferation and angiogenesis in vitro via PDGF beta-receptors." J Cell Biol **125**(4): 917-28.

Benaud, C., R. B. Dickson, et al. (1998). "Roles of the matrix metalloproteinases in mammary gland development and cancer." Breast Cancer Res Treat **50**(2): 97-116.

Cao, Y. (1998). "Endogenous angiogenesis inhibitors: angiostatin, endostatin, and other proteolytic fragments." Prog Mol Subcell Biol **20**: 161-76.

Cao, Y., M. S. O'Reilly, et al. (1998). "Expression of angiostatin cDNA in a murine fibrosarcoma suppresses primary tumor growth and produces long-term dormancy of metastases." J Clin Invest **101**(5): 1055-63.

Caramia, F., Z. Huang, et al. (1998). "Mismatch between cerebral blood volume and flow index during transient focal ischemia studied with MRI and GD-BOPTA." Magn Reson Imaging **16**(2): 97-103.

Chambers, A. F. (1999). "The metastatic process: basic research and clinical implications." Oncol Res **11**(4): 161-8.

Deane, B. R. and P. L. Lantos (1981). "The vasculature of experimental brain tumours. Part 2. A quantitative assessment of morphological abnormalities." J Neurol Sci **49**(1): 67-77.

Dewhirst, M. W., C. Y. Tso, et al. (1989). "Morphologic and hemodynamic comparison of tumor and healing normal tissue microvasculature." Int J Radiat Oncol Biol Phys **17**(1): 91-9.

Enholm, B., K. Paavonen, et al. (1997). "Comparison of VEGF, VEGF-B, VEGF-C and Ang-1 mRNA regulation by serum, growth factors, oncoproteins and hypoxia." Oncogene **14**(20): 2475-83.

Ferrari, M., D. A. Wilson, et al. (1992). "Effects of graded hypotension on cerebral blood flow, blood volume, and mean transit time in dogs." Am J Physiol **262**(6 Pt 2): H1908-14.

Fidler, I. J. (1978). "Tumor heterogeneity and the biology of cancer invasion and metastasis." Cancer Res **38**(9): 2651-60.

Fidler, I. J. and G. L. Nicolson (1978). "Tumor cell and host properties affecting the implantation and survival of blood-borne metastatic variants of B16 melanoma." Isr J Med Sci **14**(1): 38-50.

Folkman, J. (1971). "Tumor angiogenesis: therapeutic implications." N Engl J Med **285**(21): 1182-6.

Folkman, J. (1990). "What is the evidence that tumors are angiogenesis dependent?" J Natl Cancer Inst **82**(1): 4-6.

Folkman, J. and H. P. Greenspan (1975). "Influence of geometry on control of cell growth." Biochim Biophys Acta **417**(3-4): 211-36.

Gado, M. H., M. E. Phelps, et al. (1976). "Changes in cerebral blood volume and vascular mean transit time during induced cerebral seizures." Radiology **121**(1): 105-9.

Ganju, R. K., N. Munshi, et al. (1998). "Human immunodeficiency virus tat modulates the Flk-1/KDR receptor, mitogen-activated protein kinases, and components of focal adhesion in Kaposi's sarcoma cells." J Virol **72**(7): 6131-7.

Gimbrone, M. A., Jr., S. B. Leapman, et al. (1973). "Tumor angiogenesis: iris neovascularization at a distance from experimental intraocular tumors." J Natl Cancer Inst **50**(1): 219-28.

Grubb, R. L., M. E. Raichle, et al. (1974). "The effects of changes in PaCO2 on cerebral blood volume, blood flow, and vascular mean transit time." Stroke **5**: 630-639.

Hanahan, D. (1997). "Signaling vascular morphogenesis and maintenance." Science **277**(5322): 48-50.

Holmgren, L., M. S. O'Reilly, et al. (1995). "Dormancy of micrometastases: balanced proliferation and apoptosis in the presence of angiogenesis suppression." Nat Med **1**(2): 149-53.

Ingber, D. E. and J. Folkman (1990). "Control of intracellular pH and growth by fibronectin in capillary endothelial cells." J. Cell Biol. **110**: 1803-1811.

Jain, R. K. (2001). "Normalizing tumor vasculature with anti-angiogenic therapy: a new paradigm for combination therapy." Nat Med **7**(9): 987-9.

Kim, K. J., B. Li, et al. (1993). "Inhibition of vascular endothelial growth factor-induced angiogenesis suppresses tumour growth in vivo." Nature **362**(6423): 841-4.

Kirkpatrick, D. B. (1984). "The first primary brain-tumor operation." J Neurosurg **61**(5): 809-13.

Liotta, L. A., K. Tryggvason, et al. (1980). "Metastatic potential correlates with enzymatic degradation of basement membrane collagen." Nature **284**(5751): 67-8.

Millauer, B., L. K. Shawver, et al. (1994). "Glioblastoma growth inhibited in vivo by a dominant-negative Flk-1 mutant." Nature **367**(6463): 576-9.

Mineura, K., T. Yasuda, et al. (1986). "Positron emission tomographic evaluation of histological malignancy in gliomas using oxygen-15 and fluorine-18-fluorodeoxyglucose." Neurol Res **8**(3): 164-8.

Severinghaus, J., G. Ozanne, et al. (1976). "Measurement of the ventilatory response to hypoxia. A step hypoxia three-minute test." Chest **70**(1 Suppl): 121-4.

Todd, M. M., J. B. Weeks, et al. (1993). "Microwave fixation for the determination of cerebral blood volume in rats." J Cereb Blood Flow Metab **13**(2): 328-36.

Vogt, H. H. (1975). "[The cell 100 years ago]." MMW Munch Med Wochenschr **117**(16): 693-6.

Zaharchuk, G., J. B. Mandeville, et al. (1999). "Cerebrovascular dynamics of autoregulation and hypoperfusion. An MRI study of CBF and changes in total and microvascular cerebral blood volume during hemorrhagic hypotension." Stroke **30**(10): 2197-204; discussion 2204-5.

Zama, A., M. Tamura, et al. (1991). "Three-dimensional observations on microvascular growth in rat glioma using a vascular casting method." J Cancer Res Clin Oncol **117**(5): 396-402.

Chapter 4 Nuclear Magnetic Resonance Foundations

Imaging Basics

Magnetization: The Study of Spins

The basis of nuclear magnetic resonance is the manipulation of the nuclear magnetic moment of protons, generally hydrogen molecules of water. Spin is a fundamental property of matter. Nuclei with an odd number of protons or neutrons have this property, a measure of intrinsic angular momentum. The magnetic moment μ is defined as

$$\mu = \frac{h}{2\pi}\gamma I$$

Equation 1

where h is plank's constant, γ is the gyromagnetic ratio and I is the spin quantum number. Protons have spin ½, and an appropriate vector can represent this quantity. Generally, there is no preferred orientation for proton spins, and therefore given a large quantity of matter (a test tube of water, for example) all the spin vectors cancel each other out. However, if this matter is immersed in an external magnetic field, all orientations are no longer equivalent and in the language of physics, the energy degeneracy is broken. An applied external magnetic field will induce a net magnetic moment in the material. If the magnetic dipole μ of a material is in the opposite direction of the external magnetic field, the matter is termed diamagnetic. In paramagnetic materials, like the hydrogen atoms in water, the magnetic moment aligns with the external magnetic field. Ferromagnetic materials already have a preferred orientation prior to the existence of an external field.

When nuclei are placed in B_0, the energy is given by Equation 2, from a classical torque equation.

$$E = \mu B_0 = \frac{h}{2\pi}\gamma I B_0$$

Equation 2

For spin ½ particles, there are two eigenvalues for the z-component of I = ± ½. So as mentioned previously, we have a splitting of the energy degeneracy yield two separable energy eigenstates as a function of B_0. The calculations determining the energy splitting are demonstrated in Equation 3.

$$E_{\downarrow} = \frac{h}{2\pi}\gamma B_0(-1/2)$$

$$E_{\uparrow} = \frac{h}{2\pi}\gamma B_0(1/2)$$

$$\Delta E = \frac{h}{2\pi}\gamma B_0$$

Equation 3

ΔE is the difference in the two energy levels, and is proportional to the applied magnetic field. It is also proportional to the gyromagnetic ratio, a property of the isotope. For $_1$H, the most commonly used, $\gamma = 4250$ Hz/G or 42.5 Mhz./T. This means that a hydrogen atom will resonate at a frequency of 42.5 MHz in a 1 Tesla magnetic field. The next most commonly used isotope used in NMR is $_{19}$F with $\gamma = 40.1$ Hz/G or .4 Mhz/T. A high gyromagnetic ratio is desirable in NMR, since this leads to greater difference in energy levels, which results in a more easily detectable signal.

Taking nuclei and placing them into a magnetic field we find that they populate both energy levels, although not equally. The ratio of the populations is given by the statistical mechanics - derived Boltzmann equation,

$$\frac{E_{\downarrow}}{E_{\uparrow}} = e^{-\Delta E/kT}$$

Equation 4

where *k* is the Boltzmann constant and *T* is the temperature in Kelvin. For typical laboratory values, there exists a few parts per million difference in the populations, meaning that for every million nuclei in each of these states, there are a few more in the more energetically desirable state. Given this very subtle difference, it is remarkable that all NMR signals essentially derive from this difference in energy eigenstate population. The inherent insensitivity of NMR is overcome by the fact that there are roughly 10^{24} nuclear spins in a cubic centimeter of water. It is also important to note the dependence in B_o and T, as this explains research interest in very low temperature NMR and why large magnets with high field strengths are so desirable for many applications.

Transitions between these two energy levels are possible. From the Boltzmann equation and given that the quantum mechanical parcel of energy is described by $E = h\omega/2\pi$, the frequency of transitions $\omega_{transition} = \gamma B_o$, and is called the larmor frequency. Energy must be applied at the larmor frequency to cause a spin flip, disturbing the equilibrium spin populations from the Boltzmann equation. Equivalently, energy emitted by the system returning to equilibrium will also be confined to this characteristic larmor frequency, in the domain of radio waves.

Manipulating Spins

Heisenberg's uncertainty principle dictates that we can only know the magnitude of a nuclear magnetic moment and one of its components simultaneously. Defining μ_z as the component of the magnetic moment in the direction of the external magnetic field, we can then theoretically locate a single spin quantum mechanically on a cone with values μ in magnitude and μ_z in the **z** direction. We can then place many nuclear moments together in a similar fashion, some in the spin-up, some in the spin-down states. Summing these nuclei we get the net magnetic moment, $M=\Sigma\mu$. Graphically, we see that this summation leaves us with a net magnetic moment in the direction of the magnetic field, with $M_{x,y} = 0$, these components of the vectors (although individually unknowable) canceling out. M_z is on the order of $\Delta E/kT$ from a first order expansion of the Boltzmann distribution.

The equation for torque, applied in this situation to a net magnetic moment is given by the vector cross-product

$$\frac{dM}{dt} = \gamma M \times B = \gamma \begin{vmatrix} \hat{i} & \hat{j} & \hat{k} \\ M_x & M_y & M_z \\ B_x & B_y & B_z \end{vmatrix}$$

Equation 5

In the equilibrium situation, with M solely in the **z** direction, the matrix determinant simplifies to zero, meaning no net torque while at equilibrium. However, it is possible to generate a torque on M by applying another external magnetic field, B_1. The result of an external field B_1 in the **x** direction is a torque about that axis, into the **y-z** plane. The amount of rotation will be related to the strength of B_1 and the amount of time that this field is active. Having performed such a rotation and turned off B_1, we are now in a non-equilibrium state. Now there is a torque caused by the B_0 field in the **z** direction that causes a precession, or rotation, about the **z**-axis. Vectorally, equilibrium has been perturbed in the **z**-component (longitudinally) as well as in the **x-y** plane. Relaxation processes bring the magnetic moment back into equilibrium and can be thought of as two distinct processes with characteristic strengths, defined by the amount of time it takes for that component of magnetization to reach equilibrium. Relaxation in the **z** direction, or longitudinal relaxation is termed T_1 based on the characteristic time for this process. In essence, it describes how spins that have been knocked into the less favorable energy state emit energy and perform the transition back into the more favored state. Because this energy exchange takes place with the local environment, it is called spin-lattice relaxation. T_2 relaxation describes the process by which individual nuclei lose coherence with one another and cause the planar component of the tipped magnetization to shrink, generally much quicker than the T_1 relaxation. T_2 relaxation is called spin-spin relaxation time, based on the model in which inter-spin interactions contribute to decoherence. Of note is the fact that $T_2 \leq T_1$ which can be shown classically through conservation of energy or quantum mechanically following the Heisenburg uncertainty principle.

The most basic NMR experiment involves applying a B_1 magnetic field pulse for a short time, tipping the spins, and recording the signal evolved from observing the relaxation. A Free Induction Decay is recorded by a receiving coil in the transverse (**x-y**) plane as the magnetization precesses about the **z**-axis at the larmor frequency. The fourier transform of this signal vs. time data yields a Lorentzian lineshape describing the signal in the frequency domain, rather than as a function of time.

Spin Echoes and Gradient Echoes

Based on the foundational concepts of magnetization and applied magnetic fields, we create the basic building blocks of experiments in which we perturb equilibrium situations and thoughtfully analyze the characteristics of their relaxation. Two of the main methods used to study nuclear spins focus on the spin-spin (T_2) relaxation. One clever mechanism for interrogating this physical phenomenon is to allow some degree of dephasing and then to reverse this process such that the spins once again come into alignment, causing a sudden re-amplification or echo, of signal. Initially the spins are aligned (coherent) resulting in maximum signal. Natural relaxation properties cause dephasing of the spins. Given adequate time, there is no longer a net magnetization and therefore no signal. The implementation of a reverser of some sort can cause the spins to migrate in the opposite angular direction, back towards the original mean amplitude. Eventually, the spins are once again aligned, causing an echo or re-emergence in signal. The fundamental component, T_2, does indeed describe quantum dephasing of spins. But superposed on this phenomenon are other factors that speed energy loss to the surroundings and return to equilibrium. This effective transverse relaxation time is termed T_2* and includes several other factors including, most importantly for the experiments discussed in this thesis, heterogeneities in the magnetic field. A non-uniform magnetic field, as all are to some degree, speeds the dephasing of spins. Therefore when we discuss transverse relaxation, we speak of the inherent nuclei-based parameter T_2 (or 1/R2) and the effective relaxation rate T_2* (or 1/R2*) which comprises T_2 as well as all other effects. When one measures the free induction decay, plots the magnitude decay as a function of time, and fits the data to an exponential curve, T_2* is being measured. It takes more advanced experiments to accurately measure T_2.

There are two ways to construct a reverser to rephase spins. In the gradient echo method, an initial magnetic field pulse (called $\pi/2$ after the tip angle in radians) rotates the net magnetization into the *x-y* plane. As the spins slowly begin to diphase, a magnetic field gradient is applied over sample material. This gradient is a deliberately changing field that greatly accelerates the process of dephasing. After a time, this gradient is reversed in direction, forcing the spins to refocus. This process is not dissimilar from the natural decoherence but happens much more quickly due to the imposed magnetic field heterogeneity. The spins begin to refocus, proceed through a maximum, and then once again defocus as the spins diphase in the opposite angular direction. The result is a signal echo the characteristics of which can be used in several ways, including the accurate determination of T_2* as well as imaging when used as a component in more advanced pulse sequences. An alternative to echo creation is the spin echo. Spin echoes are generated by a different mechanism than gradient echoes. The experiments begin the same way by preparing the magnetization in the transverse plane. But instead of applying external magnetic field gradients to forcibly dephase the spins and reversing the gradient to rephase them, spin echoes utilize the natural dephasing properties and magnetic field. In the case of spin echoes, natural dephasing occurs and is reversed by inverting the magnetization. Flipping the system has the effect of reversing the direction of spin migration from the net magnetization by switching the direction of the spins while leaving intact all the inherent heterogeneities in the local magnetic field. The effect of this inversion is to cause the spins to refocus, allowing a measurement of T_2, the inherent value of dephasing, as the dephasing and rephasing in this situation were governed by that parameter only.

Imaging Basics

Spatially Identifying Spins

The key to forming images based on magnetic resonance is the localization of signal. One must not only detect signal but one must be able to say precisely from where in the sample that signal originated.

$$B_{total}(x_i) = B_0 + B_G(x_i) = B_0 + x_i \frac{\partial B_z}{\partial x_i}$$

Equation 6

The resonant frequency of spins in a magnetic field is linearly related to the strength of that field. By applying a spatially varying external magnetic field, or magnetic field gradient, it becomes possible to identify the location of a specific signal. Imagine a sample in a field of B_0. Superimposed on top of this is a gradient field that increases with distance in the **x** dir. In this example, $G_x = \delta B_z/\delta x$, and the net magnetic field is Equation 6, where the gradient $\delta B_z/\delta x$ is typically on the order of Gauss/cm. The result is that spins at different locations along the **x**-axis feel slightly different magnetic fields, have slightly different resonant frequencies, and therefore, the frequency in the signal can be matched reliably with location within the sample. In the same way, gradients can be imposed in the other directions as well to isolate regions in all three dimensions. This unit is called a volume element, or voxel, and is limited primarily by the strength of the applied gradients under normal imaging conditions.

Conventional vs. Echo Planar Imaging

The methods of data acquisition often play a limiting role in an imaging experiment. The time it takes to acquire a set of data, or images, must be traded off against the quality of the image and volume of coverage. It is especially helpful to think about image acquisition in frequency space (also known as reciprocal space, k-space, and Fourier space), rather than position space, due to the fact that position (the data of interest) is encoded in the frequency of the spins, the quantity we physically measure.

The NMR signal can be written as follows:

$$S = \int_V e^{-i\Delta\omega t} e^{-t/T_2} e^{-i\gamma\partial B_z/\partial x_i x_i t} \rho(x, y, z) dxdydz$$

Equation 7

Let us review each term. The first term describes the effect of the frequency offset, that is, the difference between the real larmor frequency and the presumptive rotating frame frequency in which most analytical work is performed (for simplicity). It is a unitary phasor (its has rotational characteristics, but the magnitude of this term is unity by definition) and is of no consequence here. The second term is the exponential decay term due to the spin-spin relaxation, where T_2 is the time required for the signal to drop in intensity from S_0 to S_0/e. The third term is written in its most general form. It describes the effect of the magnetic field gradients applied during imaging. It too is a unitary phasor, but is very important because it contains the spatial coding in all directions. The term $\mathbf{x_i}$ refers to an arbitrary direction. In conventional imaging, this term would be repeated three times, with $\mathbf{x_1}$ referring to **x**, $\mathbf{x_2}$ referring to **y** and $\mathbf{x_3}$ referring to **z**. In reality, there can be an arbitrary number of gradients in any direction. Such a technique forms the basis of diffusion imaging, a topic aside the scope of this thesis. ρ(x,y,z) is the three-dimensional spin density, describing the location of all spins in the sample material. All of these terms are integrated in space to give the NMR signal.

As mentioned previously, it is advantageous to discuss data acquisition in frequency space. For simplicity let us discuss a situation in which there is a gradient in only the **z** dir. In the k-space picture, the gradient term of the signal in Equation 7 can be simplified to e^{-ikz} where $k = \gamma\ \delta B_z/\delta x\ t$. K is a wavenumber and corresponds to a wavelength as $\lambda = 2\pi/k$. The gradient term is an oscillator, as expressed in the sinusoid nature of the graphs. The first graph shows the signal (remember the signal is the vector component in the **x-y** plane) as a function of distance along the **z**-axis at a particular time after the application of the gradient. The gradient has created a winding helical pattern in the spins in the sample. At some time later, we look at the same region and see that this helical pattern has tightened; the nodes and anti-nodes are closer together. The k-value is inversely proportional to the wavelength of this oscillation. So we see that by increasing the k-value we tighten the spiral forming what has been called a magnetization grating. It is the wavelength of this grating that is a limiting factor in imaging resolution. From the definition of k, we may conclude that stronger gradients and increased gradient activation time can provide greater spatial resolution. Colloquially, this is referred to as going out farther in k-space, or in other words, sampling higher spatial frequencies, which translates directly into smaller spatial distances and higher resolution.

In a real three-dimensional object, k-space is sampled in all three directions(x,y,z) at various levels of k. Each dot corresponds to a data point, where the spatial frequency of the object has been measured at numerous points in the x and y directions. Again, the farther into k-space one samples, the greater the resolution of the resulting image. The path in which these data points are sampled, and the spacing of the samples is a large topic of discussion (the reader is referred to one of many texts that cover sampling theory in great detail).

Susceptibility NMR

Steady-State Methods

Magnetic Susceptibility

Magnetic susceptibility is the response of the internal magnetization of a substance to the application of an external magnetic field. In NMR, the magnetization of study is the magnetization of the nuclei, not of the electrons. Generally, materials are classified by their bulk magnetic properties, which are primarily defined by the electrons, because magnetic moment is inversely proportional to mass.

Paramagnetism is the tendency for a material's magnetic moment to line up parallel with an applied external magnetic field. This is in contrast to diamagnetism where the moment tends to line up anti-parallel. In transition metal ions like gadolinium and dysprosium, some orbital electrons are unpaired and therefore possess both net spin and angular momentum. These electrons are randomly oriented until the sample is placed in a magnetic field. In the case of paramagnetism, the overall magnetic field is enhanced by the addition of the induced magnetic field. The change in magnetic field is given by

$$M = \chi B_0$$

Equation 8

where M is the induced magnetization, and χ is the magnetic susceptibility of the material (positive for paramagnetic, negative for diamagnetic). Greater field strengths result in greater induced magnetization until a saturation limit is reached.

The Physics of Susceptibility Contrast

The relaxation of excited spins is governed in part by the inhomogenieties of the magnetic field in which the spins exist. Such inhomogeneities can be classified as either recoverable or irrecoverable. Recoverable inhomogeneities are those in which the spins can pass through a change in magnetic field and then be forced backwards through the same field change, thereby undoing the addition phase incoherence invoked by the magnetic field inhomogeneity. Spin echoes can refocus the effects of such inhomogenities. The relaxation rate corresponding exclusively to dephasing that is recoverable is $\Delta R_2 = 1/T_2$. $\Delta R_2{}^*$ includes the effect of both the recoverable and irrecoverable field inhomogeneities.

When a group of freely diffusing spin experiences changes in local magnetic field due to the interface of two magnetic field susceptibilities, those spins lose additional phase coherence with each other on top of the inherent transverse relaxation. The susceptibility-induced phase decoherence can be expressed as the integral of the spin phases as a function of time:

$$S(t) = \frac{1}{V}\int_V d\vec{r} \int_\phi d\phi \cdot p(\phi(t), \vec{r}) \cdot e^{i\phi(t)}$$

Equation 9

This integral sums all the paths in space, with each spin acquiring a phase φ in time t. $P(\varphi(t),\mathbf{r})$ is the probability distribution governing the path of a spin and its subsequent phase shift given that path through the local magnetic field. In the situation of contrast agent within vasculature, S(t) is a very complex function that depends on the following physical parameters: susceptibility difference ($\Delta\chi$) between the contrast agent containing and non-contrast agent containing compartments; vascular volume fraction; size distribution of the vessels; and NMR pulse sequence parameters.

Analytical and numerical techniques have been applied to solve this difficult problem. In certain simplified models, it is possible to mathematically solve Equation 9 exactly. In more complex models, simplifying assumptions can be made to allow for analytic solutions. In the most complex situations, which involve many of the most interesting situations in physiology and medicine, it has been shown that numerical solutions provide an accurate and more precise solution than analytic models, because the number of simplifying assumptions is generally reduced. Next we explore some of the seminal earlier work in both analytical and numerical modeling of susceptibility contrast and its effect on the NMR signal.

Analytical Methods

The effects of magnetic susceptibility variations are known to have significant impact on the NMR signal. Much effort has gone into analytically describing the effects of diffusing spins in such environments.

Hahn's original work describing spin echoes involved the effect of Brownian motion on spins experiencing a uniform gradient. Later, Carr and Purcell repeated and extended aspects of this work and examined the effects of diffusion on free precession (Carr and Purcell 1954). They also derived an expression for spin echo signal attenuation under time independent gradient field perturbation:

$$S = e^{-\sigma^2/2}$$

Equation 10

where $\sigma^2 = 1/6\ D\ T_E^3\ \gamma^2\ G^2$, where D is the diffusion constant, γ is the gyromagnetic ratio, TE is the echo time, and G is the gradient amplitude. This result forms the basis for the monte carlo simulations upon which much of the presented susceptibility contrast data is interpreted. As this attenuation parameter varies with the diffusion constant, this fact has been exploited to create diffusion maps, which have many research and clinical uses. Torrey added a diffusion term to the bloch equations to create a solvable generalized equation for signal loss due to proton diffusion in magnetic gradients (Torrey 1956). Weisskoff et al used these equations to develop scaling rules to predict behaviors under various circumstances (Weisskoff, Zuo et al. 1994).

Generalization from linear to non-linear gradients was necessary for work relevant in vivo. Packer measured T_2 on molecules diffusing through gradients derived form the heterogeneity of striated muscle. Glasel studied the effects of nonlinear gradients from water and glass bead systems and calculated field strengths at the surface of microscopic perturbers (Glasel 1970). These results were then extended to cell suspensions and tissues to better understand the susceptibility issues of *ex vivo* samples. Brindle et al studied transport and metabolism in cells. Brown et al showed that T_2 changes in erythrocyte suspensions were largely caused by diffusion through field gradients at the convex membrane boundaries (Brown, Ribeiro et al. 1983).

The classification of susceptibility contrast has evolved into three regimes, determined by the relationship between the rate of diffusion of the spins and the rate of spatial variation in local field strength. The characterization of an environment is determined by many factors including its geometric, dynamic, and magnetic properties. These regimes are described by the following terms: motionally narrowed, intermediate, and linear gradient. τ_D is the diffusive correlation time describing the time for a spin to experience a local magnetic field perturbation. $\delta\omega$ is a characteristic change in larmor frequency on the surface of such a perturber. These quantities are defined as follows:

$$\tau_D = R^2 / D$$
$$\delta\omega = \gamma B_{eq}(R)$$

Equation 11

where R is the radius of a perturber and $B_{eq}(R)$ is the magnetic field on the surface of the perturber. We now address each regime and their limitations.

Motionally Narrowed Regime

Under the condition of $\delta\omega$ times $\tau_D << 1$, diffusion is fast with respect to the spatial variation of the field perturbations and the system is described as motionally narrowed. Spins experience a range of magnetic fields present within the sample, and sample many if not all of them. Modeling of such interaction requires the spatial averaging over protons and over the spectrum of larmor frequencies due to the spatially varying magnetic fields. Gillis and Koenig examined transverse relaxation of protons in solution induced by the diffusion of protons in the outer sphere environment of impenetrable magnetized spheres of uniform size and applied their results to explain the relaxation of erythrocytes and other materials (Gillis and Koenig 1987). They formulated the relaxation rate due to a spherical perturber as:

$$\Delta R2 = 16\tau_D f(\delta\omega)/135$$

Equation 12

where the change in T_2 relaxation is inversely linear with the diffusion constant and quadratic with magnetic field and susceptibility difference. They also concluded that in the regime of motional narrowing with perturber volume held constant, a smaller number of larger particles yielded more ΔR_2 than a greater number of smaller particles. It is notable that outer sphere relaxation theory, upon which this formula is derived, takes into account only one perturber and therefore no overlap of the magnetic field due to neighboring particles or perturbers. Subsequently, the foundation for this work is not clearly extendable into fast diffusion rates or strong field perturbers.

Linear Gradient Regime

This regime takes place at the other extreme, where diffusion is slow compared to the spatial variation in magnetic fields, i.e. $\delta\omega\tau_D >> 1$. Here, protons sample only a small amount of the range of magnetic fields in a given time unlike the previous motionally narrowed regime, where they are assumed to sample all fields within a characteristic time, experiencing overall an averaged magnetic field. The name linear gradient regime comes from the fact that if spins are moving slowly through changing fields, the spin experience can be locally described as a linear gradient, and over time as a series of linear gradients, for which attenuation factors are well known. By modeling the distribution of linear gradients throughout space, one can derive expressions for the ΔR_2 relaxation enhancement. In situation where diffusing spins do not feel significant magnetic field perturbations during a T_E period, the ΔR_2 relaxation is not increased, but ΔR_2* does increase due to loss of internal local phase coherence.

Majumdar and Gore derived the following expression for transverse relaxation enhancement in a spin echo experiment:

$$\Delta R2 = (\gamma\sigma_G TE)^2 D/12$$

Equation 13

where σ_G^2 is the variance of the internal gradient distribution induced by the perturbation. From this, one predicts a linear dependence of relaxivity on diffusion.

Intermediate Regime

Previous analytical work is interesting particularly from a theoretical standpoint. Some applications have evolved that do involve these regimes, most notably oil logging. However, application to *in vivo* biology is limited in that there are few systems that correspond to either the motionally narrowed or linear gradient regimes. It has been shown that numerical techniques are required to relate ΔR_2 transverse relaxation to biophysical parameters.

Let us explicitly examine why magnetic susceptibility contrast due to blood vessels is particularly wedged into the intermediate regime. As discussed previously, the parameter $\delta\omega\tau_D$ defines the appropriate regime. Let us examine typical parameters in one of the imaging experiments contained in this thesis. Contrast agent is trapped within the vascular space. Our histological examination and literature present a typical capillary radius in tumor R = 6μm. Given a diffusion constant D ≈ 1 x 10^{-5} cm^2s^{-1}, τ_D defined as $R^2/D \approx$ 36ms. At 2 Tesla, and with a susceptibility difference between intracapillary plasma volume filled with contrast agent and extravascular water $\Delta\chi$ = ppm, then:

$$\delta\omega \approx \gamma \Delta X \chi B_0 \tau_D \approx 10$$

Equation 14

and therefore clearly does not fit into either the motionally narrowed or linear gradient regime.

Numerical techniques are required to explore the relationship between field perturbations and diffusing spins in this intermediate regime. But as simulations become more accurate in modeling complex systems, probabilistic solutions such as monte carlo sampling have profound advantages. Higher order biological characteristics can be added and their relative impact assessed. Monte Carlo simulations based on the work of Boxerman and Weisskoff form the basis on which our experiments interrogating tumor vasculature are based(Boxerman, Bandettini et al. 1995).

Monte Carlo Methods

Basics of MC

Magnetic susceptibility-induced MR signal changes produced by both exogenous (Gd-DTPA) and endogenous (deoxyhemoglobin) intravascular contrast agents depend upon the size and geometry of the vessels in which the agents are compartmentalized, the fraction of vascular space occupied by the contrast agent (f_v), the susceptibility difference ($\Delta\chi$) between the compartmentalized agent and the surrounding tissue, the field strength, and specific pulse sequence-dependent parameters. As discussed, analytical solutions for this complex interdependence have been derived previously for limiting cases including the motionally narrowed and linear gradient regimes, although this complex relationship is often inaccessible with analytical techniques and is best elucidated with numerical methods. We also briefly described some previous numerical models of susceptibility contrast, and addressed some shortcomings of these techniques for accurately modeling susceptibility contrast *in vivo*.

The theoretical foundation of much of this work is a Monte Carlo model created and implemented by Boxerman et al in an attempt to generate more realistic phase distributions. This Monte Carlo routine computes a signal attenuation, S(t), based upon the expectation of proton phases accumulated during time t due to susceptibility-induced perturbations of the homogeneity of the applied magnetic field:

$$S(t) = \left\langle e^{i\phi(t)} \right\rangle$$

Equation 15

From Equation 9, it is evident that the expectation value actually consists of three components: $p(\phi(t),\vec{r})$ is the probability density function for a proton starting at initial position $\vec{r}$ within volume V to acquire phase ϕ by time t, and the entire expectation is taken over all configurations of magnetic field perturbers. For each configuration, an expectation value is computed over both the initial positions of the protons and, for each initial position, all possible paths through the medium. The Monte Carlo methods used herein accumulated the phase of N_p randomly distributed protons:

$$S(t) = \frac{1}{N_p} \sum_{n=1}^{N_p} e^{i\,\phi_n(t)}$$

Equation 16

where $\phi_n(t)$ is the phase of the nth proton at time t. Monte Carlo estimation is therefore actually used twice: once explicitly to obtain the expectation over starting locations, and once implicitly as the stochastic walk of the protons generates proton phases that must be distributed like $p(\phi(t),\vec{r})$.

In the Monte Carlo simulations described below, the following steps were taken to produce a Monte Carlo estimate of the change in imaged transverse relaxation rate for gradient echo and spin echo acquisitions (adapted from Boxerman, Ph.D. thesis, 1994).

(1) A proton was placed initially at the origin of a simulation "universe", and surrounded by randomly distributed magnetic field perturbers with radius R and a susceptibility difference $\Delta\chi$

between the intra- and extra-perturber space. Unlike previous Monte Carlo simulations they did not assume a periodic distribution of the magnetic field perturbers. The size of the simulation universe depended on the diffusion coefficient (D), the maximum observation time (TE), and the size of the perturbers (R). Each proton commencing at the origin took a random walk, and was expected to diffuse within a cube with edge 2A by a given observation time, where $A=\sqrt{2\ D\ TE}$ is the expected diffusion distance in one dimension during TE, and D (1 x 10^{-5} cm^2s^{-1}, a value typical of cerebral cortex and used for all simulations unless otherwise noted) is the diffusion coefficient. The perturbers were distributed randomly to fill a volume fraction f of a larger cube with edge 2B, where $B = A + k\ R$. That is, the size of Region B was chosen to be roughly twice the RMS diffusion distance at the end of the simulated MR experiment plus a "buffer" region to minimize boundary effects at the edge of the expected path for each proton. The extent of each proton's walk was not monitored to insure that the proton did not wander beyond the boundary of Region B. It is conceivable, therefore, that some protons reached the outer extremes of the universe in which the desired volume fraction of perturbers did not exist locally. However, an appropriate value of k for minimizing these boundary effects was determined by estimating relaxivity change for increasing values of k and selecting a value for which larger k introduced insignificant change.

(2) For every time step, Δt, during the random walk of each proton, stochastic proton diffusion was simulated by choosing a Gaussian random displacement, with zero mean and standard deviation $\sigma=\sqrt{2\ D\ \Delta t}$, in the $\hat{x}$, $\hat{y}$ and $\hat{z}$ directions. Each proton took $N_s = 50$ steps per $\Delta TE = 10$ ms (time step $\Delta t = 0.2$ ms), corresponding to a σ to R ratio between 0.6 (R = 1 μm) and 0.006 (R = 100 μm). An appropriate value for N_s was determined by estimating relaxivity change for increasing N_s and selecting a value for which larger N_s introduced insignificant change.

(3) The magnetic field perturbation at each proton position during each random walk was evaluated by summing the $\hat{z}$-component of the susceptibility-induced magnetic field perturbation, ΔB_Z, contributed by each magnetic field perturber. Because $\Delta\phi << 1$ for all $\Delta\phi$ values studied, it was assumed that the field perturbations from all magnetic field perturbers could be simply superposed. Furthermore, only the $\hat{z}$-component of the perturbation was considered because $B_0\hat{z}$ is the dominant applied field.

(4) The phase accumulated by the nth proton during each step was evaluated by trapezoidal integration

$$\Delta\phi_n(t) = \gamma\ \Delta B_z\ \Delta t$$

and steps (2)–(4) were repeated until the proton had diffused for the maximum observation time, typically 100 ms. Spin echo (not CPMG) and gradient echo phases were estimated every 10 ms from a single time series by storing the $\phi_n(t)$ that evolved in each 5 ms interval and combining the phases with phase inversions appropriate for each TE. Steps (1)–(4), including the re-randomization of all perturbers (for computation simplicity), were repeated for each of N_p protons (typically 4 x 10^4). An appropriate value for N_p was determined by estimating relaxivity change for increasing N_p and selecting a value for which larger N_p introduced insignificant change.

(5) Finally, estimates for SE and GE signal attenuations, S(t), were produced from the phases of the individual protons. The associated transverse relaxivity changes $\Delta R2$ and $\Delta R2^*$ were estimated by computing:

$$\Delta R2(t), \Delta R2^*(t) = -\frac{\ln(S(t))}{TE}$$

using the SE and GE signal attenuations, respectively.

The following details describe those aspects of the Monte Carlo methodology that pertain exclusively to the simulations involving cylindrical magnetic field perturbers. A geometrically simple yet largely reasonable model for magnetized blood vessels in an imaging voxel is a random distribution of cylinders with infinite extent. For $D = 1 \times 10^{-5}\ \mathrm{cm^2 s^{-1}}$ and TE = 100 ms, the expected one-dimensional proton diffusion distance $\Lambda/2 = \sqrt{2\ D\ TE}$ is roughly 14 μm, which is significantly less than a typical capillary segment length. This suggests that the infinite cylinder model is a reasonable approximation locally.

An infinite paramagnetic cylinder with radius R at an angle ϕ with an external field $B_0\hat{z}$ perturbs the applied magnetic field sensed by a proton at cylindrical coordinates r and by an amount ΔB_z

$$\frac{\Delta B_z(\rho,\varphi)}{B_o}=\begin{cases}2\pi\Delta\chi\left(\frac{R}{r}\right)^2\cos2\varphi\sin^2\theta, & r\geq R\\ \frac{2\pi}{3}\Delta\chi\left(3\cos^2\theta-1\right), & r<R,\end{cases}$$

where r is the distance between the proton and the axis of the cylinder, θ is the angle between the proton and the projection of B_O in a plane orthogonal to the axis of the cylinder, and $\Delta\chi$ is the volume susceptibility difference between the intra- and extra-cylindrical space.

Modeling of vasculature

To compare predictions of their Monte Carlo model with experimental data and to interpret *in vivo* signal changes, Boxerman et al developed a simplified vasculature with volume distributed between microvessels (denoted by radius R_C and volume fraction f_C) and macrovessels (denoted by radius R_V and volume fraction f_V). They chose $R_C = 3$ μm for microvascular representation, and for macrovascular size they compared models with $R_V = 25$ μm and $R_V = 100$ μm. $R_V = 25$ μm is the radius for small venules, but is significantly smaller than the radius for large veins. At R = 25 μm $\Delta R2^*$ reached a plateau (i.e. is not size dependent) and therefore they predicted quantitatively similar behavior for a vascular model that incorporates a larger R_V. The model, however, is more sensitive to the choice of R_V for SE acquisitions, since $\Delta R2$ decreases monotonically with cylinder size for macrovessels (R exceeding 10 μm for most $\Delta\chi$). They therefore compared results for models with $R_V = 25$ μm to those with $R_V = 100$ μm to determine the effect of macrovascular representation. They also assumed equal volume distribution between capillary ($R_C = 3$ μm) and macrovascular ($R_V = 25$ μm or $R_V = 100$ μm) components of the vasculature, and referred to this balanced vascular model as the "equidistributed" vascular model. This model is based upon literature values for capillary (2%) and total (4%) volume fraction in cortical gray matter. Sample signal change curves from the work of Boxerman et al are included in Figure 1.

Volume Fraction Dependence

They found the ratio of $\Delta R2^*$ and $\Delta R2$ to be proportional to the ratio of volume fractions for $R = 1 - 100\ \mu m$. These results predict linear volume fraction dependence over a physiological range of fv. The interpretation of the integral of $\Delta R2(t)$ as a relative measure of CBV requires that $\Delta R2$ be proportional to f_v. For physiological f_v, recruitment-based increases(i.e. two regions with similar vascular composition but different volumes) yield increases in $\Delta R2^*$ and $\Delta R2$ that are proportional to the increase in f. This linear recruitment-based f dependence is predicted for a vasculature composed of any combination of vessel sizes. Hence the integral of $\Delta R2(t)$ correctly reflects differences in rCBV between regions with recruitment-based changes in volume within the regime of reasonable physiological or pathological blood volume fractions.

$\Delta R2^*$ and $\Delta R2$ are quite linear over the physiologically relevant range of fv for both models, suggesting that linearity with f is a reasonable assumption regardless of the mechanism of volume increase. For fluctuations in f between 4 and 6% (i.e. 50% hypervascularity), the mechanism of volume change influences $\Delta R2^*$ and $\Delta R2$ by less than 10% at $\Delta\chi = 1 \times 10^{-7}$ and 4×10^{-7}. The (general) linearity predicted for the volume fraction dependence is demonstrated experimentally by comparing gray and white matter relative CBV estimates in high resolution SE CBV maps. Aronen et al. computed a gray:white CBV ratio of 2.32 ± 0.32 over 19 patients, which agrees very well with the ratio of 2:1 found in the PET literature(Aronen, Glass et al. 1995).

From Boxerman et al, Table 6 summarizes the inter-relationships of diffusion, transverse relaxivity, vascular compartmentalization and imaging sequence(Boxerman, Hamberg et al. 1995). In gradient echo acquisitions, an increase in diffusion constant lowers $\Delta R2^*$ in the microvessels while having little effect in the larger vessels. The same effect holds in the microvessels with spin echoes, but in spin echoes, diffusion increases increase $\Delta R2$ as well.

	Spin Echo	**Gradient Echo**
Small Compartments	Increase D, decrease ΔR2	Increase D, decrease ΔR2*
Large Compartments	Increase D, increase ΔR2	Increase D, same ΔR2*

Table 6 Inter-relationships between diffusion, transverse relaxivity, vascular compartmentalization and imaging sequence. (Boxerman, Hamberg et al. 1995)

Superparamagnetic Methods

Ultra Small Particle Iron Oxides (USPIO)

Superparamagnetic compounds orient their magnetic dipoles quickly and strongly in the direction of an applied magnetic field. The resulting induced magnetic field is much greater that that of a paramagnetic substance. The linear relation of Equation 8 still holds true at low and moderate magnetic fields, but the effect saturates at high fields. When the external field is removed, the induced moment vanishes without hysteresis.

Superparamagnetic contrast agents have been used in animal models for enhancing contrast in rat brain, rat liver, and heart. A new class of ultra small iron oxide contrast agents (USPIO) is being developed. These agents allow for passage into almost all compartments of the vasculature while remaining intravascular in most situations. Such agents are already saturated in the 2T regime in which this work was carried out.

MION

Monocrysalline iron oxide nanoparticle compound (MION) is a stable colloid that enables target specific MR imaging (Weissleder, Stark et al. 1989). Shen et al. determined specific physicochemical properties of this compound, used as an intravascular contrast agent in our studies (Shen, Weissleder et al. 1993). MION consists of hexagonal shaped electron dense cores of 4.6 ± 1.2 nm in diameter. Each core has an average of 25 ± 6 dextran molecules attached (10kD), creating a hydrodynamic radius of 20 nm as determined by laser light scattering experiments. MION is superparamagentic with induced magnetization of 68 emu/g Fe at 1.5 Tesla. R1 and R2 relaxivities of MION are 16.5 and 34.8 mM-1 sec-1 respectively under standard conditions and 0.47 T. They found a detectibility threshold in liver less than 50 nmol Fe/g.

MION's relatively large size is near-ideal for intravascular studies. A significantly larger compound may have difficulty sampling all levels of the vasculature. A significantly smaller compound, such as Gado-DTPA has an extravasation rate that seriously complicates blood volume measurements, although correction algorithms do exist (Weisskoff, Boxerman et al. 1994).

Total CBV

The quantitative understanding of magnetic susceptibility perturbations in an applied field permits the determination of vascular space. With the aid of a contrast agent that remains intravascular in the time frame of the MR experiment, one can create a signal change that is proportional to the blood volume (Rosen, Belliveau et al. 1991; Rosen, Belliveau et al. 1991). When such an agent is injected intravacularly, magnetic susceptibility perturbations are induced. If the amount of contrast agent present in a voxel is proportional to the MR signal change caused, then one has a marker for the amount of agent present and consequently, the amount of accessible vasculature. In the case of gradient echo signal acquisitions, we see that the relaxivity based on cylindrical perturbers beyond several microns is flat (Figure 1). So this measurement correlates nicely with total vascular space or as named in the MR literature, blood volume. In brain imaging, this term is generally called cerebral blood volume (CBV). Brain imaging is a special case because of the presence of the blood brain barrier in which the tight endothelial junctions prevent contrast agent leakage from the vasculature. We, and others, have shown MION to remain intravascular in rat brain tumors, despite disruption of the BBB (Weissleder, personal communication) (Dennie, Mandeville et al. 1998).

Microvascularly weighted CBV

Monte Carlo modeling has elucidated the relationships between changes in transverse relaxivity due to magnetic susceptibility perturbation and the size of the perturbers. It has also detailed the differences in relaxivity between $\Delta R2^*$ and $\Delta R2$, signal recalled by gradient echo or spin echo acquisitions respectively.

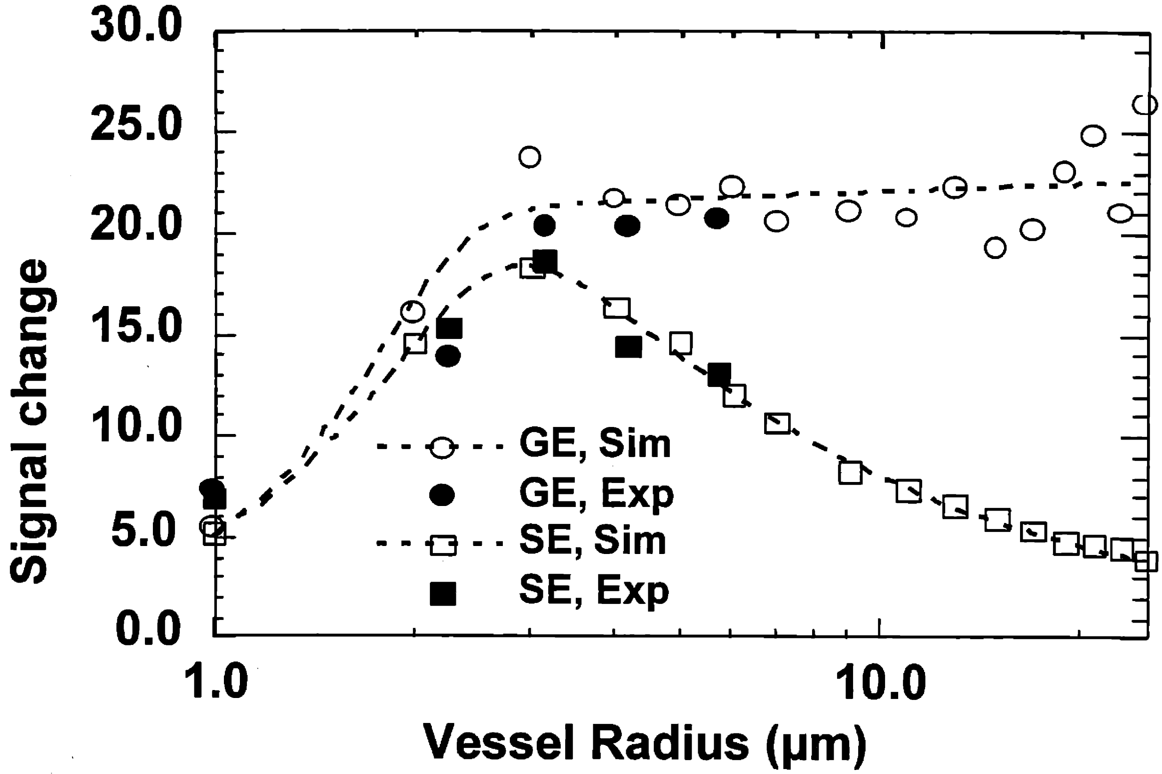

Figure 1 ΔR2* and ΔR2 relaxivity for fixed Δχ, TE, and D as a function of vessel radius and echo type. Comparison of theory and experiment. From (Boxerman 1994; Weisskoff, Zuo et al. 1994)

As seen from the graph of relaxivity based on perturber size (Figure 1), the SE reactivity takes a different form than the GE reactivity. While the GE reactivity is largely flat, the SE reactivity peaks around 2 microns (the exact peak is a function of delta chi and TE) and then decreases again. Above roughly 20 or 30 um, there is very little change in transverse relaxation due to such great perturbers. We can exploit this happenstance of spin physics and utilize SE based measurements of ΔR2 to provide a microvascularly weighted blood volume. As with gradient echo blood volume, the amount of blood, *i.e.* the vascular space causes the signal change, but the effects from the larger vessel is mostly excluded. This microvascularly weighted blood volume is particularly helpful to image capillary sized objects, a size regime of great interest in tumor angiogenesis.

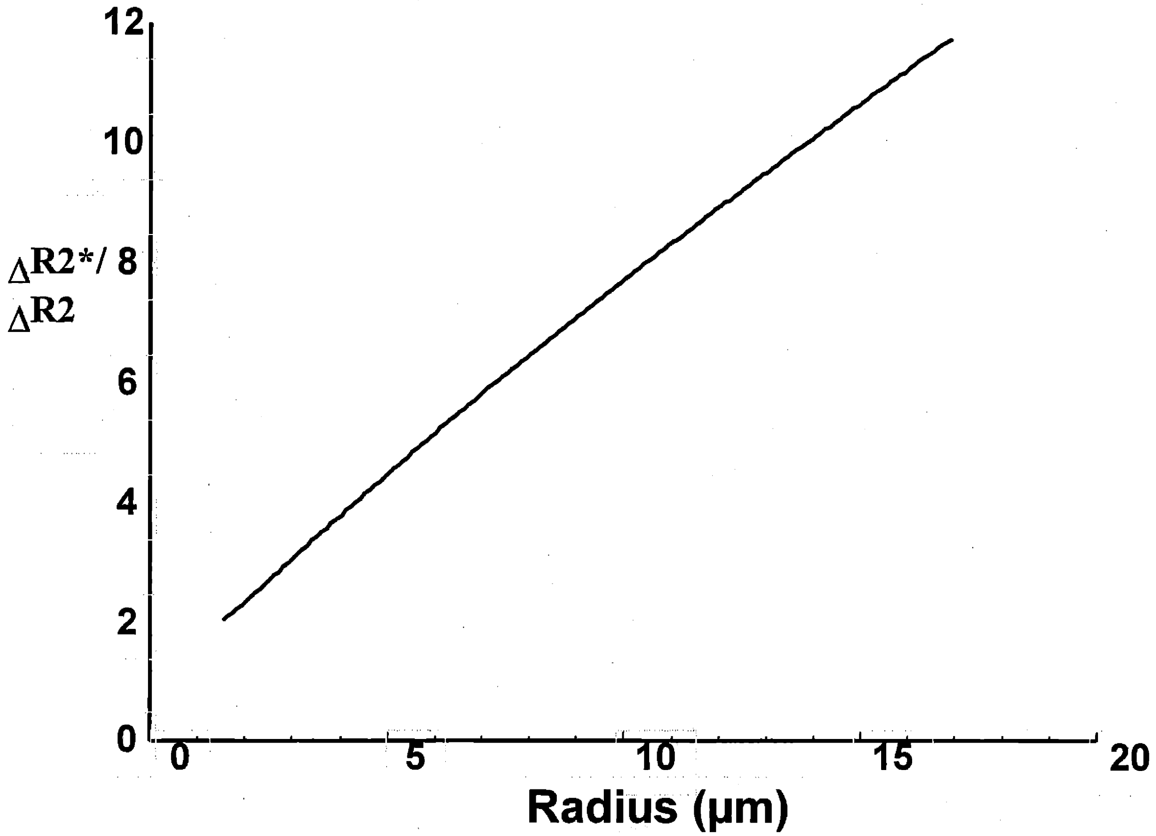

Figure 2 Ratio of gradient to spin echo relaxavity is linear with magnetic perturber radius. This finding is the basis for the mean vessel size metric.

Mean Vessel Size

Examination of the size dependencies of ΔR2* and ΔR2 on perturber size in cylindrical systems leads to useful a discovery. The ratio ΔR2*/ΔR2 varies linearly with cylinder radius (Figure 2). This result comes directly from the Monte Carlo simulations. This theoretical finding was important for two separate reasons. First, the ability to perform in vivo non-invasive assays of blood vessel size would be very useful in cancer as well as potentially in other disease systems such as stroke. Second, it would be an instance where the inferred information obtained from the study would reflect object parameters orders of magnitude smaller than the conventionally defined resolution of the images. Such superfine resolution is an important discovery and is testament to the flexibility and power of nuclear magnetic resonance. Dennie *et al.* followed this work in a C6 brain tumor model in rats (Dennie, Mandeville et al. 1998). It is one of the goals of this thesis to further explore this technique and most importantly to validate it directly with conventional histological analysis.

Advantages of intravascular contrast agents

The increasing use of CBV in research settings testifies to the fact that it is a superior tumor marker than clinically-used gadolinium-DTPA. Gadolinium is a relatively small paramagnetic agent and provides contrast based on leakage. In most physiological applications, the rate of leakage is proportional to the permeability surface area product. The amount of contrast enhancement (i.e. the bright spot on a clinical MR film) is a complex amalgum of permeability, blood volume, extravascvascular space, quantity injected, and blood flow. It has been fortuitous that gadolinium-enhanced MRI has been enormously useful in the clinic despite its status as a relatively non-specific biomarker. Intravascular agents are a more natural and specific marker for tumor presence, as it directly measures the amount of vasculature, and it is well known that increased vasculature is necessary for the existence of tumors beyond a few cubic mms (Folkman 1971). Specific CBV correlations with clinical parameters will be discussed in the next section. The anticipated arrival of FDA-approved contrast agents of this class will be a major improvement to radiological evaluation in oncology and in other blood vessel critical disease states like stroke.

The role of blood volume mapping in the longitudinal tracking of animal and human disease will likely evolve into a major one. Not only will radiologists and oncologists be able to track the size of tumors in the face of conventional therapy, but they will also have a near-ideal biomarker for the efficacy of anti-angiogenic therapy. Suitable clinical endpoints are difficult to quantify in a therapy designed mostly for tumor stasis rather than tumor cell kill. CBV measurement by MRI using intravascular contrast agents offers a direct marker of the vasculature, the precise target of anti-angiogenic therapies.

Bolus Methods

Theory

The ability to determine cerebral blood flow is critical for a complete *in vivo* picture of perfusion. As technology allows for faster MR imaging, it has become possible to track the motion of blood, or a contrast agent administered intravenously, with a time resolution on the order of the vascular mean transit time. By carefully injecting and rapidly monitoring contrast agents, it is now feasible to extract cerebral flow data without disturbing the vasculature and to perform such a measurement in a voxel-wise manner throughout the brain. To fully understand this MR technique is important to review some seminal tracer theory and to see how it is applied in this instance.

A delta-function bolus of tracer (contrast agent in our case) is injected and travels to some tissue voxel of interest (VOI). There will be a continuum of paths from the injection site to the VOI as well as a continuum of paths through the VOI . Eventually the tracer exits this VOI, leaving no residue. The paths through the VOI will depend on flow and the local vascular structure. The transport function *h(t)* is the probability density function describing these transit times and ranges from zero, indicating instantaneous flow, to infinity, describing regions where flow is absent or completely circuitous within the VOI. The arterial input *Ca(t)* feeds the VOI and the venous output function *Cv(t)* is given by

$$C_v(t) = C_a(t) \otimes h(t) \equiv \int_0^t C_a(\tau) h(t-\tau) d\tau$$

Equation 17

Mean Transit Time for tracer is defined with respect to the transport function:

$$MTT = \frac{\int_{-\infty}^{\infty} \tau h(\tau) d\tau}{\int_{-\infty}^{\infty} h(\tau) d\tau}$$

Equation 18

Weisskoff et al have described the distinction between this definition of MTT and the first moment of the *C(t)* curve as measured by MR during intravascular contrast agent bolus passage.

The amount of intravascular tracer in a VOI is determined by:

$$CBV = \frac{\int C_{VOI}(\tau)d\tau}{\int_{-\infty}^{\infty} C_a(\tau)d\tau}$$

Equation 19

In the setting of the brain, and assuming that the tracer is held intravascular by the blood brain barrier, the contrast agent occupies the intravascular, extracellular space not held by impermeable red blood cells – the plasma volume. The total space available is then CBV * (1-Hct), where Hct is the hematocrit. Under most conditions one may assume that Hct is constant and that comparisons may be made across regions and across animals.

Now, having defined MTT and CBV, we invoke the central volume theorem and state that they are related in the following way:

$$MTT = \frac{CBV}{CBF}$$

Equation 20

In our bolus passage experiments, the concentration *C(t)* is measured for each voxel as is an arterial input function (AIF). The most useful quantity from these experiments is the fraction of tracer remaining in the vasculature at some time *t*, called the residue *R(t)*:

$$R(t) \equiv 1 - \int_0^t h(\tau)d\tau$$

Equation 21

This function is appropriately normalized with $R(t=0) = 1$, with R(t) approaching or reaching 0 as time is extended to infinity. *R(t)* is a positive monotonic, decreasing function. We may now rewrite the concentration within a voxel $C_{VOI}(t)$ as a function of time utilizing the residue function:

$$C_{VOI}(t) = CBF \int_0^t C_a(t) R(t-\tau) d\tau$$

Equation 22

Should the arterial input function exist as a perfect delta-function, we simplify the integral and find that the initial height of the deconvolved concentration curve equals the flow. The first-order estimate of flow then is the peak increase in *C(t)*, which in the case of iron oxide contrast agents, is the peak drop in signal. This situation is analogous to the measurement of CBF invasively using radioactive tracers, or to a venous washout method. In reality, the arterial input function has a non-trivial time dependence. In practice, the bolus is injected as quickly and sharply as possible. Nonetheless, the deconvolution with the AIF is required. Ideally the measured AIF would match exactly the input felt by the VOI. In truth incongruity between the measured AIF and true AIF for each voxel is unavoidable and result in an artificially spread *R(t)* and consequently, dip in CBF. The AIF must be measured as closely as possible to the VOI of interest to minimize dispersion of the *R(t)* function.

From the curve of *R(t)* the next task is to solve Equation 22 for CBF.

Mathematical extraction of CBF

It is not straightforward to solve Equation 22 for CBF because we do not have much information about how *R(t)* varies with the local vascular network. An inverse solution is required, in which CBF for each voxel is solved either numerically or analytically. There are two main categories of approaches in this instance. One may invoke model dependent solutions, making certain assumptions about the nature of the vasculature and therefore *R(t)*. The other option is model independent; no knowledge is assumed about *R(t)* and CBF and *R(t)* are solved simultaneously.

Analytical (Model dependent) solutions

Model dependent solutions offer significant advantages in certain situations. If the system is well understood, it is the simplest and most mathematically stable method to perform the deconvolution. One such general model of the residue function is a single exponential that describes the residue based on MTT as follows:

$$R(t,MTT)=e^{-\frac{t}{MTT}}$$

Equation 23

In addition to this simplified model of one well-mixed compartment, one can also use more advanced models, often superpositions of exponentials, each corresponding to a separate compartment. The greatest drawback of these types of models is that they make unrealistic assumptions of the nature of the vascular bed. Generally, and particularly in tumor models which characteristically have highly chaotic vasculature, such simplifications are incorrect. While multi-compartment models can conceivably provide a reasonably accurate approximation of true vasculature, advanced models become exceedingly difficult to solve. This fact has encouraged the development of model independent approaches.

Nonparametric (Model independent) solutions

Ideally, dynamic measurements of physiology would be independent of the specific characteristics of that system. Minimizing the assumptions of the vascular system under study would allow for a more robust measurement. In non-parametric approaches, the residue function *R(t)* leads to CBF. These equations are difficult to solve if SNR is not high. Noise is a major problem, and can lead to instabilities in the equations and errors in the solutions.

Non-parametric deconvolution can be accomplished using a variety of mathematical transforms or through algebraic means. Numerous filtered transform methods have been described. It has been found however, by Ostergaard *et al.*(Ostergaard, Weisskoff et al. 1996), that algebraic methods tend to be more reliable. Singular Value Decomposition (SVD) solves the matrix version of

$$C(t_j)=\int_0^{t_j}C_a(\tau)R(t-\tau)d\tau\approx\Delta t\sum_{i=0}^{j}C_a(t_i)R(t_j-t_i)$$

Equation 24

SVD constructs matrices that permit the solution of *R(t)*. Given a complete time course, it is possible to identify elements in the *C(t)* curve that provide a stable solution to *R(t)* relative to the noise in the data. It has been shown that this technique leads to the best possible solution with respect to a least squares analysis (see Press *et al.* for another computations text).

Technical Considerations

There are many important practical considerations that must be addressed in order to successfully utilize the preceding theoretical constructs and translate them into quality maps of CBV and CBF. The first and most obvious issue is that of signal to noise. The images from which CBV and CBF are calculated must have adequate SNR, whether the calculation is being made in the steady state or dynamically through bolus tracking. This condition is more easily achieved in the steady state, as these images are generally time averaged resulting in a $\sqrt{(N)}$ increase in SNR, where N is the number of images. High SNR is more of a challenge in dynamic measurements where the convenience of time averaging in not feasible. In these cases, a balance must be struck between time resolution and SNR. Ideally, images would be acquired very rapidly to allow for the greatest time resolution. However, this generally means using a sub-optimal T_R and small flip angle. In the extreme case of very fast imaging, the MR signal and hence the image quality suffers.

In this work, the balance was struck such that there were several time points acquired during the first pass of the contrast agent bolus such that the Mean Transit Time could be sampled adequately. In rats, MTT $\approx$ 1.25 seconds in normal brain, and roughly 30% higher in tumor. Time sampling of four times per second yielded satisfactory images and permitted analysis of the bolus time course as long as the bolus was delivered sharply. Ideally, one would deliver the contrast agent as a delta-function bolus. In reality, the experimenter is constrained by the gauge and compliance of the venous line as well as the natural resistance of the cannulated vessel. The sharpness of this injection is further broadened by vascular transit from the injection site to the brain. In this work, we utilized a central line to inject the agent directly into the right atrium so as to minimize the widening due to vascular transit. The physical injection was carried out as quickly as possible.

After minimizing the shape of the bolus, we then select an arterial input function (AIF) with which to perform the deconvolution. Ideally, this should come from the time course of purely arterial voxels. Others have approximately the AIF using venous data from the great draining vessels on the surface of the brain such as the superior sagittal sinus. Some have even mathematically modeled an artificial AIF based on literature data, particularly when no arterial information is available. We selected our MR image coverage to include the middle cerebral arteries bilaterally. We used these voxels (typically eight) to represent the arterial input function. While there is certainly some partial volume averaging with neighboring brain tissue, this is a good approximation in this small animal model. In human studies finding an arterial input is easier, as is obtaining adequate time resolution because of the greater MTT in humans.

One final technical issue is that of contrast agent leakage. The CBV and MVS calculations are based on an intravascular tracer. As discussed earlier, our agent has been shown to have a blood half-life of about four hours, much larger than the time frame of the experiments. What little change in blood concentration occurs would serve to underestimate blood volume as a decrease in the contrast agent would result in a decrease in susceptibility difference between vessel and tissue, and therefore an underestimate in the signal change and blood volume.

Gadolinium Methods

Gadolinium

Contrast agents have been constructed to exploit the properties of paramagnetism to increase contrast in certain situations. Such agents have large magnetic moments due to their unpaired electrons, which can generate local magnetic fields more than 10^3 times greater than those generated simply by protons. Gadolinium diethylenetriamine pentaacetic acid, known as Gd-DTPA, is one such contrast agent. It is the most commonly used MR contrast agent and has been shown to be both safe and effective in many situations. Gd-DTPA is effective because it has seven unpaired electrons. These unpaired electrons interact with the proton magnetic dipole in a dipole-dipole or electron-dipole interaction, which has the effect of shortening T_1, the longitudinal relaxation time. Ideally, this compound would only affect T_1, but in reality, motion of these paramagnetic ions induces a chaotic local magnetic field inhomogeneity that cannot be refocused, which enhances proton dephasing and results in T_2 and T_2* decreases.

Weisskoff et al have shown that the absolute susceptibility of Gd-DTPA in a vessel and the surrounding tissue is 2.8 x 10^{-8} mM-1 Gd (cgs). Gadolinium has many important uses, particularly in the brain. It has been shown to increase both the specificity and sensitivity of brain MR imaging. In the case of intact BBB, Gd-DTPA cannot extravasate into the extracellular space, and there is no change in signal. It does not generally cross intact cell membranes due to the size charge and hydrophilic nature of the molecule. In cases of BBB breakdown such as tumor angiogenesis, the agent does indeed leak into this compartment. The resulting local increase in signal in these areas is termed enhancement. Qualitatively, one can use gadolinium enhancement to identify areas of tumor. There has been much work with the time course of gadolinium enhancement in an effort to extract more and quantitative information from gadolinium injections.

Permeability Mapping Background

Tofts and Kermode developed methods to quantitatively analyze the characteristics of signal enhancement due to gadolinium extravasation (Tofts and Kermode 1991). They introduce a dynamic scanning approach by which signal enhancement versus time curves are generated such that lesions that enhance with different time courses can be differentiated. They then describe a quantitative analysis of the dynamic enhancement curve that permits absolute measurements of blood brain barrier permeability and leakage space.

Modelling Permeability

Tofts and Kermode first presented their model for the dynamic enhancement of MR signal following injection of Gadolinium chelates in 1991, similar to the model of Larsson et al. (Larsson, Stubgaard et al. 1990; Tofts and Kermode 1991). Since then, many have utilized this or very similar strategies for evaluating permeability related metrics in animals and humans. The basic process involves repeated imaging of tissue following the injection of a T1 based contrast agent (typically Gado-DTPA). The agents must be diffusible (transportable out of the capillaries into the extravascular extracellular space). The image data set includes baseline values and images defining the wash-out and/or the wash-in of the contrast agent. Signal intensity versus time curves from a single voxel or region of interest can permit study of physiological variables such as capillary leakage.

We evaluated the DCE-MRI data building upon the two compartment physiologic model of Tofts and Kermode (Tofts and Kermode 1991; Tofts, Brix et al. 1999)

$$\frac{dCt(t)}{dt} = k^{trans}Cp(t) - k_{ep}Ct(t)$$

Equation 25

where C_t and C_p are tissue and plasma contrast agent concentration, and k^{trans} and k_{ep} are transport rates into and out from the extracellular extravascular space. We integrated the generalized kinetic model (Equation 25) over time

$$Ct(t) = k^{trans}\int_0^t Cp(t)dt' - k_{ep}\int_0^t Ct(t)dt'$$

Equation 26

Based on the work of van der Sanden and colleagues (van der Sanden, Rozijn et al. 2000), we assumed a functional form of the vascular input forcing function Cp(t)

$$Cp(t) = \xi\left[A_1e^{-\lambda_1 t} + A_2e^{-\lambda_2 t}\right]$$

Equation 27

Where A_1 and A_2 are amplitudes (mM) and λ_1 and λ_2 represent bi-exponential plasma decay of gadolinium due to exchange with the extravascular extracellular space and its renal clearance, respectively (Tofts and Kermode 1991). We calculated a fitting factor ξ related to the total constant agent dose in each rat by summing the signal drop due to the first pass T2* effect of gadolinium over eight seconds (2 images) in normal brain contralateral to the tumor. We then fit the full signal time course data (excluding 24 seconds of data after contrast injection because of T2* effects) to the linear equation (EQN 2) for k^{trans} and k_{ep}. Image voxels with less than 10% increase in signal were excluded.

In the permeability-limited regime ($PS < F$), $k_{ep} = PS\ \rho/v_e$ where PS is the permeability-surface area of the endothelial cells, F is blood flow, ρ is the tissue density, and v_e is the volume of extravascular extracellular space per unit volume of tissue (Tofts, Brix et al. 1999). Based on literature values for normal rat cerebral blood flow (100 ml/min/100g tissue) (Todd, Weeks et al. 1993; Wittlich, Kohno et al. 1995) and ve (0.27) (van der Sanden, Rozijn et al. 2000), PS in these leaky tumors is still two orders of magnitude less than CBF. The k_{ep} data then provide a quantitative measure of the permeability surface area product, ρ/v_e taken as invariant pre- and post-therapy.

Aronen, H. J., J. Glass, et al. (1995). "Echo-planar MRI cerebral blood volume mapping of gliomas: Clinical utility." Acta Radiol **36**: 520-528.

Boxerman, J. L. (1994). Non-invasive Measurement of Physiology Using Dynamic Susceptibility Contrast NMR Imaging. Health Sciences and Technology. Cambridge, Harvard-MIT.

Boxerman, J. L., P. A. Bandettini, et al. (1995). "The intravascular contribution to fMRI signal change: Monte Carlo modeling and diffusion-weighted studies in vivo." Magn Reson Med **34**(1): 4-10.

Boxerman, J. L., L. M. Hamberg, et al. (1995). "MR contrast due to intravascular magnetic susceptibility perturbations." Magn. Reson. Med. **1995**: 555-566.

Brown, M. F., A. A. Ribeiro, et al. (1983). "New view of lipid bilayer dynamics from 2H and 13C NMR relaxation time measurements." Proc Natl Acad Sci U S A **80**(14): 4325-9.

Carr, H. and E. Purcell (1954). "Effects of diffusion on free precession in nuclear magnetic resonance experiments." Phys. Rev. **94**(3): 630-638.

Dennie, J., J. B. Mandeville, et al. (1998). "NMR imaging of changes in vascular morphology due to tumor angiogenesis." Magn Reson Med **40**(6): 793-9.

Folkman, J. (1971). "Tumor angiogenesis: therapeutic implications." N Engl J Med **285**(21): 1182-6.

Gillis, P. and S. H. Koenig (1987). "Transverse relaxation of solvent protons induced by magnetized spheres: application to ferritin, erythrocytes, and magnetite." Magn Reson Med **5**(4): 323-45.

Glasel, J. A. (1970). "NMR relaxation in heterogeneous systems." Nature **227**(259): 704-5.

Larsson, H., M. Stubgaard, et al. (1990). "Quantitation of blood-brain barrier defect by magnetic resonance imaging and gadolinium-DTPA in patients with multiple sclerosis and brain tumors." Magn. Reson. Med. **16**: 117-131.

Ostergaard, L., R. M. Weisskoff, et al. (1996). "High resolution measurement of cerebral blood flow using intravascular tracer bolus passages. Part I: Mathematical approach and statistical analysis." Magn Reson Med **36**(5): 715-25.

Rosen, B. R., J. W. Belliveau, et al. (1991). "Susceptibility contrast imaging of cerebral blood volume: human experience." Magn Reson Med **22**(2): 293-9; discussion 300-3.

Rosen, B. R., J. W. Belliveau, et al. (1991). "Contrast agents and cerebral hemodynamics." Magn Reson Med **19**(2): 285-92.

Shen, T., R. Weissleder, et al. (1993). "Monocrystalline iron oxide nanocompounds (MION): physicochemical properties." Magn Reson Med **29**(5): 599-604.

Todd, M. M., J. B. Weeks, et al. (1993). "Microwave fixation for the determination of cerebral blood volume in rats." J Cereb Blood Flow Metab **13**(2): 328-36.

Tofts, P. S., G. Brix, et al. (1999). "Estimating kinetic parameters from dynamic contrast-enhanced T(1)-weighted MRI of a diffusable tracer: standardized quantities and symbols." J Magn Reson Imaging **10**(3): 223-32.

Tofts, P. S. and A. G. Kermode (1991). "Measurement of the blood-brain barrier permeability and leakage space using dynamic MR imaging. 1. Fundamental concepts." Magn Reson Med **17**(2): 357-67.

Torrey, H. (1956). "Bloch equations with diffusion terms." Phys. Rev. **194**(3): 563-565.

van der Sanden, B. P., T. H. Rozijn, et al. (2000). "Noninvasive assessment of the functional neovasculature in 9L-glioma growing in rat brain by dynamic 1H magnetic resonance imaging of gadolinium uptake." J Cereb Blood Flow Metab **20**(5): 861-70.

Weisskoff, R., J. Boxerman, et al. (1994). Simultaneous blood volume and permeability mapping using a single Gd-based contrast injection. Second Meeting of the Society of Magnetic Resonance, San Francisco.

Weisskoff, R. M., C. S. Zuo, et al. (1994). "Microscopic susceptibility variation and transverse relaxation: theory and experiment." Magn Reson Med **31**(6): 601-10.

Weissleder, R., D. D. Stark, et al. (1989). "Superparamagnetic iron oxide: pharmacokinetics and toxicity." AJR Am J Roentgenol **152**(1): 167-73.

Wittlich, F., K. Kohno, et al. (1995). "Quantitative measurement of regional blood flow with gadolinium diethylenetriaminepentaacetate bolus track NMR imaging in cerebral infarcts in rats: validation with the iodo[14C]antipyrine technique." Proc Natl Acad Sci U S A **92**(6): 1846-50.

Chapter 5 Tumor Vessel Morphometry and Physiology Relationships

Introduction

In this thesis, we take three approaches to refine non-invasive imaging techniques to elucidate the physiology of tumor vessels. In the next two chapters, we will evaluate reactivity to physiological perturbation and permeability, respectively. This chapter discusses the application of both steady state and dynamic contrast enhanced MR imaging methods to interrogate the vasculature of human gliomas in rat models. Utilizing these techniques we study tumor vessels with respect to normal vessels along two lines: morphometry and physiology. We study tumor vessel morphometry by evaluating total and microvascular cerebral blood volume (CBV) as well as mean vessel size (MVS). Our physiological measurement is the determination of the flow/volume relationship within tumors quantified by our definition of a metric of perfusion efficiency.

Better understanding of tumor vasculature microanatomy is crucial to the understanding of tumor growth dynamics and angiogenesis and provides a basis from which to evaluate anti-cancer therapies, particularly vascular targeting therapies. Currently, no one technique can provide detailed vascular information without extensive invasive probing. We exploit a novel macromolecular iron oxide compound to solve this problem. While still in clinical trials, this class of contrast agent will soon be available in clinical practice. With respect to vascular measurements, MRI offers three key advantages over other methods. First, the MRI measurement is non-invasive compared to other existing techniques. Research animals need not be sacrificed following imaging in the laboratory, and clinically, patients may undergo scans as often as is desired. Second, the MR imaging parameters can be set, based on magnetic susceptibility contrast physics, primarily sensitive to the microvasculature. By utilizing previous findings regarding the magnetic susceptibility mismatch between contrast agent containing capillaries and free extravascular space, we selectively refocus signal in the smallest vessels (Dennie, Mandeville et al. 1998)(Boxerman, Hamberg et al. 1995)(Fisel, Ackerman et al. 1991). Finally, these imaging methods permit interrogation of the entire tumor rather than a sample limited by biopsy. Previous methods of determining mean vessel size involve the staining and microscopic counting of excised tissue samples (Mignot, Barres et al. 1981). Such work is time consuming and prone to sampling error. Even if sampling criteria are satisfied, the tissue specimen may be from an unrepresentative or non-critical part of the tumor (de Jong, van Diest et al. 1995). We solve this problem by sampling the whole tumor.

We predict that MR-measured blood volume will correlate highly with vascular area measured in excised and stained tissue samples of tumor and normal brain. CBV is known to be a surrogate tumor marker and a prognostic indicator. Aronen et al. investigated the relationship between CBV and tumor grade in human gliomas (Aronen, Gazit et al. 1994). Several groups have shown that tumors present with high blood volume by MRI (Rosen, Belliveau et al. 1991) (Aronen, Glass et al. 1995) and PET (Mineura, Yasuda et al. 1986). High tumor CBV is caused by the presence of new vessels developed by the process of tumor angiogenesis. In Folkman's archetypal picture of tumor growth, expansion is modest at first, limited to roughly 1mm^3 (Folkman 1971). Following the proposed "angiogenic switch," the generation of new vessels begins (Folkman and Hanahan 1991) (Folkman 1992). As these new vessels result in greater vascular area, and given, as we show in this chapter, that CBV is intimately linked with vascular area, we then conclude that high CBV is a footprint of tumor angiogenesis. Knowing the gross amount of vasculature can be helpful, as it has been related to numerous clinically relevant parameters such as glucose uptake and tumor grade (Aronen, Pardo et al. 2000) (Aronen, Glass et al. 1995) (Mineura, Sasajima et al. 1994). Additionally exciting is the potential to focus primarily on the microvascular component of the blood volume, given that most tumor-spawned vessels are in the microvessel size regime. We suggest that microvascularly-weighted CBV may reflect the tumor vasculature even more accurately than total CBV.

We hypothesize that our MR MVS parameter $\Delta R2^*/\Delta R2$, the ratio of gradient to spin echo relaxivity, will correlate well with mean vessel size determined by standard histological techniques. The application of an intravascular contrast agent enables us to collect such data. Mean vessel size (MVS) is an intriguing parameter. Previous studies have shown that tumors tend to exhibit larger vessels than normal tissue (Dewhirst, Tso et al. 1989). But methods to stain, count, and size tumor vessels are so arduous as to be useless in the clinical setting. Rather, vascular area is the parameter of general use. Consequently, little is known regarding the clinical relationships between mean vessel size and parameters such as tumor grade and patient outcome because such studies are not feasible in the clinical setting. Our investigation of mean vessel size may not only reveal interesting facts about vessel size in tumors but may also introduce a technique of great future clinical utility.

Having looked at the locally static parameters of CBV and MVS, we also sought to understand the perfusion status of these tumors. Blood flow and volume are well matched in normal tissues. In tumors, there are three possibilities regarding this relationship. CBF and CBV could remain well matched, there could exist a power relationship between the two as is the case with Grubbs' law, or there could exist a flow/volume mismatch. Based on the inefficient and tortuous nature of tumor-spawned vessels, we hypothesized a mismatch of low flow per unit volume in tumors compared to normal brain. Following the method of Ostergaard et al., we track the passage of a bolus contrast agent and deconvolve it with the measured arterial input function. From this data we can extract a measure of total perfusion or local cerebral blood flow (CBF) with high spatial resolution (Ostergaard, Weisskoff et al. 1996). We define a parameter called perfusion efficiency by normalizing the total CBF by the amount of blood (CBV), and scaling this value to normal brain. By this calculation we quantitatively determine diminished perfusion efficiency, or flow-volume mismatch, in tumors. There is a great deal of academic and pharmaceutical interest in tumor perfusion, a subject that has ramifications in the fields of tumor biology, drug delivery, and oncology. For example, Jain et al. suggest that more streamlined vasculatures could be more accessible to blood born anti-cancer agents (Jain 2001).

We will begin with blood volume measurements, reflecting the total space of the tumor vessels. Then, we will employ MR physics to extract an indicator of mean vessel size. Finally, we will evaluate the flow/volume relationship in tumors with respect to normal brain tissue. Our ensemble of MR imaging biomarkers will permit us to explore the nature of the tumor's vascular bed in a more complete and non-invasive way and could potentially lead to useful clinical tools.

Methods

Glioma implantation

The U87MGdEGFR human glioblastoma cells were a generous gift of Dr. H.-J. Su Huang (University of California at San Diego). This cell line was established by retroviral transfer of a mutant epidermal growth factor receptor (de 2-7 EGFR) into U87MG human glioblastoma cell line, enhancing its tumorigenic capacity in the brain of nude mice (Nishikawa, Ji et al. 1994). Cells were grown in Dulbecco's modified Eagle medium (DMEM) supplemented with 10% fetal bovine serum, 100 U/ml penicillin, 100ug/ml streptomycin, and 50ug/ml G418 at 37°C in 5% CO_2.

Gli36dEGFR5 is a human malignant glioma cell line, stably transduced with a recombinant retrovirus expressing mutant epidermal growth factor receptor (de 2-7 EGFR) (Ichikawa and Chiocca, unpublished experiments). These cells were grown at 37 C in an atmosphere containing 5% CO_2 in Dulbecco's Modified Eagle Medium (DMEM) supplemented with 10% heat-inactivated fetal calf serum, 100U/ml of penicillin, 100 ug/ml of streptomycin, and 0.5 ug/ml of puromycin (SIGMA, Saint Louis, MO).

Animal Preparation

Animal studies were performed in accordance with guidelines issued by the Massachusetts General Hospital Subcommittee on Animal Care. Adult female nude rats (rnu/rnu) were anesthetized with an intraperitoneal injection of 0.5ml of 0.9% NaCl containing 12.5mg of ketamine and 2.5mg of xylazine. After immobilizing the rats in a stereotactic apparatus and placing a linear skin incision over the bregma, a 1mm burr hole was drilled in the skull approximately 1mm anterior and 2mm lateral to the bregma on the right side. 200,000 U87MGdEGFR cells (in a 2µl volume) were injected at a depth of 3.5mm from the dura, using a 5µl Hamilton syringe.

Animal Maintenance

Rats were anesthetized with 1.5% halothane in oxygen for surgery; a tracheostomy was performed, and femoral arterial and venous cannulae were inserted. Following surgery, rats were mechanically ventilated with 0.7% halothane in a mixture of air and oxygen using a 3 ml tidal volume, a rate of 40 breaths per min, and an inspiration to expiration ratio of 1:1. After initiation of mechanical ventilation, rats were paralyzed with a 2 mg/kg bolus of pancuronium followed by continuous intravenous infusion at 2 mg/kg/hr. To minimize motion artifact, rats were placed into a custom plastic cradle attached to a head frame machined from plastic (David Kopf Instruments, Fremont, CA); heads were fixed with plastic screws inserted into the ear canals and a bar inserted under the front incisors. The rat torso was wrapped in two heating blankets (Gaymar, Orchid Park, NY) that circulated water at 40° C to maintain body temperature. Rat heads were shaved and covered with gel toothpaste to reduce magnetic susceptibility artifacts arising from the air-tissue interface. The ear canals and oro-pharynx were also filled with toothpaste.

Imaging protocols

Between ten and thirteen days after implantation, n=15 rats underwent imaging on a 2T 11cm bore SISCO NMR image Spectrometer (Varian Associates, Fremont, CA) using a custom-built surface coil. Before contrast agent injection, baseline spin echo and gradient echo conventional (n=11) or echo planar (n=4) images were obtained via an interleaved double echo protocol adapted from the pre-existing multi-slice imaging pulse sequence code ($TR/TE_{GE}/TE_{SE}$ = 2500/22/60 ms, FOV 2.5 X 2.5 cm, slice thickness 1mm, in-plane resolution: 780 μm, n=60 averages). A total dose of 3 mg/kg of MION was then injected in three 1mg MION / kg animal boli; during which a GE EPI single slice bolus tracking protocol (TR/TE = 250/22 ms, FOV 2.5 X 2.5 cm, slice thickness 1mm, flip angle = 40) was used to sample the MR signal time course at a rate of four times per second.

Rat core temperature and mean arterial blood pressure (MABP) were monitored throughout the imaging session. Blood gas analysis yielding pH, and partial pressures of CO_2 and O_2 was carried out periodically via samples drawn from the femoral artery.

Histology

Animals were perfused during sacrifice by intracardiac infusion of a solution containing 4% neutral paraformaldehyde (PFA) in phosphate buffered saline (PBS) pH=7. Harvested brains were placed for 24 hours in 4% PFA in PBS and then for an additional 2 days in 30% sucrose in

PBS. Brains were analyzed by sectioning (10um thick) on a cryostat and air-dried at room temperature. Tumor sections were stained by hematoxylin and eosin or NBT/alkaline phosphatase to stain vessels specifically (Weiss, Buchweitz et al. 1982). Traditional blood vessel staining methods such as the application of CD31 or Factor VIII (von Willebrand Factor) failed to stain the tumor vasculature, although they did adequately color vessels on the contralateral side of the brain.

Regional Analyses

Regions of interest (ROI) were outlined in the MR images and histological sections of each rat to facilitate inter-animal comparisons of the imaging data. We used post-contrast agent T2*-weighted images to delineate the tumor, selecting the (obvious) dark region as tumor. We also defined an ROI corresponding roughly to the striatum-region contralateral to the tumor for comparison as normal tissue. Within the tumor region, the following specific subsections were defined geometrically, dividing the entire tumor into three ring-like regions from the center of the tumor outward: Tumor Center, Tumor Middle and Tumor Edge. Using these ROIs, we then normalized values of CBV and CBF to contralateral striatum to provide a common basis of comparison across animals. For comparison with histology, these ROIs were duplicated in the appropriate histological section.

After imaging, fixation and brain removal, 10 μm sections were sliced on a cryotome. Fixed brain sections corresponding to the MRI slices through the tumor, as determined by anatomical markers such as brain size, were then stained with NBT/BCIP, which stains the alkaline phosphatase of the blood vessels. Slides, each containing a brain section from a scanned rat, were placed under the digitizing microscope. Pictures of the tissues, magnified to 20x, were processed in the ImageProPlus software package. The program allowed us to identify, highlight, and measure the darker objects in the images. As the vascular stain was darker than the counterstain, we used semi-automated thresholding methods that selected objects in the field based on overall light intensity and its breakdown into its RGB components to select vessels. Then we gathered data from each object regarding its size and shape. The minimum radius from the center of each object to its edge was used as the indicator of vessel radius and the fractional stained area in a given field was used as the vascular area. Data was collected from the blood vessels in three different areas of the tumors (edge, middle, and center) and on the contralateral side.

Results

To determine the vascular properties of tumors, we imaged 15 rats inoculated intracranially with U87MGdEGFR, 6 of which underwent histological examination. Of the histologically examined rats, n = 4 underwent steady state EPI to permit direct voxel-wise matching with dynamically acquired data. An additional 4 rats were inoculated with GLI36dEGFR. All rats received three or four bolus injections of the intravascular macromolecular contrast agent MION to permit averaging of CBF measurements. Blood gas values of each rat were measured via arterial blood sampling. As metabolic parameters like $PaCO_2$ and MABP can profoundly influence blood flow and blood volume, reasonably consistent blood gas values of $PaCO_2$ and MABP were prerequisite for valid comparison of tumor CBF and CBV across rats. The physiological statuses of the rats at the time of imaging were: (Mean values ± SEM) $pH = 7.31 \pm 0.04$; $PaCO_2 = 36.4 \pm 1.2$; $PaO_2 = 171 \pm 4$; $MABP = 112 \pm 7$. Core temperature was maintained between 37.0° and 38.0° Celsius.

N = 6 rat brains were removed, fixed, sliced, and stained by the protocols listed above to permit comparison with MR images. We found that more traditional vascular stains (e.g. Factor VIII, CD31) were ineffective in the U87MGdEGFR tumor line but NBT/BCIP was successful. Figure 3 shows the vascular stain (dark) with eosin counterstain (light purple).

To ensure that the histological data correctly represented each region, it was necessary to measure vascular area and size from adequate number of blood vessels. Histology values from each ROI (corresponding to roughly 20 voxels) were compiled from four 20X microscopic fields, sampling about 800 microvessels for each data point. We expressed the mean vessel size as a function of the number of vessels counted (e.g. Figure 4). Values within 10% of the final value converge quickly – within 100 counts.

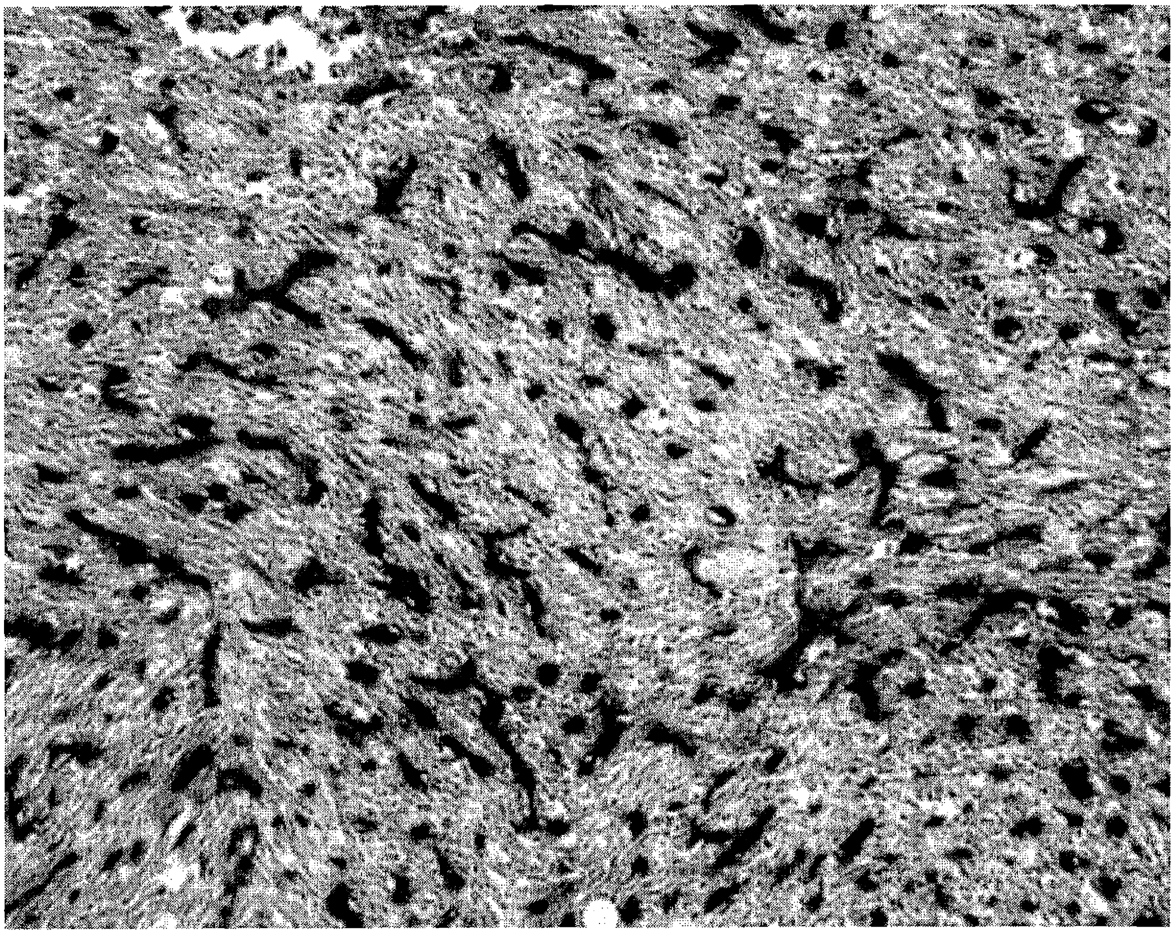

Figure 3 Vascular stain of U87MGdEGFR utilizing NBT/BCIP staining alkaline phosphatase (dark). Eosin counterstain (lavender).

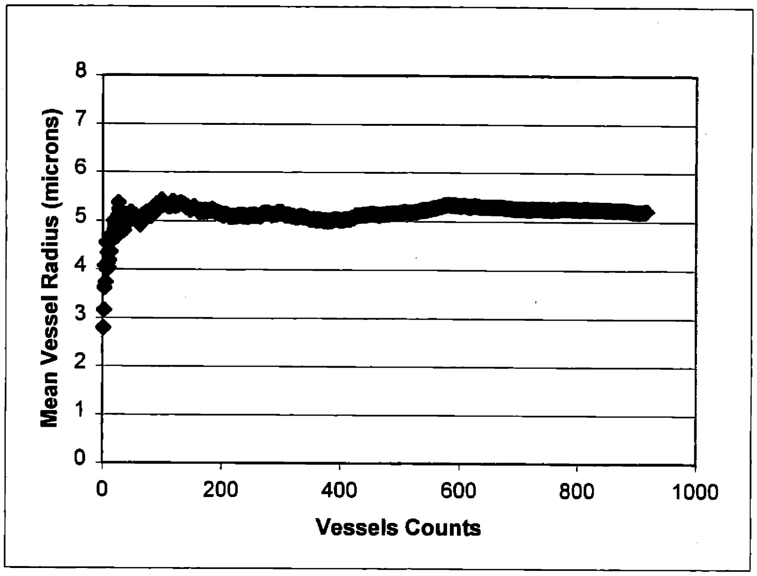

Figure 4 Convergence of mean vessel radius with number of vessels counted. By counting several hundred vessels, adequate sampling is ensured.

After confirming adequate sampling, we compiled vascular data from each region in each rat (Table 7). The mean vessel radius was greater in the tumor regions than in contralateral striatum ($p < 0.001$, pooled t-test). There was no significant difference in size between the tumor regions ($p > 0.1$, pooled t-test). Vessel area was five-fold greater in the tumor regions than in striatum ($p < 0.001$, pooled t-test) and again there was no difference between tumor regions ($p > 0.1$, pooled t-test). The tumor regions had greater vessel size variability than the contralateral striatum (standard deviation 1.7μm compared to 1.1μm) as well as greater vessel area variability (5.2% compared to 1.6%)

Having evaluated the histology data from six rats, we proceeded to analyze the MR data so that we could determine the relationships between them. From the steady state images before and after administration of contrast, we generated maps of $\Delta R2^*$ and $\Delta R2$, transverse nuclear relaxivity determined by gradient echoes and spin echoes, representing total and microvascularly-weighted relative CBV respectively. Figure 5a and Figure 5b show typical maps of total and microvascularly-weighted CBV utilizing this approach. Figure 5c are mean vessel size maps created by using the $\Delta R2^*/\Delta R2$ metric. In each set of maps, we display 8 1mm thick coronal slices through rat brain and U87MGdEGFR tumor arranged rostral to caudal with 780μm in-plane resolution. Bright voxels represent large values, indicating high CBV in the first two sets of images, and large mean vessel size in the last set.

Histology	Striatum	Tumor Center	Tumor Middle	Tumor Edge
Average Radius	1.9μm	3.3μm	3.4μm	3.3μm
Radius Standard Dev.	1.1μm	1.7μm	1.8μm	1.7μm
Average Vessel Area	2.5%	12.3%	12.0%	12.1%
Standard Dev. of Vessel Area	1.6%	4.9%	5.0%	5.5%

Table 7 Vessel Size Summary. Values taken from four regions within n=6 rats bearing U87MGdEGFR gliomas. Tumor regions had larger and more varied blood vessel size and area. Averages and standard deviations were calculated across animals.

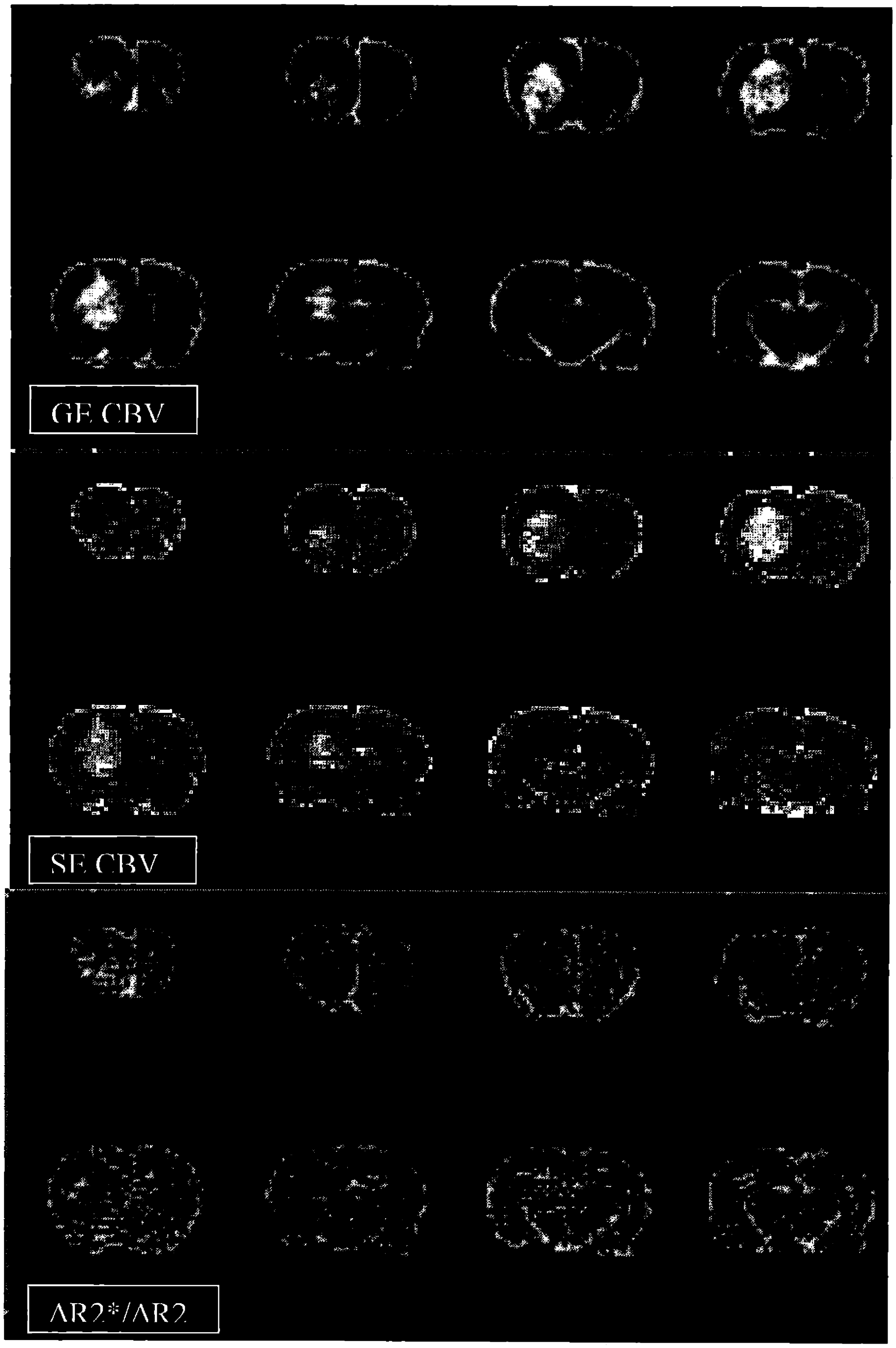

Figure 5 a) Total Blood Volume b) Microvascularly-weighted Blood Volume and c) Mean Vessel Size maps from U87dEGFR bearing athymic rats. Each set of maps contains the same 8 1mm thick slices with 780 micron in plane resolution.

These tumors exhibited elevated and heterogeneous total CBV (Table 8). We compiled values of total CBV from the same animals in which we performed histological analysis. The tumor margin is easily visible both by MR and by histology as the tumors are well-bounded rather than infiltrative. We found tumor total CBV highly elevated -- by 300% in the tumor center. There were not significant differences within the first two tumor ROIs, although the tumor edge ROI did have a lower CBV, but this is likely due to partial volume errors. Tumor CBV elevations measured by MRI (Table 8) underestimated the vascular area values determined by histology by 17%.

	Striatum	**Tumor Center**	**Tumor Middle**	**Tumor Edge**
GE CBV	**1.0 ± 0.0**	**4.0 ± 0.5**	**4.3 ± 0.5**	**2.8 ± 0.4**
SE CBV	**1.0 ± 0.0**	**3.7 ± 1.5**	**4.0 ± 1.2**	**2.3 ± 0.3**
Relative Histological Vascular Area	**1.0 ± 0.6**	**4.9 ± 2.0**	**4.8 ± 2.0**	**4.8 ± 2.2**
$\Delta R2^*/\Delta R2$	**4.7 ± 1.9**	**6.6 ± 1.4**	**5.4 ± 0.6**	**8.0 ± 2.9**
Relative Histological Vessel Radius	**3.8 ± 2.2**	**6.6 ± 3.4**	**6.8 ± 3.6**	**6.6 ± 3.4**

Table 8 MR data summary. Relative CBV and $\Delta R2^*/\Delta R2$ values were normalized to contralateral striatum to facilitate comparison across rats.

The voxel-wise distribution of CBV within a subset of $n = 4$ animals reveals a wide variation in values above that of normal tissue (Figure 6), but there is no overlap seen between the two regions. In tumor-based voxels, CBV ranged from 2-6 times that of normal brain blood volume.

Figure 7 shows the comparison between MR-derived tumor CBV voxels with the histology-derived number of microscopic fields with a given stained vascular area. In four animals, the relative MR CBV values were scaled by their mean value to correspond to the mean vascular area by histology to permit comparison between the absolute and relative techniques. The resulting data curves are strikingly similar, suggesting that MR CBV mirrors vascular area. Figure 8 shows the same comparison in contralateral striatum tissue. The curves are similar except for some underestimated high vascular areas.

We also explored the relationship between gradient echo CBV and spin echo CBV. Total and microvascularly-weighted blood volume from all n=15 rats are compiled in Table 9 along with the derived mean vessel size. While total CBV was elevated 240%, the microvascular blood volume was raised by 120%. The shaded rows indicate the rats in which we performed histological analysis.

Application of total and microvascularly-weighted CBV imaging to future clinical work relies on the validation of the technique with a gold standard. As vascular area is currently the only clinically accepted way to evaluate vascularity, we compared vascular area to microvascularly-weighted blood volume (Figure 9). The regression correlation between microvascularly-weighted CBV by MRI and histology is highly statistically significant ($r = 0.95$, $p = 1.7e-9$). The microvascularly-weighted CBV values recorded in this study extended over a six-fold range. Each data point represented a region of tumor or contralateral brain. Vascular area within striatum varied between 0.5% and 5% of the total histological area. In the U87 tumors, vascular area ranged between 7% and 22%, much higher than in striatum, agreeing with the known vascularity of tumors. Error bars in the y-axis represent the standard deviation of vascular area measurements. As the microvascularly-weighted CBV values were normalized to contralateral striatum to facilitate inter-animal comparison, striatum measurements of CBV are clustered at unity.

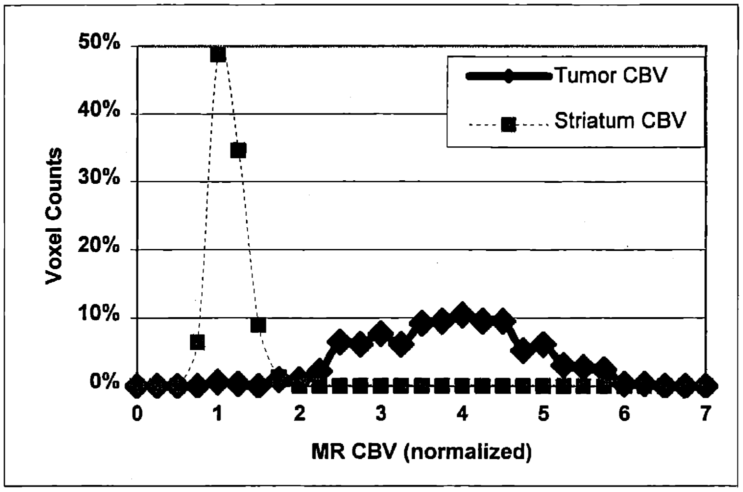

Figure 6 Total Cerebral Blood Volume distributions in tumor and striatum from n=4 rats. CBV is relatively uniform in the region of striatum. In tumor, there is highly elevated CBV. CBV distinguished tumor from striatum in these animals.

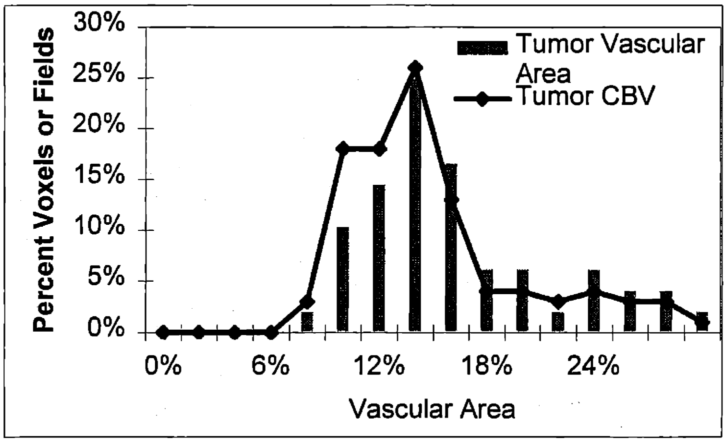

Figure 7 Comparison of MRI-based CBV measurements of tumor with vascular area determined by stained fractional area of microscopic fields. The histological data, culled from n = 4 rats, matches well with MRI values.

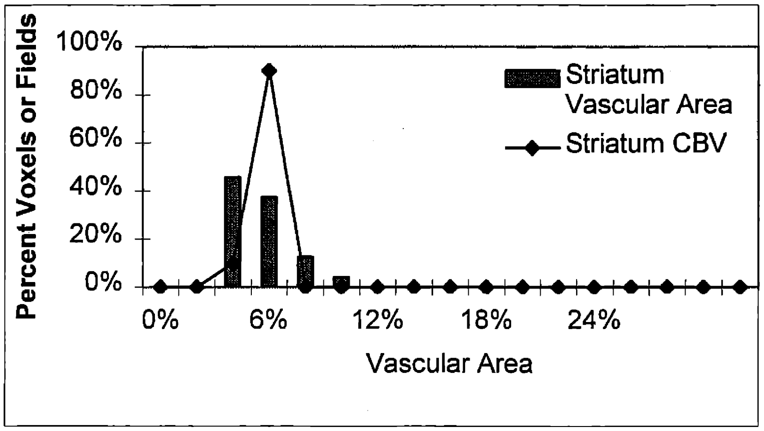

Figure 8 Comparison of MRI-based CBV measurements of striatum with vascular area determined by stained fractional area per microscopic high powered field of view of histological samples. The histological data culled from four animals matches well with MRI values.

Rat	GE CBV	SE CBV	ΔR2*/ΔR2
04/20/99	4.3	2.4	1.8
04/21/99	4.8	3.0	1.6
05/04/99	2.3	1.7	1.3
06/15a/99	3.5	2.5	1.4
06/15b/99	3.6	2.3	1.5
07/27/99	2.9	2.0	1.4
8/3a/1999	2.4	1.8	1.4
8/3b/1999	2.5	1.6	1.6
08/10/99	3.7	2.0	1.9
09/28/99	3.9	2.7	1.5
10/05/99a	2.6	1.5	1.7
6/28/00	3.8	3.0	1.3
02/07/01a	3.4	3.2	1.0
02/07/01b	3.5	3.0	1.6
02/07/01c	3.4	3.1	1.0
MEAN	3.4	2.4	1.5
ST. DEV.	0.7	0.6	0.3

Table 9 Summary of Total and Microvascularly-weighted relative blood volume results for N=15 U87MGdEGFR as well as the subsequently derived Mean Vessel Size metric. GE CBV elevated by 240%, SE CBV elevated by 140%. Average vessel size was elevated by 50%. Shading indicates animals on which histology was performed.

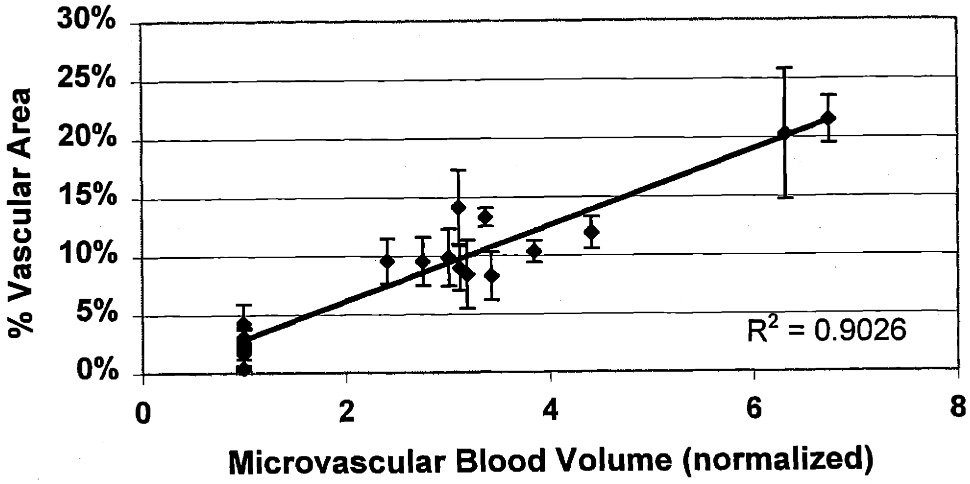

Figure 9 Microvascular Blood Volume by MRI, normalized to striatum, compared to histologically determined percent vascular area. The correlation between microvascular CBV by MRI and histology is statistically significant ($r = 0.95$, $p = 1.7 \times 10^{-9}$).

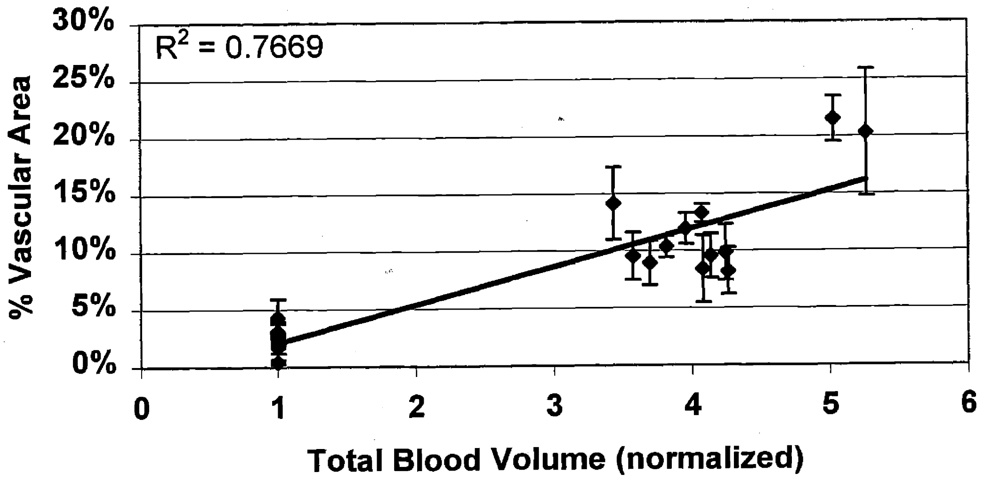

Figure 10 Total Blood Volume by MRI, normalized to striatum compared to histologically determined percent vascular area. The correlation between total blood volume and percent vascular area was statistically significant ($r = 0.88$, $p = 1.9$ e-6)

Next, we performed a similar analysis, this time plotting MR-measured total CBV and vascular area. Total blood volume also correlated significantly with the vascular density (r = 0.88, p = 1.9e-6). The level of correlation was higher between microvascular blood volume and histology than it was between total blood volume and histology (Figure 10). Error bars in the y-axis represent the standard deviation of vascular area measurements. That both blood volume measurements formed statistically significant correlations with vascular density verifies the accuracy of these techniques. It is not surprising that the microvascularly-weighted measure would correlate slightly better given that we were looking at brain regions with very few large (<20μm) vessels. Both agreed very well due to the domination of capillaries in these tissues. It is likely that in the periphery of the brain with the large draining veins, histological correlation with total CBV would surpass that of its correlation with microvascular CBV. The main obstacle to such an analysis is partial volume artifacts with extradural space.

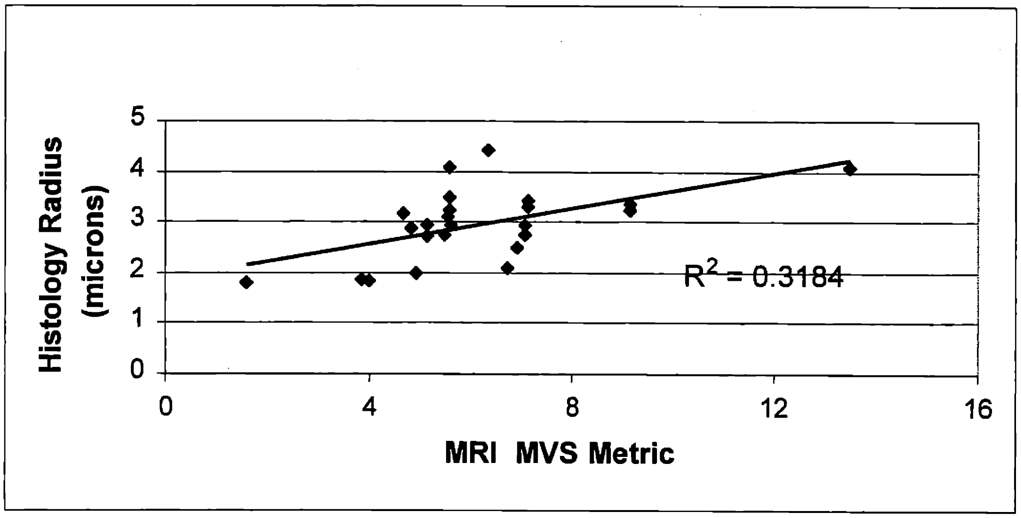

Figure 11 Mean vessel size by MRI and histology. Statistically significant correlation (r = 0.56, p = 0.004) linking the MRI based metric ΔR2*/ΔR2 (MVS) with the histology gold standard. With this relationship, one can estimate the average microvessel size within an MRI voxel – a non-invasive biopsy of sorts.

One of the main goals of this work is the exploration of the association between histologically determined mean vessel size (MVS) and our MRI MVS parameter, ΔR2*/ΔR2. We found a statistically significant correlation between the MRI MVS and mean vessel size as determined from tissue staining ($r = 0.56$, $p = 0.004$). A summary of histology-determined MVS values is included in Table 7, while the MRI-determined values are in Table 8. While previous work did indirectly approach the MR-histology relationship using one histological measurement of average vessel size as an input for microvascular computer simulations of MR signal (Dennie, Mandeville et al. 1998), we directly compared multiple specific tumor and normal brain regions by MR and histology, measuring a scaling factor between $\Delta R2^*/\Delta R2$ and mean vessel size for this tumor line.

Figure 12 and Figure 13 show histology and MR values from tumor and contralateral striatum, respectively. In the striatum, we see a relatively narrow distribution of vessel sizes, measured either by MR or histological vascular area. Tumor had a wider range by both methods. MR values were scaled by the relationship in Figure 11 for direct comparison.

The distribution of $\Delta R2^*/\Delta R2$ related to vessel size is presented in Figure 14. While tumor mean vessel size is somewhat larger than that of striatum, we see in this subset of $n = 4$ animals that there is high variability in both regions. There is a high degree of overlap between the two distributions of MR voxels.

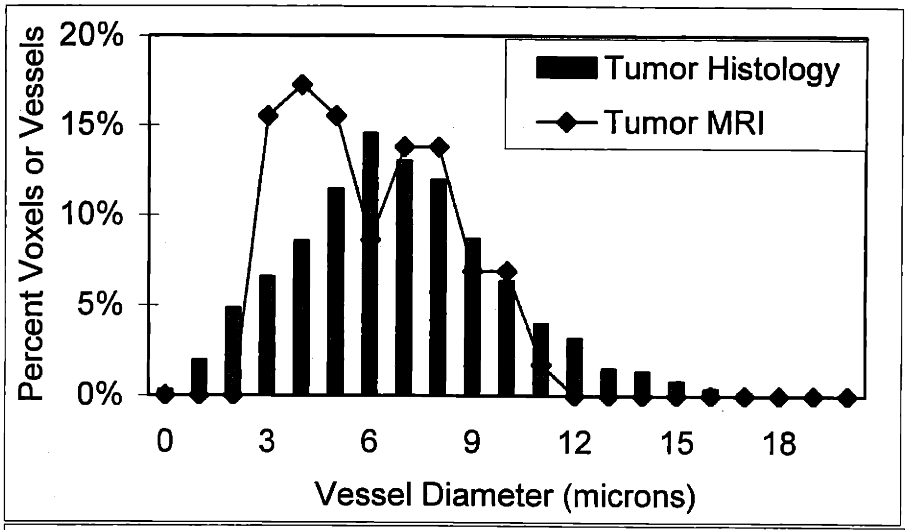

Figure 12 Comparison of MR-based and histological measurements of mean vessel size in tumor in one rat.

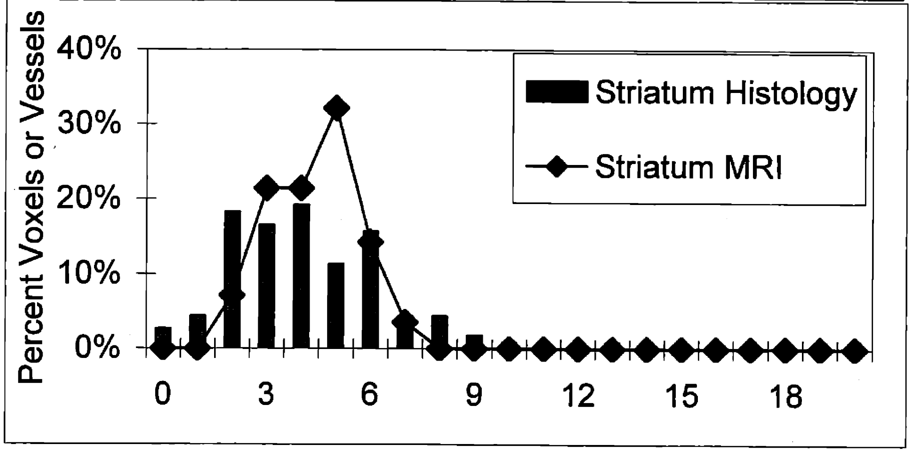

Figure 13 MRI vs. Histology in striatum of one rat. Number of high power fields of stained samples compared to number of voxels by MRI.

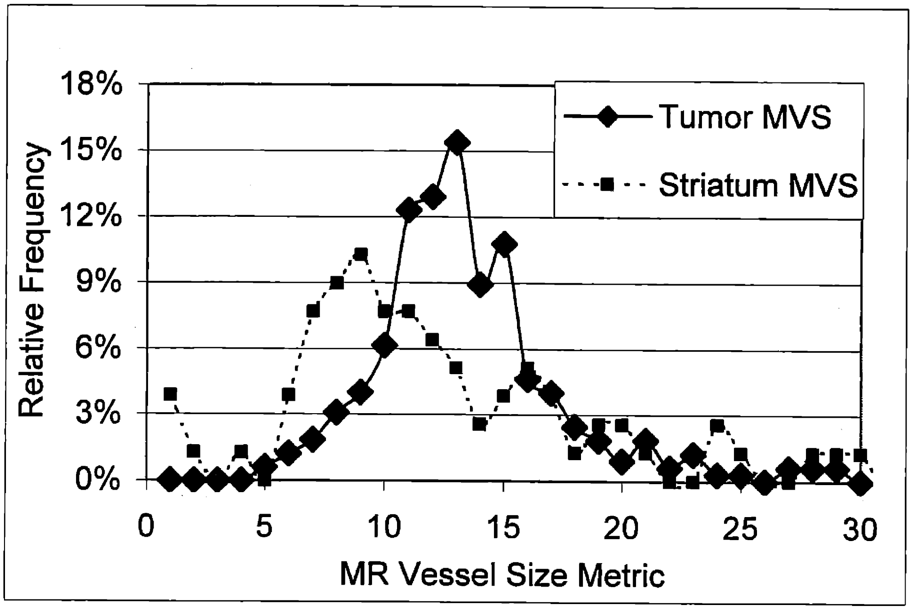

Figure 14 Mean vessel size as measured by MRI in tumor and striatum (n=4). Both regions are notable for high variability.

Rat CBF	Striatum	Tumor Center	Tumor Middle	Tumor Edge
05/04/99	1.0	2.9	2.5	1.7
06/15b/99	1.0	3.1	2.9	1.7
07/27/99	1.0	2.3	2.3	1.5
8/3a/1999	1.0	1.2	1.1	0.9
8/3b/1999	1.0	2.8	2.6	2.0
08/10/99	1.0	3.2	2.4	1.6
09/28/99	1.0	3.1	2.8	1.9
02/07a/01	1.0	2.5	2.3	1.2
02/07b/01	1.0	1.7	1.7	1.2
02/07c/01	1.0	2.1	1.9	1.0
MEAN	**1.0**	**2.3**	**2.1**	**1.4**
STD	**0.1**	**0.3**	**0.4**	**0.4**

Table 10 Cerebral Blood Flow. Relative blood flow values were normalized to contralateral striatum for comparison across animals. Tumor Center and Middle possess 120% elevated CBF in the U87MGdEGFR model. While the variance across animals was rather small, CBF is visibly heterogeneous in each experimental animal.

Table 10 summarizes cerebral flow data in the U87 model. We compiled the data by ROI to look for regional trends beyond the visible heterogeneity. Tumor flow over the center and middle regions was 120 ± 40% higher than flow in contralateral brain. Regional analysis showed lower CBF values at the tumor edge as defined by the outer regions of low T2* in post-contrast images.

Looking at voxel-wise CBF distributions within animals, we find a relatively narrow distribution of flows in striatum with a wide range of distributions (0.3 to 3.5, relative to striatum) in tumor (Figure 15). We find that normal or even low flow does not differentiate between tumor and normal tissues. In this group, the average CBF was nearly twice that of contralateral striatum.

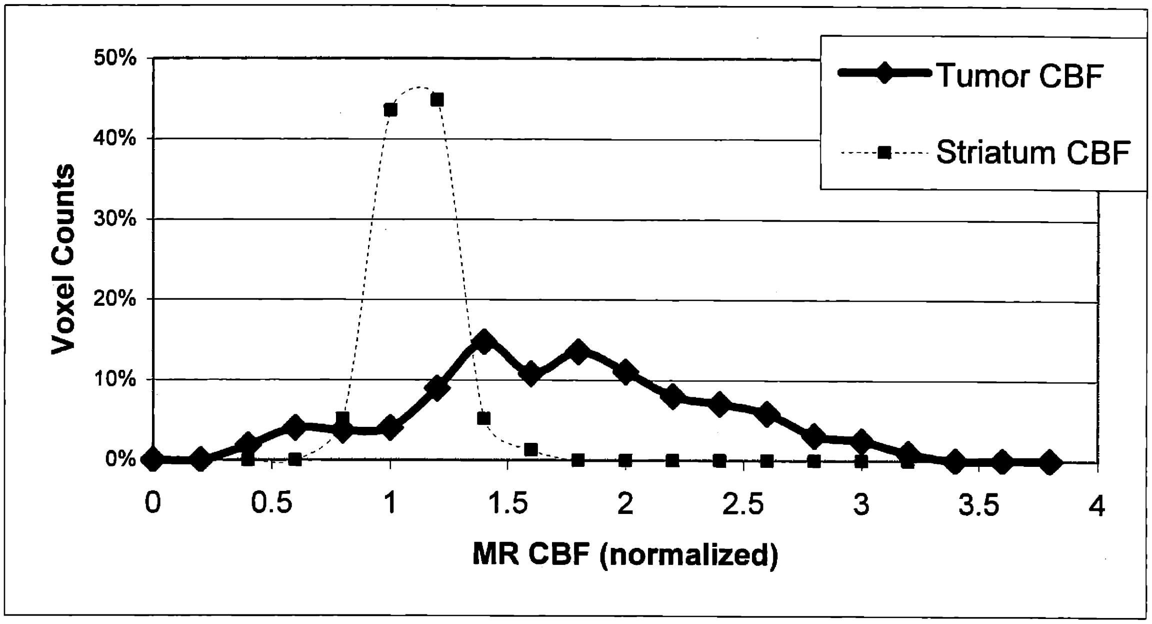

Figure 15 Distribution of Cerebral Blood Flow in n=4 subset of rats. Tumor blood flow is heterogeneous and elevated overall, but CBF does not differentiate tumor from striatum.

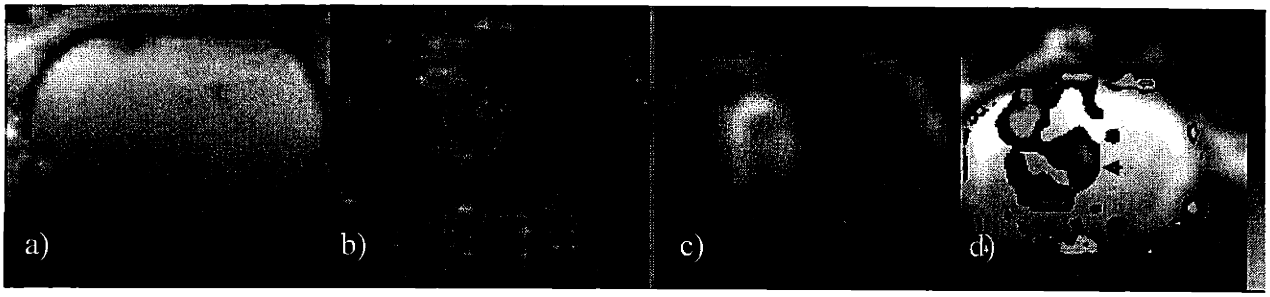

Figure 16. Flow/volume mismatch in U87MGdEGFR glioblastoma. a) Conventional GE proton-density weighted image for anatomical localization. b) Conventional GE CBV map. c) EPI GE CBF map. d) Perfusion Efficiency map overlay on anatomical image.

Having shown that MR blood volume and mean vessel size techniques are linear with true histological values, we pursued the relationships between these parameters and blood flow. Images in Figure 16 were derived with gradient echo sequences. Figure 16a and Figure 16b are from conventional sequences (TR/TE : 2500/22 msec; flip angle = 90°) while Figure 16c was acquired using EPI (TR/TE : 225/22 msec; with a flip angle = 40°). Relative CBV was determined by $\Delta R2^*$ calculated from injection of steady state contrast agent MION 3 mg/kg. Relative CBF was determined from the time courses of bolus injections of 1 mg/kg MION contrast agent. Figure 16a is the conventional proton density weighted anatomical image. The brain is rather unremarkable except for a dark spot near the brain surface indicating minor hemorrhage at the local of the needle track. Figure 16b is the gradient echo derived cerebral blood volume map. The boundary of this large tumor is clear. There exists considerable heterogeneity in blood volume in this tumor, which is typical of our findings in this tumor model. Figure 16c is relative cerebral blood flow. From inspection we see that high flow exists within the tumor and also around the edge of the brain probably due to the presence of large draining veins with large throughput. Figure 16d shows the regions of greatest CBF/CBV mismatch. Image C was divided by image B; the color overlay depicts voxels in which perfusion efficiency (CBF/CBV) is more than one standard deviation beneath the value in normal brain. This overlay is placed on top of a single anatomic slice. Note the highlight along the injection track where tissue damage has occurred, disturbing the flow/volume relationship. While perfusion efficiency is diminished overall, it accentuates the periphery (arrowhead).

Using all of the magnetic susceptibility contrast techniques we have discussed, we compiled an array of maps from one typical rat through the center of its glioma. Figure 17a,b are the total and microvascularly-weighted blood volume maps. Each shows the elevated and heterogeneous nature of tumor blood volume overall and when weighted towards to the smallest vessels. Figure 17c shows a different pattern of elevation, although heterogeneity is present here as well.

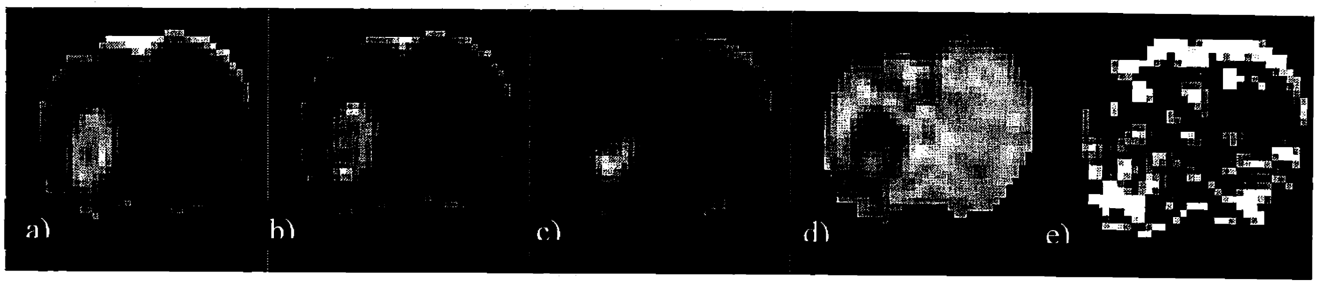

Figure 17 Full array of MR images obtained using susceptibility contrast techniques and an intravascular contrast agent. a) GE (total)CBV b) SE (microvascularly-weighted) CBV c) CBF d) Perfusion Efficiency (PE) e) Mean Vessel Size (MVS). All maps through the same 1mm thick slice through the tumor center from U87MGdEGFR bearing rat.

To understand where flow and volume are poorly matched we generated a perfusion efficiency map (Figure 17d) to highlight these regions. The dark zones of this image represent diminished perfusion efficiency and greatest flow/volume mismatch and while occurring widely in the tumor, are of particular note in the tumor periphery. Figure 17e shows vessel size by the $\Delta R2^*/\Delta R2$ metric. The brain is well outlined and there exist high values in the tumor region, although not exclusively there.

The mismatch between blood flow and blood volume pictured in Figure 17d is of particular interest. As we hypothesize changes in perfusion efficiency due to tumor angiogenesis we expect to find such flow volume mismatches in regions that are undergoing or have undergone drastic increases in angiogenesis, such as the periphery of a tumor. Another way to explore this mismatch is to plot CBF and CBV for each voxel, clustered by region. Figure 18 shows CBV/CBF scatter in normal brain (yellow and pink) and tumor (blue). Each data point represents one voxel. CBF values range between 0.5 and 4.7. CBV values were more widely distributed, between 0.2 and 9.0 (high CBV outlier data not shown).

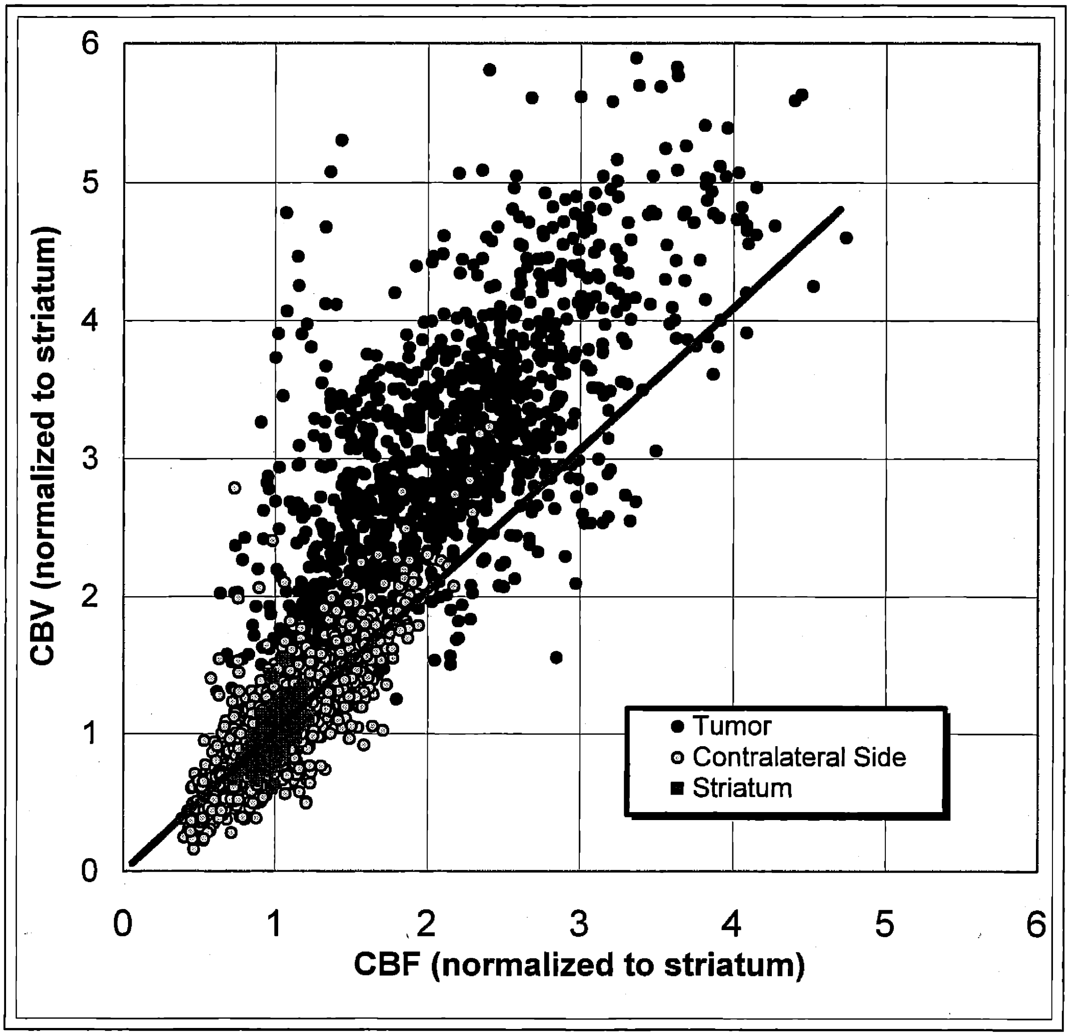

Figure 18 Voxel-wise depiction of flow/volume mismatch in tumors. CBV/CBF ratio reliably identifies tumor voxels. Each point represents one voxel in each brain region – composite of 10 rats. Normal tissues fall on a line of unity while tumor generally lies above this line of normality.

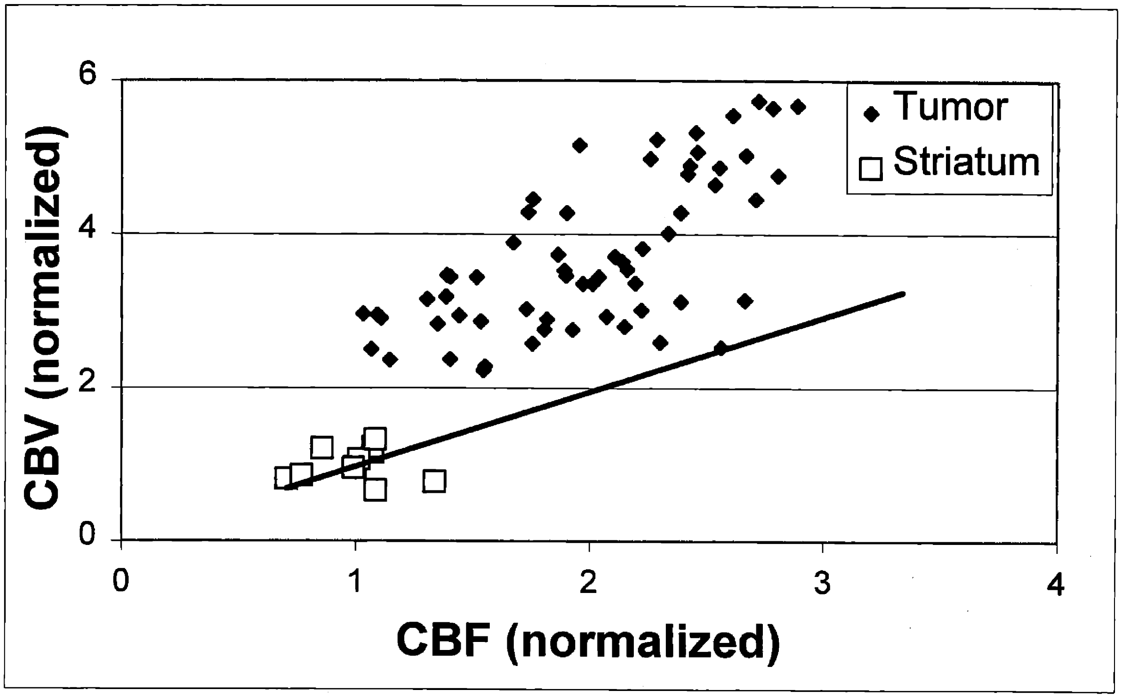

Figure 19 CBF/CBV ratio data from a single tumor-bearing rat. Tumor and striatum are clearly separated.

Figure 19 illustrates the robust nature of the perfusion efficiency metric. The presence of tumor disrupts the natural flow/volume relationship to the extent that even within a single rat it is possible to clearly differentiate tumor (blue) from contralateral striatum (red). Relative values of CBF were scaled to the mean of the contralateral striatum. Values for striatum are tightly clustered around unity and this variance can be taken as a natural metric of the variability in this tissue. Tumor-based values for CBF tend to be high, while CBV values were much greater in tumor than in striatum. Tumor and striatum are differentiated, or separable, by CBV, although not by CBF. From both sets of data, we also see the predicted mismatch between flow and volume in each animal, suggesting the hypothesized effect of neovascularity contributing more to blood volume than to blood flow.

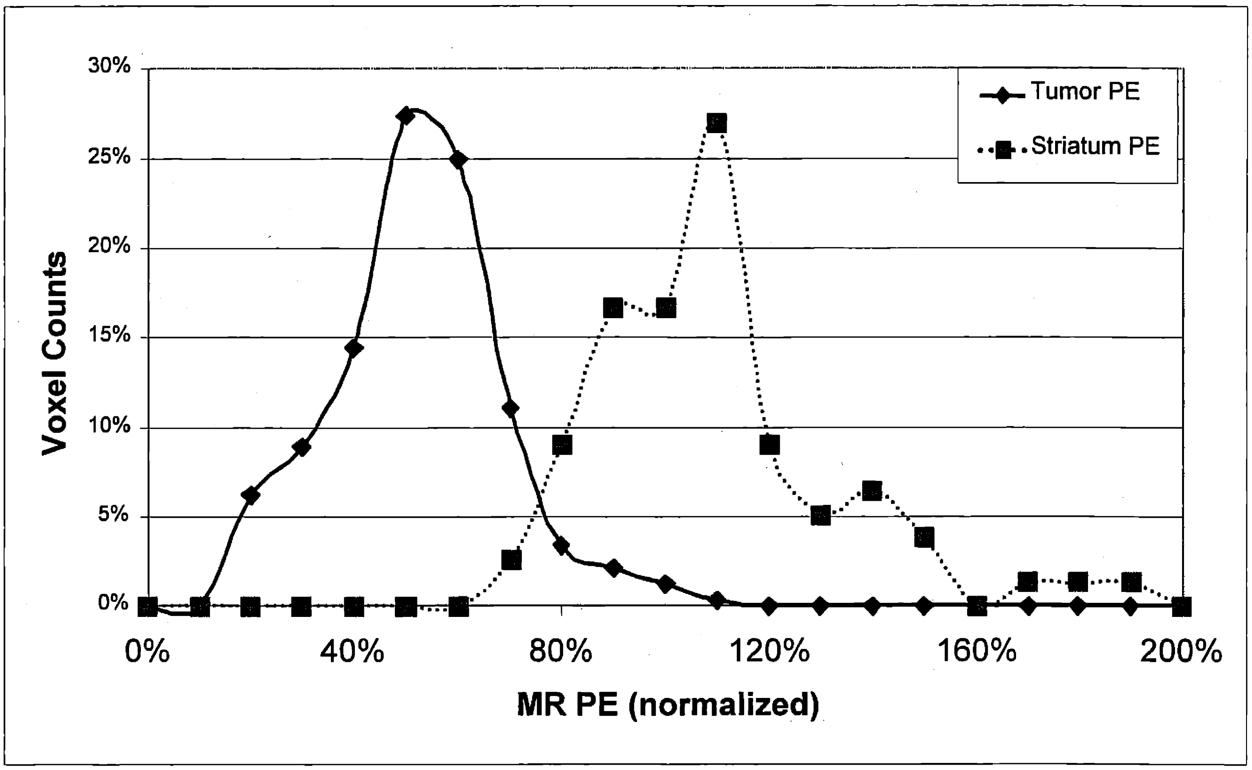

Figure 20 Distribution of Perfusion Efficiency (n=4) within tumor and contralateral striatum. Tumor expresses a lower perfusion efficiency and similar variance.

To see hypothesized differences in perfusion efficiency distributions between tumor and striatum, we plotted the distribution of perfusion efficiency map voxel values from normal brain and tumor from U87MGdEGFR bearing rats (n=4) (Figure 20). Striatum is defined as normal and is therefore centered at 100% efficiency. The percentage of voxels was used rather than the raw number of voxels to aid in comparison between the two differently sized ROIs. The tumor PE distribution exhibits a lower median (50%) but not a different variace ($p > 0.1$, f-test). We conclude that tumor perfusion efficiency is diminished ($p < 10^{-6}$, pooled t-test with unequal variance) compared to normal contralateral striatum.

Figure 16d is an example of low perfusion efficiency accentuating the tumor periphery. To investigate this phenomenon further, we looked at the spatial relationship of perfusion efficiency in an n=10 subset of rats with the most spherical and well-shaped tumors Figure 21. Tumor Edge perfusion efficiency was significantly diminished with respect to Tumor Center ($p = 0.018$). No necrosis was found in any of the histologically examined rats, suggesting that lowered PE in the tumor edge is not an artifact of cell death, but truly reflecting the mismatch between blood flow and blood volume that is especially severe at the proliferating tumor edge.

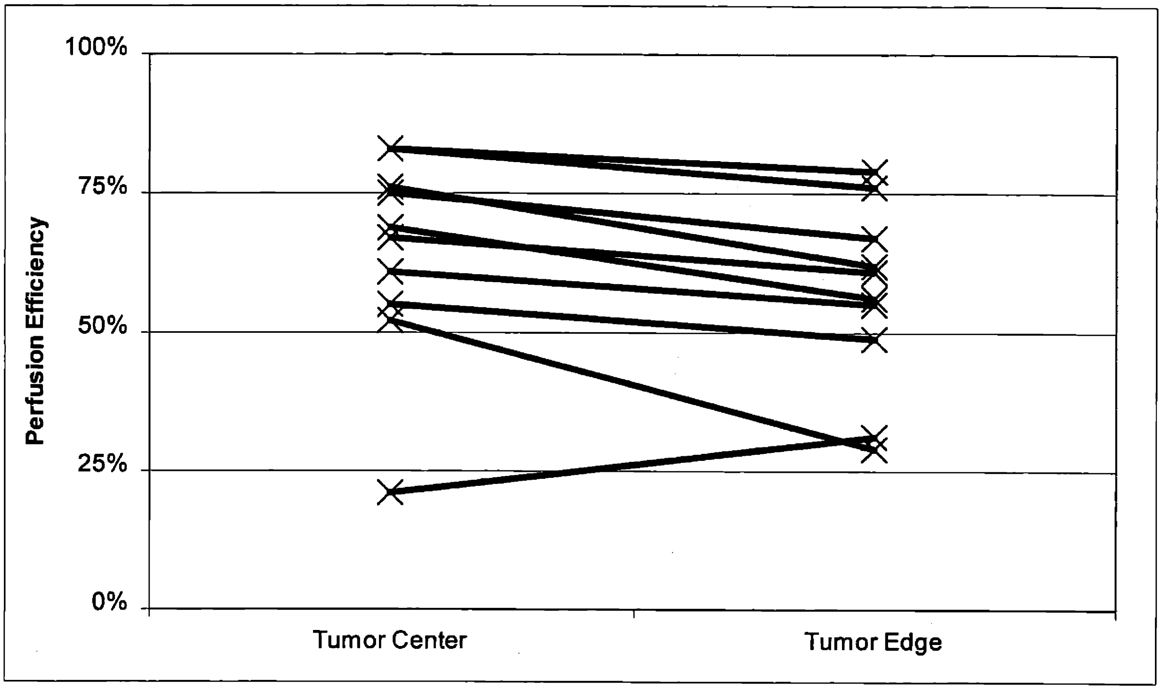

Figure 21 Perfusion efficiency by region in N=10 subset of rats. In 9/10, perfusion efficiency was lower in tumor edge than in tumor center (p = 0.018 by paired t-test).

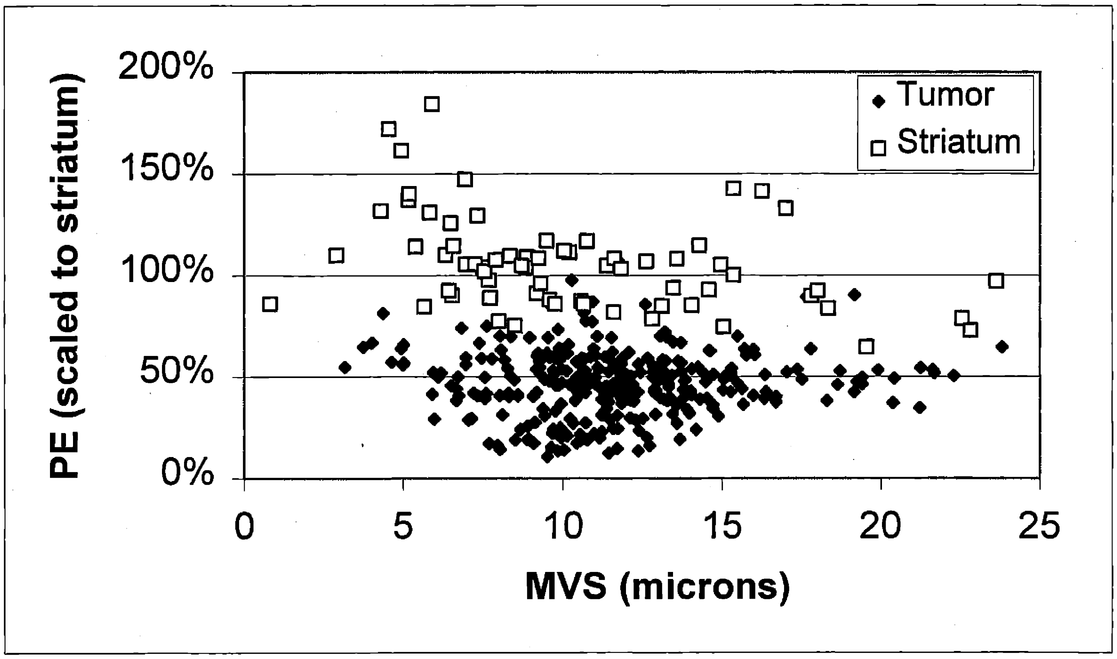

Figure 22 Perfusion efficiency (PE = CBF/CBV) appears uncorrelated with mean vessel size, but does reliably separate tumor from normal tissue in the U87MGdEGFR model (N=4). Diminished perfusion efficiency is found to be a hallmark of disturbed vasculature.

One potentially confounding effect with respect to decreased perfusion efficiency is the possibility that we are merely seeing a hydrodynamic effect -- that perfusion efficiency varies with vessel radius due to the mechanics of fluid transport in a pipe-like structure. In such a structure, fractional changes in CBF are proportional to the square of changes in CBV. This is contrary to the flow/volume relationship that we observe, where increases in CBV are greater than CBF changes. We find that there is no correlation between perfusion efficiency and mean vessel size in tumor ($r = 0.05$, $p > 0.1$) or striatum $r = 0.03$, $p > 0.1$) in the regime in which we are imaging (Figure 22). We conclude that the MRI derived mean vessel size metric and perfusion efficiency are independent for capillary-sized objects. The smallest striatum vessels in Figure 22 indicate that there may be a perfusion efficiency-size relationship for the smallest of capillaries, but further studies focused on these smallest vessels or other extremely small perturbers could resolve this issue.

Comparison Between Tumor Lines

It is difficult to make conclusions about the utility and reliability of an imaging technique that has not been verified in more than one model. In addition to our extensive imaging of the U87MGdEGFR model, we also examined the GLI36MGdEGFR tumor line. Imaging of the GLI36 model was performed using the same MRI parameters as imaging of the U87 tumor line. Additionally, all animal preparation and surgeries were performed using the same procedures. Tumors were size-matched rather than time-matched to eliminate potentially confounding effects of differences in tumor size that could not be addressed here but will be examined in future longitudinal studies.

As GLI36 is known to be a less vascular tumor model than the U87 based on vascular staining experience (E.A. Chiocca, personal communication), we expected and found lower relative total and microvascular CBV in GLI36 compared to U87, although both were well above normal values in contralateral striatum ($p < 0.001$, pooled t-test). The MR determined values are presented in Table 11. Total CBV was elevated by 180% in GLI36 while microvascular CBV was 60% higher than in normal brain tissue. There were no statistical differences in MVS between the two tumor lines ($p > 0.1$, pooled t-test, unequal variance). However, total CBV was greater in U87 than GLI36 ($p = 0.03$, pooled t-test, unequal variance). There was also a difference in the microvascular CBV between the two tumor lines ($p = 0.0002$, pooled t-test, unequal variance). This is especially interesting because it supports the known difference in vascularity between the two tumor lines. This reality was reflected in the microvascular CBV but not in the total CBV or CBF parameters. This fact is another validation of the importance of microvascular CBV imaging and its relevance to tumor physiology. Both tumor lines exhibited significant flow/volume mismatch. While there was not a statistically significant difference between the PE values for the two tumor lines, they were both significantly different from striatum (U87: $p<10\text{-}^{5}$, n=11; GLI36: $p<0.016$, n=4).

		GE CBV	SE CBV	ΔR2*/ΔR2	CBF	PE
U87	MEAN	3.4	2.4	1.5	2.1	69%
	SEM	0.2	0.2	0.1	0.1	4%
GLI36	MEAN	2.8	1.6	1.7	1.9	80%
	SEM	0.2	0.0	0.2	0.1	5%
P-value, U87 vs. GLI36		0.03	0.0002	0.7	0.5	0.1

Table 11 Comparison of MR data from U87 (N=15) and GLI36 (N=4) tumor lines. While there are many subtle differences, only CBV was significantly different between the tumor lines by pooled, twotailed t-tests.

Discussion

This chapter has focused on MR-measured parameters of tumor physiology and morphology. By imaging rats bearing human gliomas, we were able to refine, validate, and apply MR metrics to further our knowledge of the tumor vasculature as compared to the normal matrix of blood vessels. We found a strong differentiation by CBV between tumor as defined by our ROIs and contralateral striatum. We also used vascular stains to demonstrate the accuracy by which CBV measurements match vascular area. We have also explored the relationship between blood flow and blood volume in tumors, a parameter we call "perfusion efficiency," reflecting the amount of flow scaled by the total space of the vascular network. Perfusion efficiency, or flow per unit volume scaled to the internal standard of contralateral striatum, was diminished in tumors. We also found evidence supporting especially low PE around the edge of tumors as defined by our ROIs, indicating that the tumor angiogenesis of these regions is related to perfusion efficiency as we originally hypothesized. The microscopic determination of mean vessel size within a voxel and its direct histological correlation was another seminal point of this work. Based on previous studies, we used the MR parameter $\Delta R2^*/\Delta R2$ as a marker of vessel size. We verified this relationship in excised tissue and showed significant increases in vessel size within tumors compared to normal brain. These results will be placed in the context of previous work and generally agree well with more invasive established techniques. Now some of the key findings will be discussed in more depth.

Morphometry

Immunohistochemical verification of our MR morphology measuring techniques is critical to their persuasive application. We showed strong correlations between histological values and MR values of vascularity and vessel size. The alkaline phosphatase stain, as described and used in the perfused vascularity literature, worked well in distinction to other vascular stains like Factor VIII and CD31 which, in these studies, failed to stain the tumor vasculature. These techniques did, however, adequately mark the contralateral vessels. This suggests additional ways in which the tumor vaculature is abnormal. These vessels must have damaged or missing cellular receptors that normally conjugate with the antibody/marker complex. One may argue this occurrence is an artifact of the use of the mutant epidermal growth factor strain of the U87MG and GLI36 tumors. Nonetheless, the successful application of NBT/BCIP permitted us to use histology as a "gold standard" by which to compare our MRI-based CBV and MVS findings. We plotted the convergence of histological measurements as a function of number of vessels counted to ensure adequate sampling. In a typical rat tumor, counting less than 100 vessels yielded values within 10% of the final value at over 900 vessels (Figure 4). Based on this data, our approach of counting approximately 800 vessels ensures sufficient sampling for tumors. For the striatum we counted nearly all the vessels.

We discovered highly elevated CBV, both total and microvascularly-weighted, in the U87 tumor line. This assumes that post-contrast T2*-weighted images from which our ROIs were drawn accurately reflect the tumor boundary. As high vascularity is a requirement for extended tumor growth and not all tumors are gadolium enhancing, our approach is a reasonable one. As high blood volume, generally referred to in histology as high vascular area, is a hallmark of tumors, elevated CBV is not a surprise and has been recorded by our group and others in the past using first-pass bolus techniques. Our steady-state approach to CBV is more consistent and accurate than first-pass techniques since it is a simpler measurement and easily repeatable in animals due to our intravascular contrast agent (Lin, Celik et al. 1999). In the near future, following human-use approval for such agents, this technique will be readily extendable to humans. We found excellent correlation between vascular area and microvascularly weighted CBV, and slightly less good, but still statistically significant, correlation between stained vessel area and total CBV. Since we found by histology that all the regions of interest in the brain were dominated by capillaries, it is reasonable that microvascular CBV correlation coefficient was higher than the total CBV correlation coefficient. Distributions of CBV voxels determined by MRI and histologically-measured high powered fields are strikingly similar, additionally supporting our conclusion that MRI CBV measurements do accurately reflect the vascular space.

The issue of fractionally-perfused vasculature confounds the measurement of vascularity. Pre- and post-contrast MR images are taken over a period of 24 minutes. We therefore have a window in which to catch vessels whose perfusion status could be time-dependent in such a time-frame. Such vessels would be weighted by perfused-time and CBV. Fortunately, recent work discussed in Chapter 2 has shown rat brain perfusion levels of 95%, which would minimize the problems in measuring CBV associated with perfusion status. However, if older values are believed, as few as 50% of the brain capillaries may be perfused at any given time. If this were the case, our estimates of CBV, both total and microvascular, would underestimate the true blood volume. From our data, the excellent fits between CBV and vascular area suggest that we are indeed measuring the entire vasculature quite well and lend credence to very high perfusion fractions in rat brain, particularly in the presence of neoplasia.

The cause of tumor blood volume elevation could involve both the increase in number of vessels by angiogenesis as well as the dilation of pre-existing vessels. By histology, we know that both factors are involved. We showed elevated CBV by MRI, and by using the $\Delta R2^*/\Delta R2$ metric, we determined, at subvoxel resolution, a 50% increase in mean vessel size in U87 tumor regions. Again, we successfully correlated this MRI parameter with the only available comparison – MVS as determined by vessel counting and sizing. This process is so time consuming that it is not done in the clinical setting, and only very rarely even in research. As discussed in the introduction, there are several known correlations between CBV and clinical parameters. The complexity of the vessel size measurement has hindered correlation studies with parameters of clinical interest. Our verified tool will permit research along these lines to begin in earnest.

Having quantified CBV and MVS elevation in tumor, we explored their distributions, on both a regional and voxel scale. The only regional trend, seen in both CBV and MVS, was for the tumor edge to exhibit lower values. This finding is likely a reflection of differences at the tumor boundary. There were no differences in CBV and MVS between the tumor center and tumor middle ROIs. At the voxel scale, we find heterogeneity in both the CBV and MVS parameters. The distribution of CBV of tumors was greater than that of striatum as seen by the plot in Figure 6 and visually in Figure 5a,b. The large distribution in vessel sizes seen in tumors was similar to that of contralateral striatum as seen in Table 7 and Figure 5c. While tumor vessel sizes were significantly larger than those of striatum, their size distribution widths were similar. This suggests that while the vessels grown through tumor angiogenesis are tortuous and larger than their normal counterparts, they seem to be grown consistently. Perhaps the metabolic needs of the tumor drive the production of vessels large enough to deliver what is required but not so large that transport becomes inefficient due to transport/extraction issues encountered in very large vessels.

While the agreement between mean vessel size as determined by histology and MRI is good and statistically significant, it is not a perfect correlation. Why is there significant variability in these values and only a modest correlation coefficient? One issue is the innate variability in vessel sizes within tumor regions. Tumor angiogenesis is notorious for producing tortuous vessels, often larger, and highly variable. The MR MVS metric presented here does not yield any information about the distribution of vessels, simply the average radius within the voxel. Vessel size distribution by MRI would allow for more complete characterization of the vascular bed and is a prime direction for future work. One possible approach would be to employ an array of asymmetric spin echoes to filter the vasculature to different degrees, as we have done to the extreme in the spin echo case.

Another cause for variability between MRI and histological MVS is the set of assumptions made by the Monte Carlo model upon which the relaxivity/susceptibility relationship is based. As with analytical approaches, simplifications must be made to create a tenable model. While the Monte Carlo simulations of Boxerman and Weisskoff do address issues left unexplored by previous analytical work, one major discrepancy between model and reality is clear. Cylinders of uniform radii were used to determine signal changes at numerous vessel sizes. There were no simulations exploring the effect of a continuous vascular size distribution, as clearly exists in biology. Also, true vessels are not cylinders, particularly in regions of tumor angiogenesis where it is well known that vessels are tortuous with blind-ends and distorted pre-vascular buds. Such major differences between model and reality are certain to cause discrepancies that are difficult to predict, especially by analytical methods. Future work will involve modifying the model to permit the simulation of vascular distributions and even real vascular distribution data.

A final potential source of discrepancy between MRI and histological mean vessel size arises from the highly variable vascular areas themselves. Most of the simulation work was carried out for volume fractions under 10%. In tumors we experienced vascular areas of 15% routinely with some data over 20%, compared to striatum values of 1-4%. There is a slight non-linearity with very high vascular volume between the increase in ΔR2* and ΔR2: mean vessel size will be overestimated in comparison to normal physiological volume fractions. From Boxerman et al.(Boxerman 1994), projecting to the highest measured tumor blood volume fraction, we should overestimate mean vessel size by no more than 18%.

Given the existence of the ΔR2*/ΔR2 to histology mean vessel size relationship, one can estimate the average microvessel size within an MRI voxel – a non-invasive biopsy of sorts, orders of magnitude beyond the size scales of macrovessel angiography (Leclerc, Gauvrit et al. 1999). We transcend the traditional boundary of resolution, inferring microscopic characteristics two orders of magnitude smaller than the MRI point spread function. This correlation may be determined with greater statistical significance by examining a wider array of vessel sizes. It was not possible to exploit the large draining veins on the surface of the brain to accomplish this task due to unavoidable averaging with non-vascular space beyond these vessels.

Our histological validation of MRI MVS transcends the earlier work of Dennie et al. (Dennie, Mandeville et al. 1998), in which we employed histologically-determined vessels sizes averaged over a tumor as the input for monte carlo simulations of the ΔR2*/ΔR2 parameter. In that paper, we found good overall agreement between real and simulated MR signal, averaged over all C6 tumors, reflecting mean vessel size based on magnetic susceptibility contrast. Here we directly correlate mean vessel size by MRI and histology from multiple tumor regions and striatum in multiple animals. From this data we constructed a regression relationship from which we can scale the ΔR2*/ΔR2 parameter directly to microns.

Others have taken analytical approaches, in contrast to the numerical basis for this work, to derive expressions of MR parameters related to vessel size, although no other group has correlated MR MVS data and histology in the same animals. Troprès et al. developed analytic expressions for transverse relaxivity from gradient and spin echoes: ΔR2* and ΔR2, respectively (Tropres, Grimault et al. 2001). Based on previous work of Yablonskiy and Haacke (Yablonskiy and Haacke 1994), they show a previously derived expression for ΔR2*. Troprès et al. then proceed to show data comparing their analytical and monte carlo models and demonstrate great similarity between them and slight non-linearities with respect to $\Delta R2^*$ and $\Delta R2$. When their in vivo data are presented, they make an excellent fit ($R>0.95$) with a sublinear curve, although it is apparent that a best fit line (based on $\Delta R2^*/\Delta R2$) would also provide an excellent fit.

Jensen et al. propose another approach to the imaging of microvascular parameters (Jensen and Chandra 2000). They derive a contrast agent independent factor $Q = \Delta R2/(\Delta R2^*)^{2/3}$. They go on to suggest that Q is correlated with the diffusion constant and with vascular density. They test their theory using the data from Dennie et al.(Dennie, Mandeville et al. 1998) and show reasonable fit to that data and no significant dose dependence. While they have eliminated contrast agent dependence under their stated assumptions, the purported problem of dose dependence has never been an issue in our work. As long as inter-animal contrast agent concentrations do not vary by more than an order of magnitude, there is little dose dependence (Boxerman, Hamberg et al. 1995). It seems likely that the stated assumption of uniform infinite cylinders used in both numerical and analytical treatments is a greater factor with regard to the overall accuracy of MR microvascular mapping techniques.

Pathak et al performed experiments designed to explore the relationship between CBV and histological vessel area and vessel density (Pathak, Schmainda et al. 2001). Using a latex casting technique, they found relatively poor correlation between MRI CBV and vessel area, but a good correlation with fractional vessel density utilizing an established stereologic algorithm. Perhaps the vascular area correlation was not revealed due to a property of the casting material or perhaps the 50μm thickness of the slices in that study forced the stereologic correction. Our work indicates an excellent correlation between MRI CBV and vascular area without the need for any correction terms.

Physiology

Having explored tumor morphology in great detail and having provided histological proof for the efficacy of these techniques, we then proceeded to address the relationship between blood flow and blood volume which is well understood and well regulated in healthy brain tissues. In tumor pathology, however, we find significant disturbance in this relationship. We hypothesized such an effect due to sudden rampant angiogenesis, from which we expected greater increases in blood volume than blood flow, resulting in low flow per unit volume, or diminished perfusion efficiency. Next, we discuss these findings and suggest their implications.

To complement the steady state determination of highly elevated CBV, we applied a dynamic bolus tracking method to extract a measure of relative CBF. We found CBF to be elevated as well, although not nearly as much as the total CBV elevation (110% compared to 240%). Regionally, there was a gradient of highest CBF in the tumor center decreasing towards the tumor margin (Table 10). Voxel-wise analysis showed greater CBF heterogeneity in tumors than in striatum (Figure 15). While histological validation was not possible, there has been significant work in the field that shows the reliability of these MR CBF measurements with respect to older, highly invasive techniques. CBF measurements by USPIO bolus tracking have also been shown to be compatible with more conventional gadolinium-based imaging in a study in which the authors measured cerebral blood flow (CBF) and cerebral blood volume (CBV) by bolus tracking of a an ultrasmall superparamagnetic iron oxide (USPIO) contrast agent (NC100150) and compared absolute and relative perfusion measurements with those obtained by a standard gadolinium-based contrast agent (Simonsen, Ostergaard et al. 1999). They found a linear correlation between the two methods and a high degree of reproducibility of repeated absolute as well as relative CBF and CBV values. This is important because gadolinium based bolus tracking is currently possible in the clinic, whereas MION-like contrast agents are not yet approved for human use.

The identification of flow/volume mismatch took two forms. The first was the creation of perfusion efficiency maps, defined by CBF/CBV. The second was the generation of voxel-wise plots of CBF and CBV. Each illustrates the phenomenon that we call flow/volume mismatch and diminished perfusion efficiency. Our picture of rampant angiogenesis driving neovascular sprouting led us to the hypothesis that these new vessels would be both large (high MVS) and numerous (high CBV). But they would also demonstrate inefficient meshing with the vascular matrix, blind-ending sacs, and partially-formed blood-containing vessels, causing only a modest increase in CBF with respect to the CBV elevation. We then proved this CBF/CBV mismatch in each animal, comparing perfusion efficiency between normal and tumor regions. Visually, from the voxel-wise PE plot (Figure 20), the difference between tumor and normal tissue is obvious.

Figure 21 shows diminished PE in tumor periphery compared to tumor center. We take this finding as excellent evidence supporting the hypothesis of flow/volume mismatch, of particular note around the tumor periphery due to current and rampant tumor angiogenesis.

The best-fit line in Figure 18 is essentially the line of normality around which the normal brain flow/volume relationship exists; scatter within normal tissues is elliptically centered on this line. Within tumor, a different relationship exists. The significant deviation from this line of normality suggests that tumors grow their vessels in an unusual way – not surprising given the influence of rapid tumor angiogenesis compared to the slow time scale of healthy neovascularity. A typical tumor voxel exhibited high CBF and even higher CBV. Tumor-based vessels exhibit low perfusion efficiency – low flow per unit volume. The variation in both the CBV and CBF dimensions are obviously much greater for tumor than for striatum. Such images acquired at a fairly late stage of the tumor's development suggest questions regarding the time scale of the development of these mismatched regions of vasculature. Future longitudinal studies will allow us to investigate this phenomenon over time, using each rat as its own control.

The relevance of perfusion efficiency has been discussed in more detail in Chapter 2. This parameter may prove to be off great utility in identifying regions of angiogenesis. The measurement and longitudinal monitoring of natural or drug-induced changes is one potential application. We show that perfusion efficiency is unrelated to vessel size (Figure 22). This finding not only allows us to consider these measurements as complementary information, but also raises the potential of using them in unison to provide a broader picture of the vascular state. That perfusion efficiency variance is not different in this tumor line than striatum (from Figure 20) indicates that this value is relatively uniform for a given tissue type and that it is the mean, not the variance, of perfusion efficiency that is the parameter of interest when studying tumor biology with this technique. Future study will define the role of perfusion efficiency imaging as a diagnostic technique in the research and clinical settings.

Cancer is not the first pathology in which flow/volume mismatch has been observed. In a study of stroke (Caramia, Huang et al. 1998), there have been areas identified peripheral to the occluded middle cerebral artery with increased blood volume but without significant CBF changes ($p > 0.05$). During reperfusion, CBF increased in the entire zone showing changes in blood volume during occlusion, and remained significantly elevated until 45 min post-occlusion, while CBV remained elevated in the hyperemic rim for at least 2 h. The authors of this study suggested that the presence of a peri-ischemic zone showing flow/volume mismatch identified a region wherein baseline CBF is maintained by means of compensatory vasodilatation, but where the ratio of CBF to CBV is decreased. A similar finding had been made invasively by Tomita et al. via frequent blood sampling (Tomita, Gotoh et al. 1980).

Mismatches between blood flow and blood volume are not limited to stroke. Lammertsma et al. published their investigation of the flow volume relationship in human tumor patients by PET imaging in 1983 (Lammertsma, Wise et al. 1983). In 21 patients with cerebral tumors, they found blood flow and volume to be variable and unrelated even in tumors of the same type and grade. In the contralateral gray and white matter a (linear) relationship was found between rCBF and rCBV. It is likely that the lack of spatial resolution and the variability of the human tumors prevented identification of local flow volume mismatch in these cerebral lesions. In the Mineura study (Mineura, Yasuda et al. 1986), tumor CBF and CBV were variable and unrelated to grades of tumor malignancy.

Changes in the flow/volume relationship have even been seen in a study of spontaneous non-aural migraine headache by PET imaging (Bednarczyk, Remler et al. 1998). The measured relative cerebral blood flow decreased between 16-53% while cerebral blood volume decreased 6-33%, resulting in an increased tissue transit time (10-54%). These values are qualitatively similar to our findings in gliomas – greatly increased CBV and moderately increased CBF leading to lower flow per unit volume. They are not in accordance with Grubb's Law for changes in CBV and CBF due to changes in $PaCO_2$, which would predict CBF changes greater than the concurrent CBV changes.

The ratio CBF/CBV has been suggested as an index of cerebral perfusion pressure, a parameter that is of particular interest in focal ischemia. In one study, cortical CBF, CBV, cerebral metabolic rate for oxygen ($CMRO_2$) and oxygen extraction fraction were measured by PET using the ^{15}O steady-state technique in 10 anaesthetized baboons(Schumann, Touzani et al. 1998). The

CBF/CBV ratio decreased significantly at all stages of hypotension (-21 and -31%) and was significantly increased during hypertension (+30%). The CBF/CBV ratio demonstrated a significant correlation with MAP ($r = 0.78$, $p < 0.01$). These results indicate that cortical CBF/CBV is significantly correlated with CPP, itself a function of MAP. In the investigated range of MAP, the relationships between CBF/CBV and MAP appeared to be linear.

Summary

In this work, we correlated the $\Delta R2^*/\Delta R2$ mean vessel size parameter and total and microvascularly-weighted CBV with histology in rat models of human glioma. We also found a significant flow/volume mismatch in tumors, particularly around the tumor edge, indicating diminished perfusion efficiency in tumors with respect to normal brain. These techniques could be useful for pre-clinical drug development, the study of tumor biology, and clinical monitoring of human patients

Aronen, H. J., I. E. Gazit, et al. (1994). "Cerebral blood volume maps of gliomas: comparison with tumor grade and histologic findings." Radiology **191**(1): 41-51.

Aronen, H. J., J. Glass, et al. (1995). "Echo-planar MR cerebral blood volume mapping of gliomas. Clinical utility." Acta Radiol **36**(5): 520-8.

Aronen, H. J., F. S. Pardo, et al. (2000). "High microvascular blood volume is associated with high glucose uptake and tumor angiogenesis in human gliomas." Clin Cancer Res **6**(6): 2189-200.

Bednarczyk, E. M., B. Remler, et al. (1998). "Global cerebral blood flow, blood volume, and oxygen metabolism in patients with migraine headache." Neurology **50**(6): 1736-40.

Boxerman, J. L. (1994). Non-invasive Measurement of Physiology Using Dynamic Susceptibility Contrast NMR Imaging. Health Sciences and Technology. Cambridge, Harvard-MIT.

Boxerman, J. L., L. M. Hamberg, et al. (1995). "MR contrast due to intravascular magnetic susceptibility perturbations." Magn Reson Med **34**(4): 555-66.

Caramia, F., Z. Huang, et al. (1998). "Mismatch between cerebral blood volume and flow index during transient focal ischemia studied with MRI and GD-BOPTA." Magn Reson Imaging **16**(2): 97-103.

de Jong, J. S., P. J. van Diest, et al. (1995). "Heterogeneity and reproducibility of microvessel counts in breast cancer." Lab Invest **73**(6): 922-6.

Dennie, J., J. B. Mandeville, et al. (1998). "NMR imaging of changes in vascular morphology due to tumor angiogenesis." Magn Reson Med **40**(6): 793-9.

Dewhirst, M. W., C. Y. Tso, et al. (1989). "Morphologic and hemodynamic comparison of tumor and healing normal tissue microvasculature." Int J Radiat Oncol Biol Phys **17**(1): 91-9.

Fisel, C. R., J. L. Ackerman, et al. (1991). "MR contrast due to microscopically heterogeneous magnetic susceptibility: numerical simulations and applications to cerebral physiology." Magn Reson Med **17**(2): 336-47.

Folkman, J. (1971). "Tumor angiogenesis: therapeutic implications." N Engl J Med **285**(21): 1182-6.

Folkman, J. (1992). "The role of angiogenesis in tumor growth." Semin Cancer Biol **3**(2): 65-71.

Folkman, J. and D. Hanahan (1991). "Switch to the angiogenic phenotype during tumorigenesis." Princess Takamatsu Symp **22**: 339-47.

Jain, R. K. (2001). "Normalizing tumor vasculature with anti-angiogenic therapy: a new paradigm for combination therapy." Nat Med **7**(9): 987-9.

Jensen, J. H. and R. Chandra (2000). "MR imaging of microvasculature." Magn Reson Med **44**(2): 224-30.

Lammertsma, A. A., R. J. Wise, et al. (1983). "In vivo measurements of regional cerebral blood flow and blood volume in patients with brain tumours using positron emission tomography." Acta Neurochir (Wien) **69**(1-2): 5-13.

Leclerc, X., J. Y. Gauvrit, et al. (1999). "Contrast-enhanced MR angiography of the craniocervical vessels: a review." Neuroradiology **41**(12): 867-74.

Lin, W., A. Celik, et al. (1999). "Regional cerebral blood volume: a comparison of the dynamic imaging and the steady state methods." J Magn Reson Imaging **9**(1): 44-52.

Mignot, J., D. Barres, et al. (1981). "[Histological morphometric methods. I. Semi-automatic methods on graphic tables (author's transl)]." Ann Pathol **1**(2): 152-5.

Mineura, K., T. Sasajima, et al. (1994). "Perfusion and metabolism in predicting the survival of patients with cerebral gliomas." Cancer **73**(9): 2386-94.

Mineura, K., T. Yasuda, et al. (1986). "Positron emission tomographic evaluation of histological malignancy in gliomas using oxygen-15 and fluorine-18-fluorodeoxyglucose." Neurol Res **8**(3): 164-8.

Nishikawa, R., X. D. Ji, et al. (1994). "A mutant epidermal growth factor receptor common in human glioma confers enhanced tumorigenicity." Proc Natl Acad Sci U S A **91**(16): 7727-31.

Ostergaard, L., R. M. Weisskoff, et al. (1996). "High resolution measurement of cerebral blood flow using intravascular tracer bolus passages. Part I: Mathematical approach and statistical analysis." Magn Reson Med **36**(5): 715-25.

Pathak, A. P., K. M. Schmainda, et al. (2001). "MR-derived cerebral blood volume maps: issues regarding histological validation and assessment of tumor angiogenesis." Magn Reson Med **46**(4): 735-47.

Rosen, B. R., J. W. Belliveau, et al. (1991). "Susceptibility contrast imaging of cerebral blood volume: human experience." Magn Reson Med **22**(2): 293-9; discussion 300-3.

Schumann, P., O. Touzani, et al. (1998). "Evaluation of the ratio of cerebral blood flow to cerebral blood volume as an index of local cerebral perfusion pressure." Brain **121 (Pt 7)**: 1369-79.

Simonsen, C. Z., L. Ostergaard, et al. (1999). "CBF and CBV measurements by USPIO bolus tracking: reproducibility and comparison with Gd-based values." J Magn Reson Imaging **9**(2): 342-7.

Tomita, M., F. Gotoh, et al. (1980). ""Low perfusion hyperemia" following middle cerebral arterial occlusion in cats of different age groups." Stroke **11**(6): 629-36.

Tropres, I., S. Grimault, et al. (2001). "Vessel size imaging." Magn Reson Med **45**(3): 397-408.

Weiss, H. R., E. Buchweitz, et al. (1982). "Quantitative regional determination of morphometric indices of the total and perfused capillary network in the rat brain." Circ Res **51**(4): 494-503.

Yablonskiy, D. A. and E. M. Haacke (1994). "Theory of NMR signal behavior in magnetically inhomogeneous tissues: the static dephasing regime." Magn Reson Med **32**(6): 749-63.

Vascular Reactivity to Physiological Perturbation

We now discuss the second component of our interrogation of tumor vascularity. Having explored the relationships of blood flow, blood volume and vessel size, we now turn our attention to the functional status of tumor vessels. With a better understanding of the baseline characteristics of tumor vessels with respect to their normal counterparts, we now test vasoreactivity in response to physiological challenges. Studying a system through its reaction to perturbation is a time-honored approach in science.

There are five well-understood perturbation characteristics of cerebral vasculature. The first is matching between blood flow and blood volume; increases in flow are linked to increases in blood volume. We explored this relationship in the previous chapter. The second cerebrovascular relationship is CBF and subsequent CBV response to changes in $PaCO_2$ and will be explored here. Integrity of the blood brain barrier, or blood tumor barrier, is the next characteristic and is studied in the next chapter. The other two relationships are autoregulation and flow/metabolism coupling.

In this work, we interrogate the capacity of tumor vessels to dilate and constrict in response to changes in $PaCO_2$, one of the fundamental qualities of cerebrovaculature . To test the hypothesis that CBV response to changing $PaCO_2$ is not preserved in the context of tumor vessels, we applied two perturbations. The first perturbation is the addition of 5% CO_2 to the breathing mixture of the rats. CO_2 inhalation induces hypercarbia, the elevation of blood $PaCO_2$ levels. Hypercarbia is known to increase CBF and, according to Grubb's relation, CBV(Grubb, Raichle et al. 1974). By this approach, we test vasodilation. The second stimulus we employ is hyperventilation, a well-known method of reducing $PaCO_2$ and consequently causing vasoconstriction. Combining these two approaches, we paint a picture of bi-directional CBV changes with respect to significant alterations in $PaCO_2$. We then compare tumor and contralateral striatum CBV reactivity to gain an understanding of the functional status of these vessels.

Abramovitch et al. have used vessels' response (or lack thereof) to carbogen inhalation as an assay of functionality(Abramovitch, Frenkiel et al. 1998). Vessels with significant BOLD signal increases were considered functional. Rather than the composite measure of BOLD signal change, we chose to measure CBV, a direct hemodynamic parameter. Vessels' ability to change diameter due to a physiologic perturbation is a well-characterized phenomenon. Others have measured normal reactivity to CO_2 inhalation in the brain of anesthetized rats (Todd, Weeks et al. 1993; Payen, Vath et al. 1998; Zaharchuk, Bogdanov et al. 1998; Cenic, Nabavi et al. 2000). This common physiologic challenge has been shown to increase both blood flow and blood volume in these animals.

In this chapter, we seek to better understand the dynamic vascular physiology of tumors in a human glioma transfected into athymic rats. The reactivity properties of tumor vasculature have not yet been studied in such gliomas and could illuminate functional pathophysiology. Since our primary tumor cell line is a human glioma, U87MGdEGFR, our results in the rat model may translate well to non-infiltrative human neoplasia. We also extend the study of vascular reactivity into the realm of vasoconstriction, a functionality that has not been previously examined in this context of tumor physiology. Combining measurements of vasodilation and vasoconstriction, we create a more complete picture of vasoactivity in glioma.

Methods

Glioma implantation

The U87MGdEGFR human glioblastoma cells were a generous gift of Dr. H.-J. Su Huang (University of California at San Diego). This cell line was established by retroviral transfer of a mutant epidermal growth factor receptor (de 2-7 EGFR) into U87MG human glioblastoma cell line, enhancing its tumorigenic capacity in the brain of nude mice (Nishikawa, Ji et al. 1994). Cells were grown in Dulbecco's modified Eagle medium (DMEM) supplemented with 10% fetal bovine serum, 100 U/ml penicillin, 100ug/ml streptomycin, and 50ug/ml G418 at 37°C in 5% CO_2.

GLI36dEGFR5 is a human malignant glioma cell line, stably transduced with a recombinant retrovirus expressing mutant epidermal growth factor receptor (de 2-7 EGFR) (Ichikawa and Chiocca, unpublished experiments). These cells were grown at 37 C in an atmosphere containing 5% CO_2 in Dulbecco's Modified Eagle Medium (DMEM) supplemented with 10% heat-inactivated fetal calf serum, 100U/ml of penicillin, 100 μg/ml of streptomycin, and 0.5 μg/ml of puromycin (SIGMA, Saint Louis, MO).

Animal Preparation

Animal studies were performed in accordance with guidelines issued by the Massachusetts General Hospital Subcommittee on Animal Care. Adult female nude rats (rnu/rnu) were anesthetized with an intraperitoneal injection of 0.5ml of 0.9% NaCl containing 12.5mg of ketamine and 2.5mg of xylazine. After immobilizing the rats in a stereotactic apparatus and placing a linear skin incision over the bregma, a 1mm burr hole was drilled in the skull approximately 1mm anterior and 2mm lateral to the bregma on the right side. 200,000 U87MGdEGFR cells (in a 2ul volume) were injected at a depth of 3.5mm from the dura, using a 5ul Hamilton syringe.

Animal Maintenance

Fisher rats were anesthetized with 1.5% halothane in oxygen for surgery; a tracheostomy was performed, and femoral arterial and venous cannulae were inserted. Following surgery, rats were mechanically ventilated with 0.7% halothane in a mixture of air and oxygen using a 3 ml tidal volume, a rate of 40 breaths per min, and an inspiration to expiration ratio of 1:1. After initiation of mechanical ventilation, rats were paralyzed with a 2 mg/kg bolus of pancuronium followed by continuous intravenous infusion at 2 mg/kg/hr. To minimize motion artifact, rats were placed into a custom plastic cradle attached to a head frame machined from plastic (David Kopf Instruments, Fremont, CA); heads were fixed with plastic screws inserted into the ear canals and a bar inserted under the front incisors. The rat torso was wrapped in two heating blankets

(Gaymar, Orchid Park, NY) that circulated water at 40° C to maintain body temperature. Rat heads were shaved and covered with gel toothpaste to reduce magnetic susceptibility artifacts arising from the air-tissue interface. The ear canals and oro-pharynx were also filled with toothpaste.

Imaging protocols

Between ten and thirteen days after implantation, the animals underwent imaging on a 2T 11cm bore SISCO NMR image Spectrometer (Varian Associates, Fremont, CA) using a custom-built surface coil. Before contrast agent injection, baseline spin echo and gradient echo echo planar images were obtained via an interleaved double echo protocol ($TR/TE_{GE}/TE_{SE} = 2500/22/60$ ms, FOV 2.5 X 2.5 cm, slice thickness 1mm, in-plane resolution: 780 μm, n=60 averages). A total dose of 3 mg/kg of MION was then injected.

An imaging sequence utilizing the same parameters recorded GE and SE images every 20 seconds to track changes due to vasoreactivity. In n = 9 animals, following a baseline period of approximately 5 minutes, 5% CO_2 was added to the gas mixture, inducing hypercarbia. Imaging continued for approximately 10 minutes to track the resulting image intensity changes. In the other n=9 animals, the transition to hypocarbia was induced via hyperventilation. This transition was imaged via the same MR imaging protocol. Blood gas measurements were taken just prior to and just after imaging to calibrate blood volume changes with the magnitude of change in blood $PaCO_2$.

Rat core temperature and mean arterial blood pressure (MABP) were monitored throughout the imaging session. Blood gas analysis yielding pH, and partial pressures of CO_2 and O_2 was carried out periodically via samples drawn from the femoral artery.

Regions of interest (ROIs) were created for tumor, contralateral striatum and contralateral cortex based on post-contrast T2* weighted images. These ROIs were applied to the MR data yielding the values reported in the section below.

Results

Rats were scanned in two separate cohorts (n=9 each) so as to minimize potential hysteresis effects. One rat was permitted in both cohorts as the vasoconstriction experiment was performed first and seemed to have no effect of the vasodilation portion of the experiment.

Blood gas measurements were made in all animals to track $PaCO_2$ status and health. $PaCO_2$ values for baseline, hypercarbia, and hypocarbia are presented in Table 12. The mean PaCO2 value for the baseline state was 37.5 mmHg. The mean values for hypo- and hypercarbia were 24.5 mmHg and 61.3 mmHg respectively. There was no significant difference between the baseline states in the two cohorts ($p > 0.1$). In each component of the experiment, there was a significant change from baseline to perturbed $PaCO_2$ state ($p < 0.001$).

Transition to Hypercarbia			Transition to Hypocarbia		
Rat	Baseline	Hypercarbia	Rat	Baseline	Hypocarbia
04/20/99	37.0	60.4	06/28/00a	33.0	20.9
05/04/99	41.5	58.6	02/07/01a	47.9	32.3
06/15a/99	38.6	59.5	02/07/01b	49.0	22.6
06/15b/99	36.5	63.8	02/07/01c	37.7	23.0
07/27/99	32.0	56.7	04/02/01a	32.9	26.6
08/10/99	39.9	61.8	04/02/01b	35.8	20.9
09/28/99	34.5	59.1	04/03/01a	36.9	24.5
10/05/99a	37.0	61.7	04/03/01b	36.2	25.2
06/28/00a	33.0	69.8	04/03/01c	34.8	24.8
Mean	36.7	61.3	Mean	38.2	24.5
St. Dev.	3.1	3.8	St. Dev.	6.0	3.5

Table 12 $PaCO_2$ values for baseline and perturbed states. Left) Values for the transition from normocarbia to hypercarbia. Right) Values for the transition from normocarbia to hypocarbia. In both cases the differences in $PaCO_2$ reached statistical significance ($p < 0.001$, paired t-test). There was no difference between the baseline states in the two cohorts ($p > 0.1$).

Having successfully manipulated $PaCO_2$ status, we then analyzed the MR CBV data to see whether hypercarbia and hypocarbia induced vasodilation and vasoconstriction. From the total and microvascular (GE and SE) MR data, we plotted percent change in CBV as a function of time during these metabolic transitions from normcarbia (Figure 23). In all cases, there were roughly five minutes of baseline images from which the baseline CBV was determined. Subsequent CBV changes were then recorded as percent changes from these values for each animal. Typical normal tissue total CBV increases in the transition to hypercarbia were 15-25% (Figure 23a), slightly lower for microvascular CBV increases (Figure 23b). Hypocarbia induced CBV changes in striatum were on the order of 15% (Figure 23c,d) for both total and microvascularly-weighted CBV. These CBV changes were all clearly significant ($p < 0.001$, pooled t-test between baseline and final values) compared to the baseline values.

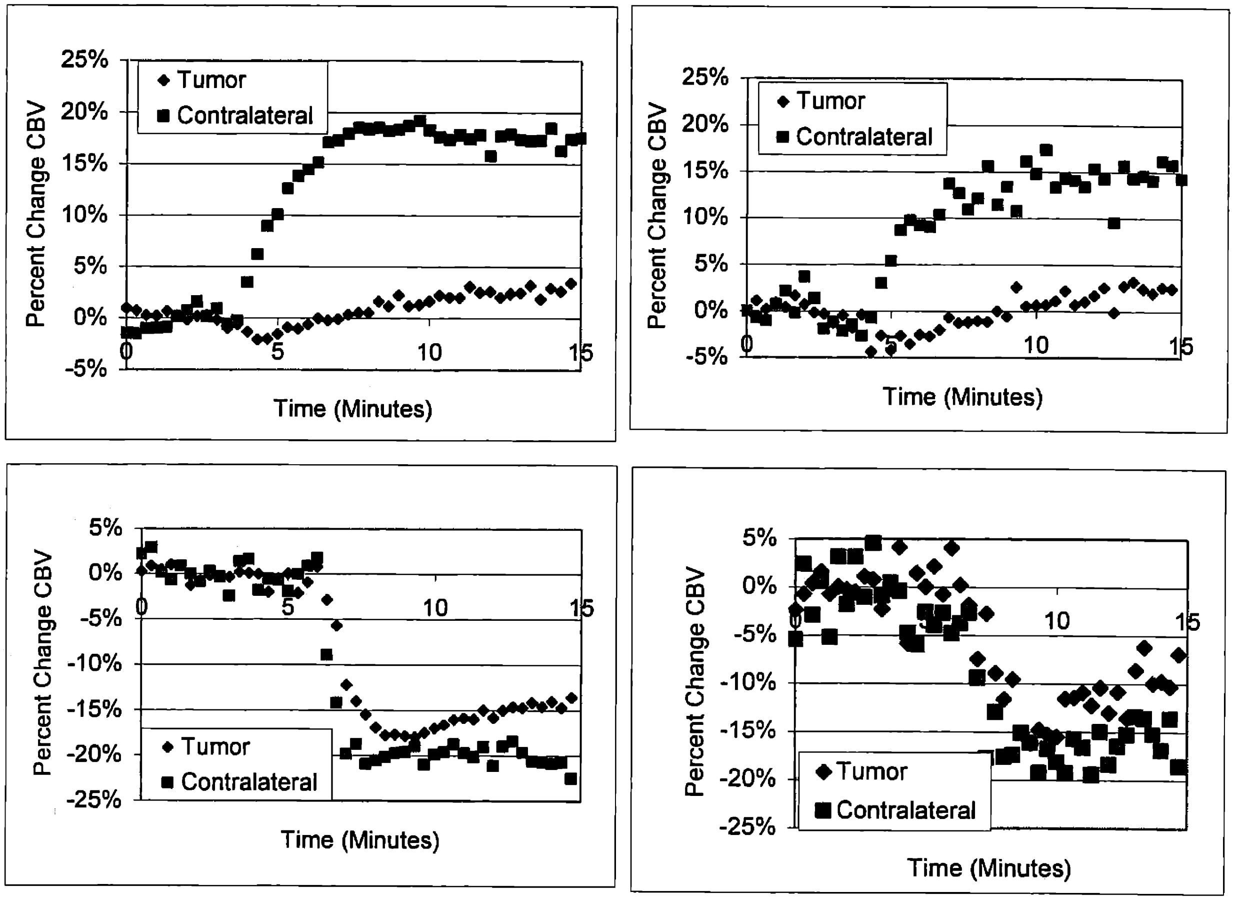

Figure 23 Percent CBV changes induced by changes in $PaCO_2$. a) and b) illustrate sample transitions to hypercarbia measured by total CBV (a) and microvascular CBV (b). c) and d) correspond to transitions to hypocarbia as measured by total CBV (c) and microvascular CBV (d). Measurements were made every 20 seconds for 15 minutes.

To appropriately compare results across animals and compensate for variations in blood gas findings, we scaled each animal's CBV change by the measured change in $PaCO_2$. We found three statistically significant differences (Table 13). CBV response to hypocarbia induction was less than CBV response to hypercarbia in contralateral striatum ($p < 0.04$, pooled t-test), but this difference was not seen in tumor ($p = 0.1$, pooled t-test). During the transition from normocarbia to hypercarbia we see diminished tumor vasodilation compared to contralateral striatum ($p = 0.0001$, paired t-test). The difference between the CBV reactivities of these two different tissues is graphically displayed in Figure 24. Next, we compared the measured differences in the total vasculature (by GE) as opposed to the microvascularly-weighted compartment (by SE). The only statistically significant difference was in the transition to hypercarbia, where striatum reactivity via GE was 1.5 ± 0.1 compared to 1.0 ± 0.1 by SE, a difference that reached significance ($p=0.006$, paired t-test).

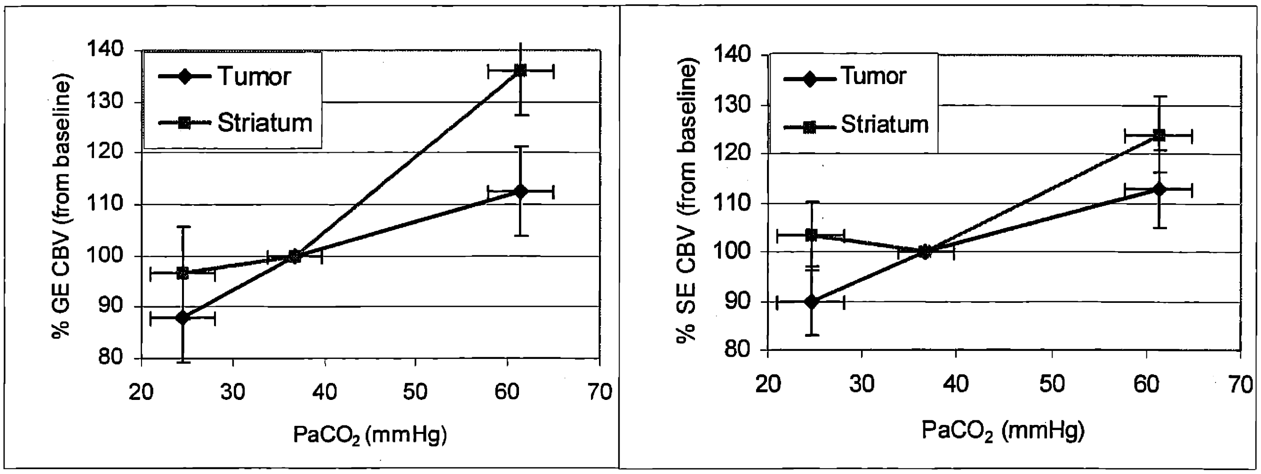

Figure 24 Summary of CBV Reactivity for total CBV (left) and microvascularly-weighted CBV (right).

		GE		SE	
Transition	**Tumor Line**	**Tumor**	**Striatum**	**Tumor**	**Striatum**
Normal to Hypercarbia	U87	$0.5 \pm 0.1^{*}$	$1.5 \pm 0.1^{*\wedge\#}$	0.5 ± 0.1	$1.0 \pm 0.1^{\wedge}$
	GLI36	1.3 ± 0.3	1.2 ± 0.4	0.7 ± 0.1	1.3 ± 0.7
Normal to Hypocarbia	U87	1.0 ± 0.2	$0.3 \pm 0.3^{\#}$	0.8 ± 0.2	-0.3 ± 0.5
	GLI36	1.8 ± 0.8	1.8 ± 0.1	0.5 ± 0.5	0.7 ± 0.7

Table 13 Total and Microvascularly-weighted CBV response (percent change CBV per mmHg CO_2) for two tumor lines. Values presented are Mean ± SEM. Superscripts indicate statistically significant difference between values ($p < 0.05$, paired t-test).

Discussion

Our evaluation of CBV changes due to physiologic challenge required precise manipulation of blood $PaCO_2$ levels. Arterial blood gas sampling permitted us to measure these values while we successfully controlled $PaCO_2$ through inhalation of CO_2 gas and hyperventilation. We studied vascular changes, measured as changes in blood volume from our MR data, in tumor-bearing rats during transitions from normocarbia to hyper- and hypocarbia. With this information we looked for differences in behavior between tumor and striatum, hypercarbic and hypocarbic reactivity, and GE- and SE-measured CBV response.

As is common in tumors, we found highly elevated blood volume in comparison with the contralateral tissue and this elevation was consistent across animals – although heterogeneous within each animal. Vasoreactivity is one parameter by which one may test for differences between normal and tumor-sprouted vessels. The non-invasive determination of the bi-directional vasoactive properties of tumors has not yet been achieved. We interrogated our tumor model in two ways, to measure not only the dilation capability of these vessels, but also their constrictive potential. It has been demonstrated by others that tumor vessels often lack some dilation functionality when challenged by the breathing of carbogen (Abramovitch, Frenkiel et al. 1998) (Neeman, Dafni et al. 2001). Carbon dioxide intake should induce increased blood flow, and concurrently, if Grubb's law holds in these cases, blood volume. Their finding implies a functional disability of these vessels and indeed they have been labeled as non-functional. In this work we also found diminished response to tumor vessels to vasodilating stimuli in one tumor line, but not such change in response in a second glioma..

Our intention in imaging the second tumor line, GLI36, was simply to verify that the CBV tracking techniques were not specific to the first tumor line. By tracking blood volume in the second tumor line, we show the breadth of potential application for CBV reactivity across tumor types. Having accomplished this goal, we were then surprised by two findings. First, we found a trend (although not significant) that GE CBV response to hypercarbia in the GLI36 was greater that that of U87, and that GLI36's tumor response was similar to the striatum response. While we found diminished vasodilation in U87, we do not see it in GLI36. Second, striatum vasoconstriction was significantly greater in the GLI36 than the U87. Yet, these are the same rats and there should no physiological differences in their striata. Further work will be required to understand the causes of this paradox.

Our data are suggestive of a few things. First, the blanket statement that vessels spawned by tumor angiogenesis are non-functional is false. Even if the tumor-based vascular bed does not respond to hypercarbia as normal tissue does, that does not prove that those vessels are incapable of vasoactivity. Therefore the technique by which immature vessels are defined by changes during carbogen breathing as measured by BOLD contrast (Abramovitch, Frenkiel et al. 1998) is insufficient to define the functional status of vessels. Second, vascular reactivity could be characteristic of individual tumor lines. Further study will be required to prove or disprove the hypothesis that vascular reactivity could be a marker of malignancy or level of angiogenesis – both of which would be extremely useful in the clinic and research settings.

Comparison With Previous Work

Our results compare favorably to other studies. Grubb, in his original work, determined a reactivity of 1.2% ΔCBV/ΔmmCO$_2$, in reasonable agreement with our finding of 1.5% ΔCBV/ΔmmCO$_2$ (Grubb, Raichle et al. 1974) for hypercarbia. Payen et al. used gradient echo CBV mapping and found 1.3 ± 0.3 % ΔCBV/ΔmmCO$_2$ during the transition to hypercarbia in the striatum of normal rats, also agreeing well with our results in the non-lesion side of the brain

(Payen, Vath et al. 1998). In a separately published follow-up, they considered the transition to hypocarbia and found essentially the same value 1.4 ± 0.3 % $\Delta CBV/\Delta mmCO_2$ (Payen, Briot et al. 2000). Again, this is in marked contrast with our finding of diminished hypocarbic CBV response, even contralateral to the lesion.

Zaharchuk et al. used the CAPTIVE method to measure CBF and CBV simultaneously using arterial spin tagging in rats without tumors (Zaharchuk, Bogdanov et al. 1998). They found 1.8 % $\Delta CBV/\Delta mmCO_2$ over a 40 mmHg CO_2 range for total blood volume, and a 2.1 % $\Delta CBV/\Delta mmCO_2$ value for their microvascularly-weighted component of the experiment. Both values are somewhat high in comparison with the established literature, possibly due to hemispheric brain averaging. Lin et al. measured GE CBV in rats as a function of $PaCO_2$, finding a CBV reactivity of 1.0% $\Delta CBV/\Delta mmCO_2$ (Lin, Paczynski et al. 1997).

Cenic et al. studied the changes in CBV and CBF during propofol anesthesia in rabbits using dynamic contrast-enhanced CT to measure CBV and radiolabelled microsphere to measure CBF (Cenic, Craen et al. 2000). The CT scanning method permitted imaging of one 3mm coronal slice through the brain at the optic chiasm in a 12 minute protocol. Simulataneously, blood was aspirated from a femoral artery catheter which measured the concentration of the CT contrast agent (a radiographic contrast material, 1.5 mL/kg iopamidol). CBF was determined by a left atrial injection of radioactive microspheres. Tissue samples from the kidneys (to verify adequate microscphere mixing) and brain were taken along with arterial blood samples. Gamma ray spectroscopy was used to quantify the presence of the microspheres.

They found no significant difference in CBV or CBF during the transition from normo- to hypo-carbia. They did see significant vasodilation ($p < 0.05$) with CBV increasing from 2.41ml/100g to 3.08 mL/100g, yielding a normalized increase of 1.66% $CBV/mmCO_2$. This value is close to but somewhat higher than that of Todd et al. (Todd, Weeks et al. 1993) and our findings in normal brain contralateral to tumor. They attempt to explain the lack of vasocontriction as typical due to low $PaCO_2$ and nearly-saturated vasocontraction prior at normocarbia. This suggestion does not mesh well with our findings and the findings of others in this carbon dioxide tension regime. While it is true that the vasoactive response diminishes at very low $PaCO_2$, the linear regime of response exists well into the 25mm CO_2 regime where it flattens greatly between 25 and 15mmCO_2. It seems more likely that the effect is due to the presence of propofol.

Todd et al explored the measured CBV response to changes in blood CO_2 tension at three states (Todd, Weeks et al. 1993). They determined a vascular reactivity to increases in $PaCO_2$ of 1.43% CBV/mmCO_2 with animals sacrificed by microwave fixation, while decapitated rats had a lower CBV response value lesser, 0.56% CBV/mmCO_2. The microwave determined value is in excellent agreement with our findings in vivo using CBV imaging.

There has also been recent interest in human vasoactivity. Hamberg et al. tested CBV reactivity in normal humans using CT scanning and found it only in human gray matter (Hamberg, Hunter et al. 1996). This was in contrast to finding CBF changes by the same method in both gray and white matter regions, suggesting this method is sub-optimal for studying such CBV changes. They also explored CBV response by CT in rats, with results in line with ours and others discussed (Hamberg, Hunter et al. 1996). Powell et al investigated CBF effects of carbogen breathing in humans using invasive microprobes. They found little or no change in bulk perfusion in most cases, with large changes in perfusion in a small sub-sample of subjects (Powell, Hill et al. 1996). A recent study by Reinstrup et al explored CBV changes in humans due to hypocarbia with and without the presence of N_2O using SPECT (Reinstrup, Ryding et al. 2001). They found a small value, averaging over several parts of the brain, 0.37 ± 0.14 % ΔCBV/ΔmmCO_2. Interestingly, in these normal volunteers, they found a value of reactivity that nearly matches our finding for vasoconstrictive reactivity in tumors but not our vasoconstrictive reactivity in striatum. N_2O did not influence the reactivity.

These literature values for rats are in general agreement with our findings. However, none of these studied looked at the effect of tumors. Our contralateral striatum reactivity values seem to mesh well with the literature in the transition to hypercarbia, but not for hypocarbia. This fact suggests inhibition, either directly or indirectly, by the tumor of normal vessel constriction. Perhaps the intracranial environment is such that these vessels are already compressed, by pressure from the tumor bulk and increased blood volume such that there is little room for additional vasoconstriction.

SUMMARY

Our findings indicate that the carbogen-breathing test is not an ideal method of evaluating overall vascular functionality, as it tells only half the story. While tumor-sprouted vessels have impaired reactivity to CO_2 inhalation, this fact does not mean they are incapable to being affected by vasoactive stimuli. We have shown that these particular tumor vessels do indeed react to vasoconstrictive stimuli, and in fact, do so quite robustly. Bi-directional tumor blood vessel reactivity to changes in $PaCO_2$ is different than in normal tissues. This difference can be exploited to understand the functionality of tumor vessels and potentially as a useful assay in clinical or pre-clinical settings.

Abramovitch, R., D. Frenkiel, et al. (1998). "Analysis of subcutaneous angiogenesis by gradient echo magnetic resonance imaging." Magn Reson Med **39**(5): 813-24.

Cenic, A., R. A. Craen, et al. (2000). "Cerebral blood volume and blood flow at varying arterial carbon dioxide tension levels in rabbits during propofol anesthesia." Anesth Analg **90**(6): 1376-83.

Cenic, A., D. G. Nabavi, et al. (2000). "A CT method to measure hemodynamics in brain tumors: validation and application of cerebral blood flow maps." AJNR Am J Neuroradiol **21**(3): 462-70.

Grubb, R., M. Raichle, et al. (1974). "The effects of changes in PaCO2 on cerebral blood volume, blood flow, and vascular mean transit time." Stroke **5**: 630-639.

Hamberg, L. M., G. J. Hunter, et al. (1996). "Quantitative high-resolution measurement of cerebrovascular physiology with slip-ring CT." AJNR Am J Neuroradiol **17**(4): 639-50.

Lin, W., R. P. Paczynski, et al. (1997). "Quantitative measurements of regional cerebral blood volume using MRI in rats: effects of arterial carbon dioxide tension and mannitol." Magn Reson Med **38**(3): 420-8.

Neeman, M., H. Dafni, et al. (2001). "In vivo BOLD contrast MRI mapping of subcutaneous vascular function and maturation: validation by intravital microscopy." Magn Reson Med **45**(5): 887-98.

Nishikawa, R., X. D. Ji, et al. (1994). "A mutant epidermal growth factor receptor common in human glioma confers enhanced tumorigenicity." Proc Natl Acad Sci U S A **91**(16): 7727-31.

Payen, J. F., E. Briot, et al. (2000). "Regional cerebral blood volume response to hypocapnia using susceptibility contrast MRI." NMR Biomed **13**(7): 384-91.

Payen, J. F., A. Vath, et al. (1998). "Regional cerebral plasma volume response to carbon dioxide using magnetic resonance imaging." Anesthesiology **88**(4): 984-92.

Powell, M. E., S. A. Hill, et al. (1996). "Effect of carbogen breathing on tumour microregional blood flow in humans." Radiother Oncol **41**(3): 225-31.

Reinstrup, P., E. Ryding, et al. (2001). "Cerebral Blood Volume (CBV) in Humans during Normo- and Hypocapnia: Influence of Nitrous Oxide (N2 O)." Anesthesiology **95**(5): 1079-82.

Todd, M. M., J. B. Weeks, et al. (1993). "Microwave fixation for the determination of cerebral blood volume in rats." J Cereb Blood Flow Metab **13**(2): 328-36.

Zaharchuk, G., A. A. Bogdanov, Jr., et al. (1998). "Continuous assessment of perfusion by tagging including volume and water extraction (CAPTIVE): a steady-state contrast agent technique for measuring blood flow, relative blood volume fraction, and the water extraction fraction." Magn Reson Med **40**(5): 666-78.

Chapter 6 – Tumor Permeability Response to Anti-Angiogenic Therapy

Introduction

In this chapter we discuss the third experimental component of our exploration of tumor vascularity: transport across vascular tight junctions. It is well known that tumors are dependent on angiogenesis for continued growth and metastasis (Folkman 1971). Increased understanding of tumor angiogenesis is leading to the development of many novel cancer treatments including KDR inhibition, a particularly promising avenue of anti-angiogenic therapy (Shaheen, Davis et al. 1999), and the development of potent and selective KDR inhibitors suitable for oral administration in humans. As KDR activation mediates increased vascular permeability, KDR inhibitors may induce acute permeability changes (Gille, Kowalski et al. 2001). In pre-clinical and clinical trials of such therapeutics with non-traditional endpoints, non-invasive and repeatable assays of pharmacodynamic efficacy are sought – consequently, the rapid response of vascular permeability to KDR blockade may prove to be a suitable biomarker for assessing the efficacy of KDR inhibitors.

Dynamic contrast enhanced magnetic resonance imaging (DCE-MRI) methods permit quantitative visualization of contrast agent extravasation – an index of vascular permeability (Taylor, Tofts et al. 1999). Our approach to DCE-MRI is based on rapid sampling of the signal time course following intravenous bolus administration of a clinically available gadolinium-based contrast agent, gadopentetate dimeglumine. To determine the acute vascular permeability effects of a KDR inhibitor, we imaged a syngeneic rat gliosarcoma model (GS-9L/lacZ) that secretes high levels of VEGF and exhibits elevated vascularization compared to normal striatum (Plate, Breier et al. 1993). Building upon an established two compartment model (Tofts, Brix et al. 1999), we quantitatively measured acute changes in vascular transport before and one to six hours after a single application of the oral KDR inhibition therapy. In doing so, we introduce a useful, minimally invasive, surrogate marker of early permeability effects due to vascular-targeted therapies.

Materials and Methods

Cell Culture. Cells from the LacZ-modified gliosarcoma line were grown in Dulbecco's Modified Eagle's Medium (DMEM) supplemented with 10% Fetal Bovine Serum (FBS) and 1% penicillin/streptomycin at 37°C in 5.5% CO_2 with medium change every 3-5 days. Injection cells were washed in HANKS solution and trypsinized with 0.05%/0.53 mM Trypsin/EDTA solution. Cells were re-suspended in HANKS at $1x10^8$ cells/ml, 10 μl was placed in syringe and used for intracerebral injections. All cell culture reagents were from Cellgro, Mediatech, Washington, D.C.

Tumor Model. Animal Studies were performed in accordance with guidelines issued by the Massachusetts General Hospital Subcommittee on Animal Care. Fisher 344 rats weighing 200-235 g were anesthetized with isoflurane (induction 5%, maintenance 1% in 70% oxygen, balance nitrous oxide). Using an electric drill equipped with a burr hole bit, a hole was drilled through the skull exposing the dura. A 70uL Hamilton syringe with a 23 gauge needle was then loaded with 30uL of 9L/LacZ cell suspension (1,000,000 cells / ml). 10 uL of the suspension (10^6 9L/LacZ gliosarcoma cells) were implanted into the striatum via stereotactic injection 0.2mm anterior, 3.2mm lateral of the bregma, and at a depth of 4mm. The injection dynamics were 2 minutes for insertion, 20 minutes for injection, two minutes post-injection pause, and 4 minutes withdrawal time. The hole was sealed with bone wax and the wound closed with 3-0 silk suture. Rats were allowed to recover with full access to food and water. Tumors were permitted to develop for 21-26 days before imaging.

Animal Preparation. Rats were anesthetized with 2% isoflurane from the time of preparation through the end of each imaging session. Prior to the first imaging session, a ventral branch of the femoral vein was catheterized with PE-10. This catheter was removed after the first imaging session. Prior to the second imaging session, the femoral vein itself was catheterized with PE-50. Immediately following the second imaging session rats were sacrificed by CO_2 asphyxiation. Blood samples were drawn; the brain and lungs were harvested. Brains were placed in Zn-Tris fixative solution after a coronal cut to enhance fixation at the tumor location. Lung samples were flash frozen in liquid nitrogen for biochemical studies.

Determination of Microvessel Density, Proliferative Activity, Apoptosis, and Cell Death. Tumor sections were deparaffinized in xylene and hydrated through graded ethanols to PBS. After blocking endogenous peroxidase activity with 3.0% H_2O_2 the sections were washed 3X in PBS. For CD31 staining the sections were blocked in Protein Block (Biogenex) for 30 min at room temperature, and incubated in murine monoclonal anti-rat CD31 (MA-3107P; Endogen) diluted 1:400, for 2 hr at room temperature.

For Ki67 staining the sections were washed well in dH_20. The sections were then immersed in preheated Target Retrieval Solution (DAKO; #S1699) and microwaved for 8 min at power level 2 (GE Profile JE1360WB). After cooling for 30 min, the sections were washed in dH_20 for 5 min, rinsed 2X in PBS and blocked in Protein Block (Biogenex) for 30 min at room temperature. Sections were incubated in anti-Ki67 polyclonal antibody NCL-Ki67p, 1:800 (Novacastra) for 1 hour at room temperature and washed 3X in PBS/0.3% Tween 20.

For activated caspase 3 staining tumor sections were deparaffinized in xylene and hydrated through graded ethanols to PBS. After blocking endogenous peroxidase in 3.0% H_2O_2 the sections were washed well in dH_20. The sections were then immersed in preheated Target Retrieval Solution (DAKO; #S1699) and microwaved for 10 min at power level 2 (GE Profile JE1360WB). After cooling for 30 min, the sections were washed in dH_20 for 5 min, rinsed 2X in PBS and blocked in Protein Block (Biogenex) for 1 hour at room temperature. Sections were incubated in anti-activated Caspase 3 polyclonal antibody, 1:3000 (Merck Frosst) overnight at 4°C. After incubation with primary antibody all sections were washed 3X in PBS/0.3% Tween 20 and incubated in biotinylated goat anti-mouse IgG (DAKO, K0609). Sections were again washed 3X in PBS/0.3% Tween 20 and incubated with peroxidase-conjugated Streptavidin (DAKO, K0609). Sections were washed 2X in PBS/0.3% Tween 20, 2X in PBS and developed with DAB/NiCl2 (KPL Labs; #54-75-00). The sections were washed in dH_20, dehydrated through graded ethanols, cleared in xylene and coverslipped with Permount (Fisher Scientific).

Tunel staining: An in situ Apoptosis Detection Kit, TACSTM 2 TdT-Blue Label from Trevigen, was used to identify and quantitate cell death following the manufacturers instructions. Briefly, tumor sections were deparaffinized in xylene and hydrated through graded ethanols to PBS. Sections were treated with proteinase K to increase tissue permeability. After blocking endogenous peroxidase activity with 3.0% H2O2 the sections were washed three times in dH20. The sections were incubated in 1X Labeling buffer for 5 min at room temperature, and further incubated in TdT dNTP Mix-Mn2+-TdT Enzyme-Labeling buffer for 45 min at room temperature. The reaction was stopped by addition of 1X stop buffer for 5 min at room temperature. Sections were washed twice in PBS and incubated with 1:750 diluted Strep-HRP solution for 10 min and labeled with substrate Blue label for 5 min at room temperature. The sections were washed in dH20, dehydrated through graded ethanols, cleared in xylene and coverslipped with Permount.

Western Blot Analysis. Lungs were rapidly removed and kept frozen at –70°C until analysis. Lungs were lysed in lysis buffer (20 mM HEPES, pH 7.5, 150 mM NaCl, 1% Triton X-100, 300 mM pervanadate, 50 mM NaF, 1 mM Microcystin-LR with proteinase inhibitor cocktail) and cleared lysates were immuno-precipitated with an anti-KDR antibody [SC-504, Santa Cruz Biotechnology] on Protein A-Sepharose. Samples were run on polyacrylamide gels and transferred onto a PVDF membrane. Blots were probed with anti-phosphotyrosine antibody [#05-321, Upstate Biotechnology] and with anti-KDR antibody [SC-6251, Santa Cruz Biotechnology].

KDR Kinase Inhibitor Preparation. An inhibitor of the intracellular kinase activity of KDR (Sepp-Lorenzino, Mao et al. 2002) (with a method of action schematized in Figure 25) was prepared in a 5mL/kg administration volume corresponding to dose of 100 mg/kg rat. The mesylate salt of the drug was dissolved in 0.5% v/v methylcellulose (in water) at room temperature and sonicated for a few minutes to achieve a uniform solution. There was no need to adjust pH. A single oral dose was delivered via oral gavage 24 hr after baseline MRI imaging. Control animals received oral gavage of methylcellulose only.

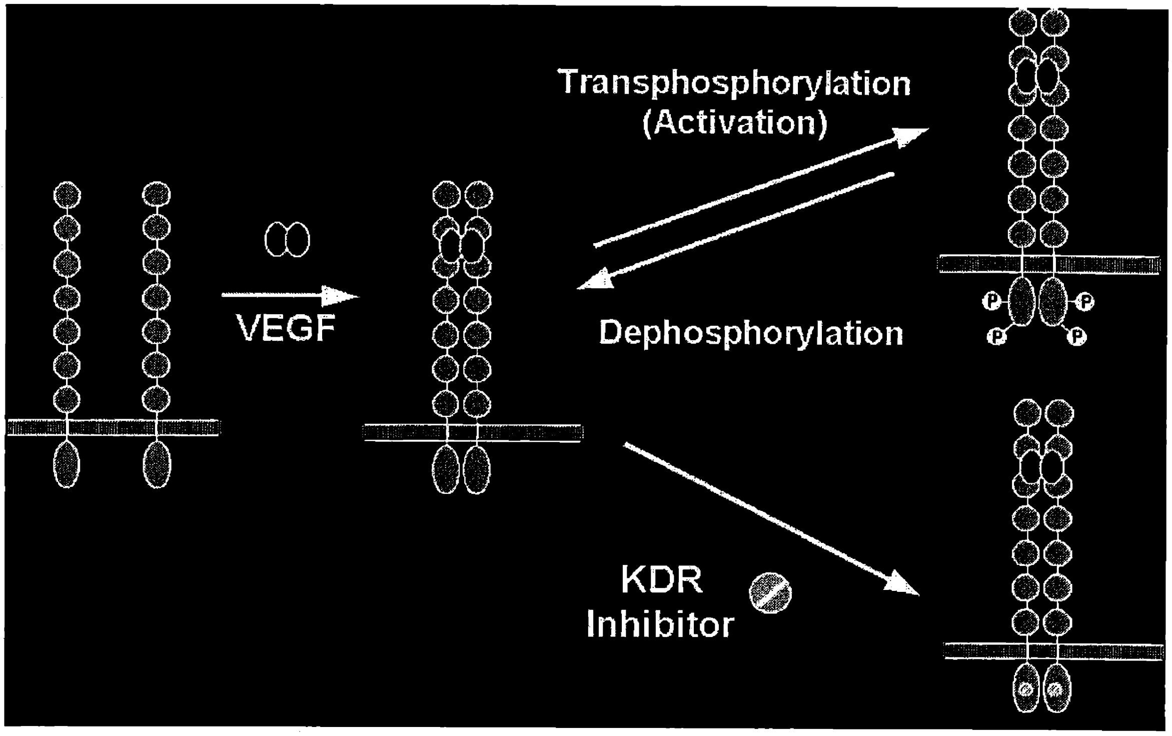

Figure 25 VEGF phosphorylation pathway and the effect of the KDR inhibitor. The compound prevents phosphorylation downstream of VEGF/FLK-1 receptor/ligand coupling. Image courtesy of Merck Research Laboratory, Cancer Division.

MRI. Experiments were performed on a 2T horizontal bore (11 cm diameter) superconducting magnet (Oxford), interfaced with a Varian console. A custom-built surface coil (3.5 cm) was used to transmit and receive RF signal. Rats underwent two imaging sessions: pre- and post-therapy. In each session, following a set of scout images for slice selection, 0.2 mM/kg of gadolinium (Magnevist, Berlex Laboratories, Wayne, NJ) was injected as a bolus over one second. Multi-shot T1-weighted echo planar gradient echo images (TR=500ms / TE=10ms; N_{shot} = 8) were acquired every four seconds across five 1mm thick interleaved contiguous slices through the tumor. The in-plane resolution was 0.78 x 0.78 mm and the flip angle was 90 degrees. Following a baseline period of 2 minutes, the contrast agent was delivered and sampling continued for an additional 10 minutes. The second imaging session occurred at times between 1 and 6 hours after application of therapy (N = 8) or vehicle control (N = 4).

Analysis of MRI data. Our data analysis method is based upon the two compartment physiologic model of Tofts and Kermode (Tofts and Kermode 1991; Tofts, Brix et al. 1999)

$$\frac{dCt(t)}{dt} = k^{trans} Cp(t) - k_{ep} Ct(t)$$

Equation 28

where C_t and C_p are tissue and plasma contrast agent concentration, and k^{trans} and k_{ep} are transport rates into and out from the extracellular extravascular space. We integrated the generalized kinetic model (Equation 28) over time

$$Ct(t) = k^{trans} \int_0^t Cp(t)dt' - k_{ep} \int_0^t Ct(t)dt'$$

Equation 29

Based on the work of van der Sanden and colleagues, we assumed a functional form of the vascular input forcing function Cp(t) and used their experimentally determined constants

$$Cp(t) = \xi\left[A_1 e^{-\lambda_1 t} + A_2 e^{-\lambda_2 t}\right]$$

Equation 30

where A_1 and A_2 are amplitudes (mM) and λ_1 and λ_2 represent bi-exponential plasma decay of gadolinium due to exchange with the extravascular extracellular space and its renal clearance, respectively (Tofts and Kermode 1991). To correct for any variation in injected contrast agent dose, we calculated a fitting factor ξ related to the total constant agent dose in each rat by summing the signal drop due to the first pass T2* effect of gadolinium over eight seconds (2 images) in normal brain contralateral to the tumor. We then fit the full signal time course data (excluding 24 seconds of data after contrast injection because of T2* effects) to the linear equation (Equation 29) for k^{trans} and k_{ep}. Image voxels with less than 10% increase in signal were excluded.

In the permeability-limited regime (PS < F), $k_{ep} = PS\ \rho/v_e$ where PS is the permeability-surface area of the endothelial cells, F is blood flow, ρ is the tissue density, and v_e is the volume of extravascular extracellular space per unit volume of tissue (Tofts, Brix et al. 1999). Based on literature values for normal rat cerebral blood flow (100 ml/min/100g tissue) (Wittlich, Kohno et al. 1995) and v_e (0.27) (van der Sanden, Rozijn et al. 2000), PS in these leaky tumors is still two orders of magnitude less than F. ρ/v_e taken as invariant pre- and post-therapy, the k_{ep} data then provides a quantitative measure of the permeability surface area product.

To directly compare KDR inhibition effects on tumor permeability and total enhancement, an enhancement-based region of interest (ROI) was defined by the pre-therapy post-contrast enhancing pixels on T1-weighted images. This ROI was re-registered to the post-therapy images. We compared calculated values by each method in each animal before and after treatment by a two-tailed, paired t-test. Contralateral striatum permeability was examined to exclude gross BBB breakdown.

Results

Blood samples drawn immediately following the second imaging session and before sacrifice were analyzed to determine the concentration of KDR inhibitor [KDRi] in each rat. Measured [KDRi] ranged from 54nM to 468nM (mean ± SEM = 249nM ± 56nM), all well above the IC_{50} for this compound (IC_{50} = 14nM). From Western Blot analysis (Figure 26), the presence of lung KDR receptor tyrosine kinase (bottom) was verified in all animals. In all treated cases (labeled by T), rat lung basal tyrosine kinase phosphorylation (top) was completely suppressed, while no suppression was seen in methylcellulose vehicle control animals (labeled by C). Figure 26 also shows representative vascular stains by CD31 pre- and post-therapy. No differences in tumor vascularity were found at these early time points. The cell proliferation assay Ki-67 also revealed no tumor differences due to therapy. From the activated caspase-3 and Tunel immunohistochemical staining, no statistically significant increases in apoptosis or total cell death were found.

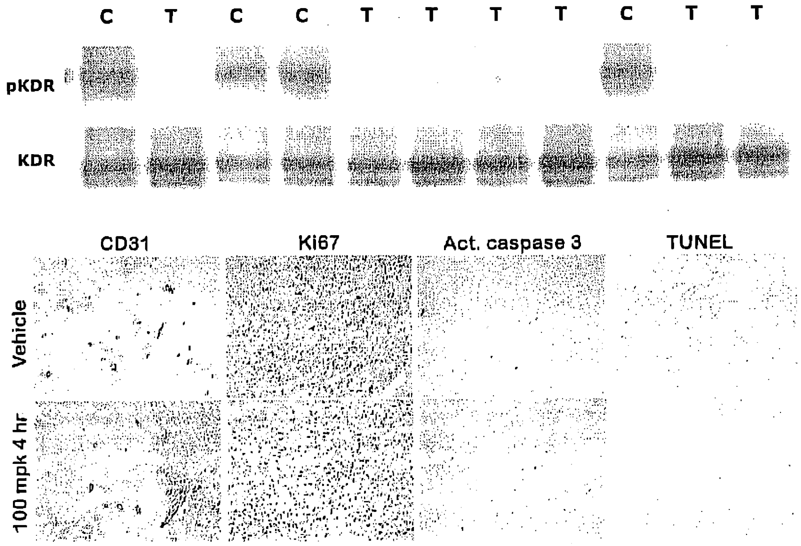

Figure 26 Top) Western Blot analysis showing the presence of lung KDR receptor tyrosine kinase (bottom) and the suppression of lung basal tyrosine kinase phosphorylation (top) in all treated (T) rats but not in control (C) rats. Bottom) No changes in vascularity following treatment were found by CD31 staining. The cell proliferation assay Ki-67 revealed no differences following therapy. Activated caspase-3 and Tunel immunohistochemical staining revealed no statistically significant increase in apoptosis or cell death.

Prior to treatment, regions of signal enhancement were visible following administration of gadolinium (Figure 27a). Applying our physiologic model, we solved Equation 29 for k_{ep} on a voxel-wise basis, creating maps related to permeability surface area product. Pre- and post-therapy images ok k_{ep} are presented in Figure 27a,b respectively.

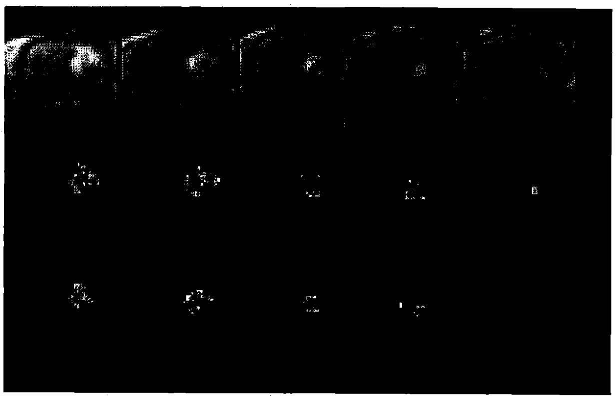

Figure 27 a) Pre-therapy, post-gadolinium T1-weighted MR images. b) Pre-treatment and c) Post-treatment maps of k_{ep}.

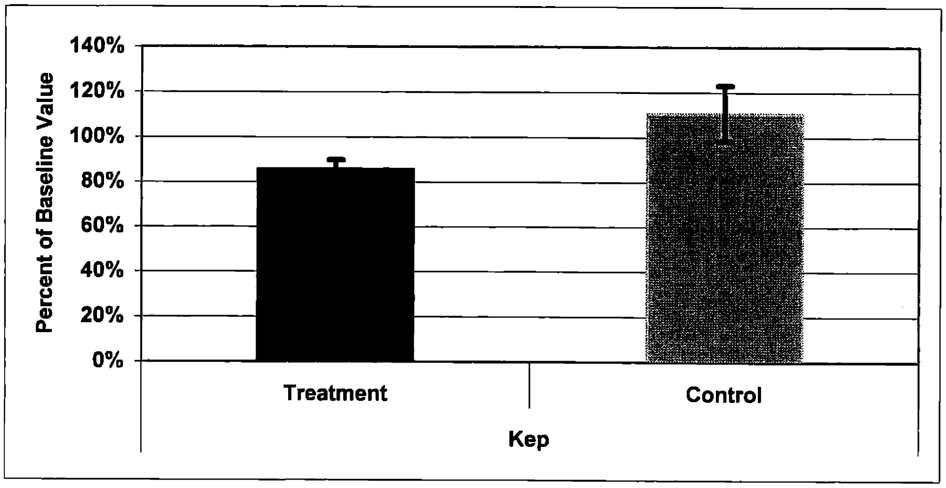

Figure 28 Summary of MRI-measured values post-therapy. * indicates statistically significant change from pre- to post- KDR inhibition ($p < 0.05$, paired t-test).

A summary of findings from the imaging data is presented in Figure 28. We solved the generalized kinetic equation voxel-wise based on a model of Cp(t) and revealed significant changes in k_{ep} ($p = 0.007$). Post-treatment k_{ep} was 86% ± 4% while control animals had k_{ep} 111% ± 12 % of their baseline values. k_{ep} values from each rat are presented in Table 14. At the high dose used in this study, there was no variation in MRI-detected response between early (1 hr) and later (6 hr) imaging times despite measured variation in [KDRi], reflecting super-therapeutic absorption of the oral agent with peak [KDRi] at 1 hr post-gavage and plasma half-life of 2.6 hours.

Treated	Kep, Pre	Kep, Post	%Change Kep
1	0.0051	0.0041	-20%
2	0.0040	0.0036	-10%
3	0.0034	0.0038	12%
4	0.0056	0.0042	-25%
5	0.0074	0.0064	-14%
6	0.0060	0.0049	-18%
7	0.0035	0.0028	-20%
8	0.0089	0.0071	-20%
MEAN	0.0055	0.0046	-14.4%
SEM	0.0019	0.0016	4.1%
Control	Kep, Pre	Kep, Post	%Change Kep
1	0.0047	0.0041	-13%
2	0.0042	0.0055	31%
3	0.0072	0.0066	-8%
4	0.0067	0.0089	33%
MEAN	0.0057	0.0063	11%
SEM	0.0007	0.0010	12%

Table 14 MRI measured values for k_{ep} for all rats.

Discussion

As tumor size response to anti-vascular or anti-angiogenic therapy may lag behind functional changes in their vessels, there has been increasing interest in applying imaging methods to determine vascular physiology changes. Because DCE MRI can be performed in the clinic as well as the laboratory, such techniques are beginning to be used in the context of drug therapy (Evelhoch, Gillies et al. 2000). Many key issues regarding data acquisition, such as spatial and temporal resolution, have been discussed previously (Evelhoch 1999). A few studies have examined changes in fractional plasma volume and unidirectional contrast agent extravasation rate following chronic treatment with monoclonal anti-VEGF antibodies (Pham, Roberts et al. 1998; Gossmann, Helbich et al. 2000; Gossmann, Helbich et al. 2002), while one recent study looked at the acute effects of combretastatin on a carcinoma in the flanks of rats (Maxwell, Wilson et al. 2002).

In this work we evaluated acute permeability-surface area product changes in a brain tumor model following application of an inhibitor of KDR phosphorylation via DCE-MRI. These changes are a biomarker of near immediate neurovascular effect that preceded any measurable histological changes. The compound was successfully delivered with doses that greatly exceeded its IC_{50}, suggesting complete suppression of KDR phosphorylation within one hour. The inhibition of phosphorylation was directly verified by Western Blot analysis. There were no acute changes in tumor vascularity, cell proliferation, or cell death. Based on the lack of a significant increase in activated caspase-3, there was no increase in apoptosis at these early time points. Upregulation of apoptosis, possible in chronic drug studies, is important from an imaging standpoint in that it may increase the extravascular extracellular space available to the injected contrast agent. In such cases, measurements of the cell volume fraction ($1-v_e$) could be used to differentiate changes in compartmental volumes from permeability effects (Donahue, Weisskoff et al. 1995).

Due to blood brain barrier breakdown at the tumor site, unilateral signal enhancement was clearly visible (Figure 2a) with changes in tumor enhancement evident following therapy. Maps of k_{ep} visually demonstrate changes following KDR inhibition (Figures 2b and 2c). The numerical k_{ep} measurement in each tumor revealed decreases in the tumor following therapy with no change found in control animals (Figure 3). Consequently, k_{ep} changes can be used as a pharmacodynamic marker of KDR inhibition, a non-invasive functional index of kinase phosphorylation. Values for k^{trans} were found to be strongly dependent on plasma gadolinium concentration and the injection dynamics, suggesting that k_{ep} is a more reliable surrogate marker of permeability.

In summary, we employed a quantitative dynamic contrast enhanced MRI technique for measuring changes in the permeability surface area product to discern the immediate effect of an experimental KDR inhibitor in 9L/LacZ bearing rats. This KDR inhibitor decreased k_{ep} by 14% modeling the enhancement time course with a two compartment physiological model. DCE-MRI may prove to be a useful rapid pharmacodynamic readout of KDR inhibition, providing critical, complementary, and unique data for go/no-go decisions in pre-clinical development as well as a non-invasive index for future clinical trials.

Donahue, K. M., R. M. Weisskoff, et al. (1995). "Dynamic Gd-DTPA enhanced MRI measurement of tissue cell volume fraction." Magn Reson Med **34**(3): 423-32.

Evelhoch, J. L. (1999). "Key factors in the acquisition of contrast kinetic data for oncology." J Magn Reson Imaging **10**(3): 254-9.

Evelhoch, J. L., R. J. Gillies, et al. (2000). "Applications of magnetic resonance in model systems: cancer therapeutics." Neoplasia **2**(1-2): 152-65.

Folkman, J. (1971). Tumor angiogenesis: therapeutic implications. UNITED STATES IP - 21 VI - 285 JC - NOW EM - 197201 RF - 21 PMID- 0004938153 CU - 1990 EDAT- 1971/11/18 00:00 MHDA- 1971/11/18 00:00 SO - N Engl J Med 1971 Nov 18;285(21):1182-6.

Gille, H., J. Kowalski, et al. (2001). "Analysis of biological effects and signaling properties of Flt-1 (VEGFR-1) and KDR (VEGFR-2). A reassessment using novel receptor-specific vascular endothelial growth factor mutants." J Biol Chem **276**(5): 3222-30.

Gossmann, A., T. H. Helbich, et al. (2002). "Dynamic contrast-enhanced magnetic resonance imaging as a surrogate marker of tumor response to anti-angiogenic therapy in a xenograft model of glioblastoma multiforme." J Magn Reson Imaging **15**(3): 233-40.

Gossmann, A., T. H. Helbich, et al. (2000). "Magnetic resonance imaging in an experimental model of human ovarian cancer demonstrating altered microvascular permeability after inhibition of vascular endothelial growth factor." Am J Obstet Gynecol **183**(4): 956-63.

Maxwell, R. J., J. Wilson, et al. (2002). "Evaluation of the anti-vascular effects of combretastatin in rodent tumours by dynamic contrast enhanced MRI." NMR Biomed **15**(2): 89-98.

Pham, C. D., T. P. Roberts, et al. (1998). "Magnetic resonance imaging detects suppression of tumor vascular permeability after administration of antibody to vascular endothelial growth factor." Cancer Invest **16**(4): 225-30.

Plate, K. H., G. Breier, et al. (1993). "Up-regulation of vascular endothelial growth factor and its cognate receptors in a rat glioma model of tumor angiogenesis." Cancer Res **53**(23): 5822-7.

Sepp-Lorenzino, L., X. Mao, et al. (2002). A KDR inhibitor induces anti-angiogenic effects and prevents tumor growth ina xenograft model. AACR, San Francisco, CA.

Shaheen, R. M., D. W. Davis, et al. (1999). "Antiangiogenic therapy targeting the tyrosine kinase receptor for vascular endothelial growth factor receptor inhibits the growth of colon cancer liver metastasis and induces tumor and endothelial cell apoptosis." Cancer Res **59**(21): 5412-6.

Taylor, J. S., P. S. Tofts, et al. (1999). "MR imaging of tumor microcirculation: promise for the new millennium." J Magn Reson Imaging **10**(6): 903-7.

Tofts, P. S., G. Brix, et al. (1999). "Estimating kinetic parameters from dynamic contrast-enhanced T(1)-weighted MRI of a diffusable tracer: standardized quantities and symbols." J Magn Reson Imaging **10**(3): 223-32.

Tofts, P. S. and A. G. Kermode (1991). "Measurement of the blood-brain barrier permeability and leakage space using dynamic MR imaging. 1. Fundamental concepts." Magn Reson Med **17**(2): 357-67.

van der Sanden, B. P., T. H. Rozijn, et al. (2000). "Noninvasive assessment of the functional neovasculature in 9L-glioma growing in rat brain by dynamic 1H magnetic resonance imaging of gadolinium uptake." J Cereb Blood Flow Metab **20**(5): 861-70.

Wittlich, F., K. Kohno, et al. (1995). "Quantitative measurement of regional blood flow with gadolinium diethylenetriaminepentaacetate bolus track NMR imaging in cerebral infarcts in rats: validation with the iodo[14C]antipyrine technique." Proc Natl Acad Sci U S A **92**(6): 1846-50.

Chapter 7 – Conclusions and Discussion: Putting the Pieces Together

The overarching goal of this work was to refine and utilize MR imaging methods to investigate some of the unusual properties of tumor blood vessels. To accomplish this task, we studied rat brain tumors using experimental intravascular and conventional extravasating MR contrast agents. Our rat models permitted us to collect the MRI data, make correlative histological measurements, and track blood gas, temperature, and blood pressure during imaging to ensure reliable and consistent physiology.

Cerebral Blood Volume

We began by measuring blood volume. Previous work showed how MR signal can be filtered to be especially sensitive to the smallest vessels. Based on these Monte Carlo simulations, we measured not only total blood volume (using gradient echoes) but also microvascularly-weighted blood volume (by spin echoes). Blood volume measurements and their histological correlates vascular area and vascular volume are known to have great clinical relevance in diagnosis and treatment of cancer. Our measurements rely on steady state images before and after the application of the intravascular contrast agent. This measurement is more reliable than first-pass bolus methods and boast greater signal to noise. By tuning the MR sequence to record the microvascularly-weighted blood volume, we also gain insight to the vasculature that is unattainable by any other process beyond tissue sectioning.

We found heterogeneous and highly elevated total blood volume and moderately elevated microvascular blood volume in the tumors. We then performed vessel counting and sizing in sections from the same tumors. These correlations have not been performed previously. We find excellent correlation between histologically determined vascular area and blood volume (microvascular CBV slightly better than total CBV).

Regional analysis of the tumors revealed no significant CBV differences between Tumor Center and Tumor Middle, although the Tumor Edge had lower total and microvascular CBV. This finding could be a result of partial volume averaging with non-tumor tissue, and regional analyses involving tumor edge are confounded by the exact ROI definition of the tumor boundary, an intrinsic problem. Voxel-wise analysis allowed for even closer inspection of CBV in these tumors. Tumor CBV was heterogeneous, ranging from 200% - 600% of normal brain CBV values, while no contralateral striatum voxels were more than twice that region's average.

Mean Vessel Size

A useful consequence of the microvascular sensitivity of SE CBV mapping is the potential to derive an index of vessel size within a voxel. Despite the fact that vessel radii are two orders of magnitude smaller than the spatial resolution of the imaging procedure, previous theoretical work predicted a linear relationship between the ratio of $\Delta R2^*$ and $\Delta R2$ and the size of cylindrical magnetic field perturbers. In this work, we show a good and statistically significant correlation between mean vessel size as measured by this MRI metric and through microscopic vessel sizing of fixed and stained tissues from the same tumors. By comparing the MRI to the established gold standard, we provide evidence of this relationship. Voxel-wise analysis shows similar heterogeneities in tumor and contralateral striatum, but that the mean value of vessel size is greater in tumor.

Perfusion Efficiency

Moving on from static measures of blood volume and vessel size, we investigated the relationship between blood flow and blood volume in tumors. We hypothesized that due to rampant tumor angiogenesis there would be a mismatch between blood flow and blood volume, particularly at the tumor periphery. As a surge in angiogenic factors induces neovascularity, these capillary buds will contribute greatly to the overall blood pool. However, as tumor-spawned vessels are often tortuous, blind-ending, and not necessarily efficiently meshed with the existing vascular matrix, we did not expect to see an equivalent increase in blood flow. We indeed discovered this predicted flow/volume mismatch and studied it both in images and on a voxel-by-voxel basis. Tumors presented with overall low flow per unit volume. We defined a metric of perfusion efficiency by scaling the CBF by the CBV and normalizing this value by that of normal contralateral tissue. Perfusion efficiency was diminished in tumors and greater flow volume mismatch was discovered in the tumor edge than in the tumor center. This finding confirms our earlier hypothesis. Voxel-wise analysis revealed similar distribution of PE in tumor and striatum, but with clearly lower mean PE in tumor. The elevation of CBF and even greater elevation of CBV demonstrate how tumor-based vessels do not grow on the line of normality – balanced flow and volume. This finding suggests that perfusion efficiency MR methods are an ideal approach to measuring the efficiency of tumor vasculature. As Jain *et al.* raise the important issue of anti-angiogenesis treatment streamlining the vasculature, we propose our imaging method as the only means of accurately assessing this quantity non-invasively during experimental drug trials

CBV Response to $PaCO_2$

Our next approach to better understand the tumor vasculature was to study its functionality by evaluating reactivity to physiological perturbation. As changes in CBF and CBV driven by changes in $PaCO_2$ are well-characterized phenomena, we chose to control $PaCO_2$ to measure the change in CBV. Specifically, we increased $PaCO_2$ to measure vasodilation and decreased $PaCO_2$ to determine the ability of vessels to contract. Addition of 5% CO_2 to the breathing gas mixture was the method by which we induced vasodilation; hyperventilation was used to cause vasoconstriction. Others have shown that tumor vessel dilation can be impaired and we verified these results. But while others took this as a marker of non-functioning vasculature, we showed through vasoconstriction that these vessels do indeed function. While vasodilation was diminished, vasoconstriction was robust in this tumor model.

We found when comparing GE and SE CBV reactivity that results for tumor were similar for each imaging method and in both the hypo- and hyper-carbic states. However in the measurement of striatum reactivity, there are differences in the values obtained from the two methods. In the transition to hypercarbia, striatum CBV reactivity via GE was greater than by SE, a difference that reached significance.

Preliminary results from a second tumor line show that diminished tumor vasodilation is not universal among tumors. GLI36 vasodilation was not diminished, a finding that lead us to explore possible reasons for this difference. As tumor CBV was elevated by 250% in the U87 tumor line, but only by 180% in the GLI36, we suggest a mechanical explanation for the differences in vasodilation. If tumor vessels are maximally, or near-maximally, engorged with blood, further expansion may not be possible sure to the size limits imposed by smooth muscle cells.

Overall, these findings refute the previously held notion that vasodilation response is a complete assay of functionality. Bi-directional vasoactivity must be addressed to adequately quantify the functionality of the vasculature, a property that is more complicated than previously understood, and complements the steady-state properties of the tumor vasculature.

Permeability

Future evaluation of drug therapies will be aided by the selection of a suitable surrogate marker. We investigated a KDR kinase inhibitor, a drug that works downstream of vascular endothelial growth factor. As VEGF is also vascular permeability factor, we selected the permeability surface area product (PS) as our surrogate marker. We measured PS before and after therapy in ten rats and in four rats that received the vehicle only. We found a significant decrease in permeability in the treated rats with no change in permeability in the untreated rats, proving that PS MR imaging is a useful technique for evaluating drug efficacy in appropriate animal and treatment models.

The Vascular Imaging Toolkit

Combing all of the previously discussed techniques, we present a vascular imaging toolkit of particular interest in the study of cancer. Given the differences between tumor and normal vascular beds, and given the need for surrogate markers in clinical treatment as well as pre-clinical drug development, the value of these techniques becomes clear. Both the functional and morphometric status of the tumor vascular bed could be useful for the monitoring of anti-angiogenic therapies.

CBV measurements are an obvious means by which to monitor therapy. Having linked these measurements with histology and building upon the work of others in correlating CBV with grade, and prognosis, we show that total and microvascular CBV approaches can be applied as a treatment tracking tool. Currently, CBV mapping is optimal only in animal models where blood pool contrast agents are available, but novel macromolecular contrast agents are likely to be available soon in the clinics. Extensive study will then define the boundaries of utility of these techniques. At the very least, CBV mapping will provide a much more accurate, direct, and appropriate tool for tumor imaging than Gadolinium-DTPA contrast enhancement using BBB breakdown as a proxy for tumor location.

The applications of flow measurement to cancer are many. The perfusion state of a tumor has impact on its progression. CBF measurement by the techniques described within, or by arterial spin labeling, can provide information unattainable through conventional means, i.e., biopsy and histology. It will likely become more common in the realm of patient care. PET, while deemed a gold-standard, has drawbacks with cost, radioactivity, and spatial resolution; frequent longitudinal study in humans is hampered by dose issues.

We have shown our perfusion efficiency metric to accentuate regions of flow/volume mismatch in tumors, of particular note at the periphery of tumors. Future longitudinal studies may reveal these regions to be the "tumor-front" of expansion, presaging the site of infiltration of tumor-spawned vasculature and future malignancy. In the context of drug delivery, the determination of zones of diminished perfusion efficiency will allow investigators to address the issue of streamlined vasculature in response to anti-vascular treatments. This finding is a timely one as scientists and clinicians struggle with the best practice of application of anti-angiogenesis agents, especially with regard to meaningful endpoints. The effectiveness of a compound hinges on its ability to arrive at tumor cells or its specific target. Jain *et al.* are investigating how inefficient vascularity can be streamlined by anti-angiogenesis therapy. Our metric of perfusion efficiency addresses a similar issue, and we predict that the application of anti-angiogenic therapy will raise perfusion efficiency closer to normal in tumors. Future work will address the effect of anti-angiogenic treatment on perfusion efficiency directly.

Combining the methods herein, we have developed a toolkit for vascular exploration. With its contents, we have explored some differences between tumor-based and normal cerebral blood vessels. The result is a clearer understanding of the characteristics of blood vessels induced by tumor angiogenesis. Additionally, these techniques are now available to streamline drug development, study tumor development over time, and track tumor response to treatment.